Ternary hydrogel blends of water-soluble polymers: A fundamental study

by

Mauritz Hermon Otto Pretorius

Dissertation presented in fulfillment of the requirements for the degree Master of Science in Polymer Science at Stellenbosch University

Supervisor: Dr. Marietjie Lutz
Co-supervisor: Dr. Nonjabulo P. Gule

Faculty of Science
Department of Chemistry and Polymer Science

Declaration

By submitting this thesis electronically, I declare that the entirety of the work contained therein is my own, original work, that I am the sole author thereof (save to the extent explicitly otherwise stated), that reproduction and publication thereof by Stellenbosch University will not infringe any third party rights and that I have not previously in its entirety or in part submitted it for obtaining any qualification.

March 2021

Abstract

Poly(vinyl alcohol) (PVA) is a water-soluble polymer. The use of PVA in the preparation of hydrogels has been well reported. However, PVA is not inherently antimicrobial, thus if this polymer is to be used in the medical industry in the form of a hydrogel, binary or ternary hydrogel blends with polymers and fillers offering antimicrobial and wound healing properties could impart these advantageous properties to the end product.

In this study primary and binary hydrogel blends of PVA, chitosan, and a chitosan derivative, namely *N,O*-carboxymethyl chitosan, were produced. Upon successful production and finding the optimum blending ratio, ternary hydrogel blends were produced by the addition of chitin nanowhiskers and cellulose nanowhiskers, individually, to the binary matrices. The distribution of these fillers within the respective matrices was then evaluated by using confocal fluorescence microscopy after labeling the chitin nanowhiskers and cellulose nanowhiskers with a fluorescent marker, fluorescein 5(6)-isothiocyanate.

The effect of blending PVA with chitosan, *N,O*-carboxymethyl chitosan, and the respective fillers was evaluated by using various characterization techniques. Scanning electron microscopy was employed to visualize the effects that blending had on the morphology of the hydrogel blends. Thermogravimetric methods and differential scanning calorimetry were used to investigate the thermal properties and the effects that blending had on these properties. The viscoelastic properties of these hydrogel blends were investigated by exploiting rheological analysis methods. Lastly, the antimicrobial properties of the primary, binary, and ternary hydrogel blends were evaluated by employing a variation of the disk diffusion method.

Opsomming

Poli(vinielalkohol) (PVA) is 'n wateroplosbare polimeer. Die gebruik van PVA tydens die voorbereiding van hidrogelle is wyd bespreek. PVA is egter nie inherent antimikrobies nie, dus as hierdie polimeer in die mediese industrie gebruik gaan word in die vorm van 'n hidrogel, sal binêre of tersiêre hidrogel mengsels met polimere en vullers wat antimikrobiese en wondgenesende eienskappe bied, gemeng word om sodoende hierdie voordelige eienskappe tot die eindproduk by te voeg.

In hierdie studie is primêre en binêre hidrogelmengsels van PVA, kitosaan en ‘n kitosaan afgeleide, naamlik *N,O*-karboksimetiel kitosaan, vervaardig. Na afloop van suksesvolle produksie en nadat die optimale mengverhouding gevind is, is tersiêre hidrogelmengsels geproduseer deur die byvoeging van kitien nanovesels en sellulose nanovesels tot die binêre matrikse. Die verspreiding van hierdie vullers binne die onderskeie matrikse is vervolgens met behulp van konfokale fluoressensie mikroskopie geëvalueer na afloop van etikettering van die kitien- en sellulose nanovesels met 'n fluoreserende merker, fluoresien 5(6)-isothiosianaat.

Die effek van die vermenging van PVA met kitosaan, *N,O*-karboksimetiel kitosaan, en die onderskeie vullers is met behulp van verskillende karakteriseringstegnieke geëvalueer. Skandeer elektron mikroskopie is gebruik om die effek wat vermenging op die morfologie van die hidrogelmengsels het, te visualiseer. Termogravimetriese metodes en differensiële skanderingskalorimetrie is gebruik om die termiese eienskappe en die effek wat vermenging op hierdie eienskappe gehad het, te ondersoek. Die viskoëlastiese eienskappe van hierdie hidrogelmengsels is ondersoek deur gebruik te maak van reologie. Laastens is die antimikrobiese eienskappe van die primêre, binêre en tersiêre hidrogelmengsels geëvalueer deur gebruik te maak van 'n aangepaste skyfdiffusiemetode.

Acknowledgments

I would like to thank the following people for their input and support with regards to the success of the thesis:

My supervisor, **Dr. Marietjie Lutz,** and my co-supervisor **Dr. Nonjabulo Gule** – thank you for the funding and your invaluable input and support provided for the duration of this study.

My **family** and **friends** – thank you for your support throughout my studies – especially **Hildegard**, **Gestél,** and **Annerike** – without our fun outings and frequent study breaks my years at Stellenbosch University would not have been the same.

The **Olefins group** – for creating the best work environment in our office.

I would like to thank the following for their contributions to this study:

Central Analytical Facility (CAF) – specifically **Madelaine Frazenburg** and **Prof. Lydia Joubert** for assistance with electron microscopy, **Lize Engelbrecht** for assistance with Fluorescence microscopy, and **Elsa Malherbe** for assistance with NMR microscopy.

Dr. Leigh Loots for assistance with DSC and TGA.

Mr. Mohamed Jaffer for assistance with TEM.

Prof. Marina Rautenbach for assistance with antimicrobial studies.

Table of contents

Declaration i

Abstract ii

Opsomming iii

Acknowledgments iv

List of figures 4

List of tables 8

List of abbreviations 9

Chapter 1: Introduction 11

1.1 Introduction 11

1.2 Motivation 12

1.3 Problem statement 13

1.4 Aims and objectives 13

1.5 Thesis outline 14

1.6 References 15

Chapter 2: Background 16

2.1 Hydrogels 16

2.2 Nanocomposites 18

2.3 Poly(vinyl alcohol) 19

2.4 Cellulose 19

2.5 Cellulose nanowhiskers 21

2.6 Chitin 22

2.6.1 Chitin extraction 24

2.6.2 Chitin nanowhiskers 24

2.6.3 Chitosan 25

2.7 Fluorescence 29

2.7.1 Fluorescein 29

2.8 References 31

Chapter 3: Experimental 39
3.1 Introduction 39
3.2 Materials 39
3.3 Methods 40
3.3.1 Isolation of chitin nanowhiskers by acid hydrolysis 40
3.3.2 Isolation of cellulose nanowhiskers by acid hydrolysis 40
3.3.3 Fluorescent labeling of chitin nanowhiskers and cellulose nanowhiskers 40
3.3.4 Synthesis of *N*, *O*-carboxymethyl chitosan 41
3.3.5 Production of primary, binary and ternary hydrogels 41
3.3.6 Rheology 42
3.3.7 Swelling studies 42
3.3.8 Antimicrobial studies 43
3.4 Characterization techniques used 43
3.4.1 Transmission electron microscopy (TEM) 43
3.4.2 Fluorescence spectroscopy 44
3.4.3 Confocal fluorescence microscopy (CFM) 44
3.4.4 UV/vis spectroscopy 44
3.4.5 Attenuated total reflectance-Fourier transform infrared (ATR-FTIR) 44
3.4.6 Nuclear magnetic resonance (NMR) 45
3.4.7 Scanning electron microscopy (SEM) 45
3.4.8 Thermogravimetric analysis (TGA) 45
3.4.9 Differential scanning calorimetry (DSC) 45
3.5 References 47
Chapter 4: Preparation and characterization of chitin nanowhiskers and cellulose nanowhiskers 48
4.1 Introduction 48
4.2 Transmission electron microscopy (TEM) 48
4.3 Fluorescence 50
4.3.1 Fluorescence spectroscopy 51
4.3.2 Confocal fluorescence microscopy (CFM) 52

4.4 UV/vis Spectroscopy 54
4.5 Conclusion 56
4.6 References 57
Chapter 5: Preparation and characterization of NOCC form CTS 58
5.1 Introduction 58
5.2 Results and discussion 59
5.2.1 Attenuated total reflectance-Fourier transform infrared (ATR-FTIR) 59
5.2.2 Carbon 13 nuclear magnetic resonance (^{13}C-NMR) 59
5.3 Conclusion 62
5.4 References 63
Chapter 6: Primary, binary, and ternary hydrogel blends by the freeze-thaw method 64
6.1 Introduction 64
6.2 Results and discussion 65
6.2.1 Rheology 65
6.2.2 Swelling studies 70
6.2.3 Antimicrobial studies 72
6.2.4 Confocal fluorescence microscopy (CFM) 74
6.2.5 Scanning Electron Microscopy 79
6.2.6 Thermal analysis 89
6.3 Conclusion 103
6.4 References 106
Chapter 7: Recommendations for future work 110

List of figures

Figure 2.1: Schematic of the formation of a cryogel: (a), macromolecule in solution, (b) solvent, (c) low molecular weight solutes, (d) polycrystals of frozen solvent, (e) unfrozen liquid microphase, (f) polymeric framework, (g) micropores adapted from Zhang *et al.*[3]. 17
Figure 2.2: (a), Monomeric structure of completely hydrolyzed PVA, (b) partially hydrolyzed PVA[25]. 19
Figure 2.3: Chemical structure of the monomeric repeat unit of cellulose. 20
Figure 2.4: TEM micrographs illustrating hydrolyzed (a) tunicin, (b) ramie, (c) cotton, (d) sugar beet, (e) MCC, and (f) bacterial cellulose[37]. 22
Figure 2.5: Visual representation of the possible applications of chitin and chitin derivatives. (Public domain images.) 23
Figure 2.6: Chitin undergoing deacetylation resulting in chitosan. 25
Figure 2.7: Visual representation of the possible application of chitosan and chitosan derivatives. (Public domain images.) 26
Figure 2.8: Schematic representation of antimicrobial mechanisms of chitosan and its derivatives adapted from Hosseinnejad *et al.*[116]. 28
Figure 2.9: The dual-labeling of CNW with FITC (green) and RBITC (red) adapted from Nielsen *et al.*[124]. 30
Figure 4.1: TEM images obtained of the ChNW by means of hydrochloric acid hydrolysis. .49
Figure 4.2: TEM images obtained of the CNW by means of sulphuric acid hydrolysis. 49
Figure 4.3: Histograms displaying the distribution of the width and length measurements of ChNWs and CNWs. 50
Figure 4.4: (a), ChNW; (b), FTIC/ChNW; (c), CNW; (d), FITC/CNW. 51
Figure 4.5: (a), Absorption spectrum of (a), an aqueous suspension of FITC (0,05 wt%); (b), emission spectrum of an aqueous suspension FITC (0,05 wt%); (c), emission spectrum of an aqueous suspension of FITC/ChNW (2 wt%); (d), emission spectrum of an aqueous suspension of FITC/CNW (2 wt%) 52
Figure 4.6: CFM images of a CNW dispersion in deionized water (a) 488 nm, (b) T PMT filter, (c) an overlay of images (a) and (b). 53
Figure 4.7: CFM images of an FITC/CNW dispersion in deionized water (a) 488 nm, (b) T PMT filter, (c) an overlay of images (a) and (b). 53
Figure 4.8: CFM images of a ChNW dispersion in deionized water (a) 488 nm, (b) T PMT filter, (c) an overlay of images (a) and (b). 53
Figure 4.9: CFM images of an FITC/ChNW dispersion in deionized water (a) 488 nm, (b) T PMT filter, (c) an overlay of images (a) and (b). 54

Figure 4.10: The UV/vis spectra of an aqueous suspension of FITC (0,05 wt%), an aqueous suspension of FITC/ChNW (2 wt%), and an aqueous suspension of ChNW (2 wt%) 55
Figure 4.11: The UV/vis spectra of an aqueous suspension of FITC (0,05 wt %), an aqueous suspension of FITC/CNW (2 wt %), and an aqueous suspension of CNW (2 wt %) 55
Figure 5.1: Preparation of NOCC from CTS 58
Figure 5.2: The FTIR spectra of NOCC and CTS. 59
Figure 5.3: The chemical structure of CTS (left) and chitin (right). 60
Figure 5.4: ^{13}C-NMR spectrum of CTS. 60
Figure 5.5: The chemical structure of NOCC (left), CTS (middle), and chitin (right). 61
Figure 5.6: ^{13}C-NMR spectrum of NOCC. 61
Figure 6.1: Determination of the LVE region for the CTSPVA sample with different loadings of ChNW and CNW filler. 66
Figure 6.2: Determination of the LVE region for the NOCCPVA sample with different loadings of ChNW and CNW filler. 66
Figure 6.3: Determination of the LVE region for the PVA sample with different loadings of ChNW and CNW filler. 67
Figure 6.4: The storage and loss modulus of the pure CTSPVA matrix. 68
Figure 6.5: The storage and loss modulus of the pure PVA matrix. 69
Figure 6.6: The storage and loss modulus of the pure NOCCPVA matrix. 69
Figure 6.7: The swelling behavior of the PVA matrix, containing different loadings of CNW and ChNW nanofiller as a function of time. 71
Figure 6.8: The swelling behavior of the CTSPVA matrix, containing different loadings of CNW and ChNW nanofiller as a function of time. 71
Figure 6.9: The swelling behavior of the NOCCPVA matrix, containing different loadings of CNW and ChNW nanofiller as a function of time. 72
Figure 6.10: Preliminary results after a few hours at room temperature, stained with alamarBlue. Left -the PVA matrix, Middle – the CTSPVA matrix, and Right – the NOCCPVA matrix. Fillers and loadings are indicated 73
Figure 6.11: Results after 60 hours of incubation, stained with NBC. Left -the PVA matrix, Middle – the CTSPVA matrix, and Right – the NOCCPVA matrix. Fillers and loadings are indicated 74
Figure 6.12: Left – the fluorescently labeled PVA2%ChNW sample. Right – the fluorescently labeled PVA2%CNW sample. 75
Figure 6.13: Left – the fluorescently labeled CTSPVA2%ChNW sample. Right - the fluorescently labeled CTSPVA2%CNW sample. 75
Figure 6.14: Left - the fluorescently labeled NOCCPVA2%ChNW sample. Right – the fluorescently labeled NOCCPVA2%CNW sample. 76

Figure 6.15: Gallery of fluorescent signals at different depths of the PVA2%ChNW sample. 76
Figure 6.16: Gallery of fluorescent signals at different depths of the PVA2%CNW sample. .77
Figure 6.17: Gallery of fluorescent signals at different depths of the CTSPVA2%ChNW sample. 78
Figure 6.18: Gallery of fluorescent signals at different depths of the CTSPVA2%CNW sample. 78
Figure 6.19: Gallery of fluorescent signals at different depths of the NOCCPVA2%ChNW sample. 79
Figure 6.20: Gallery of fluorescent signals at different depths of the NOCCPVA2%CNW sample. 79
Figure 6.21: Left – The wet CTSPVA1ChNW sample. Right – SEM micrograph of the lyophilized CTSPVA1ChNW sample. 80
Figure 6.22: SEM micrographs of various matrices (labels on image). 82
Figure 6.23: SEM micrographs of various matrices (labels on image). 83
Figure 6.24: SEM micrographs of various matrices (labels on image). 84
Figure 6.25: SEM micrographs of various matrices (labels on image). 85
Figure 6.26: Overview of pore sizes of different matrices and different ChNW filler loadings. 86
Figure 6.27: Overview of pore sizes of different matrices and different CNW filler loadings. 86
Figure 6.28: Pore size distribution of the PVA matrix with different loadings of ChNW and CNW loadings respectively. 87
Figure 6.29: Pore size distribution of the CTSPVA matrix with different loadings of ChNW and CNW loadings respectively. 88
Figure 6.30: Pore size distribution of the NOCCPVA matrix with different loadings of ChNW and CNW loadings respectively. 88
Figure 6.31: A comparison of the decomposition profiles of the ChNW and CNW fillers. 90
Figure 6.32: A comparison of the decomposition profiles of the CTSPVA matrix with different loadings of ChNW. 92
Figure 6.33: A comparison of the decomposition profiles of different matrices with ChNW filler loadings of 2%. 92
Figure 6.34: A comparison of the decomposition profiles of the CTSPVA matrix with different loadings of CNW. 94
Figure 6.35: A comparison of the decomposition profiles of different matrices with CNW filler loadings of 2%. 94
Figure 6.36: DSC thermograms of the second heating cycle and crystallization cycle of primary hydrogels from PVA and binary blends of PVA and ChNW. 97

Figure 6.37: DSC thermograms of the second heating cycle and crystallization cycle of primary hydrogels from PVA and binary blends of PVA and CNW. 98
Figure 6.38: DSC thermograms of the second heating cycle and crystallization cycle of binary hydrogels from CTS and PVA and ternary blends of CTS, PVA, and ChNW. 100
Figure 6.39: DSC thermograms of the second heating cycle and crystallization cycle of binary hydrogels from CTS and PVA and ternary blends of CTS, PVA, and CNW. 101
Figure 6.40: DSC thermograms of the second heating cycle and crystallization cycle of binary hydrogels from NOCC and PVA and ternary blends of NOCC, PVA, and ChNW. 103
Figure 6.41: DSC thermograms of the second heating cycle and crystallization cycle of binary hydrogels from NOCC and PVA and ternary blends of NOCC, PVA, and CNW. 103

List of tables

Table 4.1: Dimensions of the ChNW and CNW nanofillers 50
Table 6.1: Summary of the decomposition steps and onset of degradation of the ChNW and CNW fillers used in this study 89
Table 6.2: Summary of the decomposition steps and onset of degradation of the CTSPVA matrix with ChNW as filler at different loadings compared to the NOCCPVA and PVA matrix with 2% ChNW as filler. Temperatures in bold were identified as the main mass loss step..91
Table 6.3: Summary of the decomposition steps and onset of degradation of the CTSPVA matrix with CNW as filler at different loadings compared to the NOCCPVA and PVA matrix with 2% CNW as filler. Temperatures in bold were identified as the main mass loss step....93
Table 6.4: Peak melting temperature enthalpy with peak crystallization temperature enthalpy of PVA matrix with different loadings of ChNW and CNW nano fillers 97
Table 6.5: Peak melting temperature and enthalpy with peak crystallization temperature enthalpy of CTSPVA matrix with different loadings of ChNW and CNW nanofillers.....99
Table 6.6: Peak melting temperature and melting enthalpy with peak crystallization temperature and crystallization enthalpy of NOCCPVA matrix with different loadings of ChNW and CNW nano fillers 101

List of abbreviations

PVA	Polyvinyl alcohol
CTS	Chitosan
GAG	Glycosaminoglycans
CNW	Cellulose nanowhiskers
ChNW	Chitin nanowhiskers
DCl	Deuterium chloride
D_2O	Deuterium oxide
DMSO-*d6*	Dimethyl sulfoxide-*d6*
MCC	Microcrystalline cellulose
HIV	Human Immunodeficiency Virus
TB	Tuberculosis
NOCC	*N,O*-carboxymethyl chitosan
FITC	Fluorescein 5(6)-isothiocyanate
RBITC	Rhodamine B isothiocyanate
DA	Degree of acetylation
D	Dimensional
TEM	Transmission electron microscopy
EDS	Energy-dispersive X-ray spectroscopy
EELS	Electron energy loss spectroscopy
SEM	Scanning electron microscopy
SE	Secondary electrons

BSE	Backscattered electrons
TGA	Thermogravimetric analysis
DSC	Differential scanning calorimetry
CFM	Confocal fluorescence microscopy
ATR-FTIR	Attenuated total reflectance Fourier transform infrared spectroscopy
IR	Infrared
NMR	Nuclear magnetic resonance
I	Quantum spin number
Z	Mass number
A	Atomic number
G’	Storage modulus
G’’	Loss modulus
tan δ	Loss tangent
σ_0	Stress
γ_0	Strain amplitude
δ	Phase angle between the strain and stress
TMS	Tetramethylsilane
LVE	Linear viscoelastic
LB	Luria Bertani
REDOX	Oxidation – reduction
NBC	Nitrotetrazolium blue chloride

Chapter 1: Introduction

1.1 Introduction

Hydrogels have been used in biomedical applications such as contact lenses and absorbable sutures since the 1960s[1]. The use of poly(vinyl alcohol) (PVA) is well reported, especially as a biodegradable and biocompatible synthetic polymer. PVA is a semi-crystalline, water-soluble polymer that has been widely used in the preparation of hydrogels. It also exhibits excellent solvent resistance, mechanical performance, high hydrophilicity, and biocompatibility[2]. The blending of this polymer with natural polymers such as chitosan (CTS) and CTS derivatives, starch, and alginate and/or their derivatives has increased drastically over the past few decades. CTS is a natural cationic polysaccharide and is prepared via the alkaline hydrolysis of the aminoacetyl groups of chitin, a marine polymer[3]. Chitosan exhibits many desirable properties[1] such as biocompatibility, biodegradability, non-toxicity, sterilizability, and most importantly its versatility in biomedical fields such as immune stimulation, mucoadhesion, it's antimicrobial activity[4] and pharmaceutical applications such as the possibility of drug delivery and tissue engineering[3].

Wound healing is influenced by several factors including bacterial infection. CTS has been shown to exhibit activity against bacteria and fungi[5]. Glycosaminoglycan (GAG) supports cell proliferation which should improve the end product's cellular compatibility[6] and the chemical structure of chitosan is similar to GAG which comprises a large part of the extracellular matrix[5]. According to Zu *et al.*[7], hydrogels are unique carrier matrices for drug delivery systems. This is because the hydrogels are soft, responsive, and capable of water storage. The combination of the advantageous properties of PVA such as its elasticity and high hydrophilicity and CTS or CTS derivatives, with properties such as low toxicity and biocompatibility, makes the resultant materials excellent for the controlled release of drugs.

To produce binary hydrogel blends of PVA and CTS a freeze-thaw method, reported by Abitbol *et al.*[8], where the authors successfully produced composite cryogels containing PVA and CTS, was adopted. The freeze-thaw mechanism is driven by phase separation. As the solution freezes, phase separation occurs which causes the polymer to be rejected from the ice crystallites. The freeze-thaw cycle is repeated, and the size of the ice crystallites grows with increasing cycling resulting in water-filled pores. Consequently, physical crosslinks in the form of hydrogen bonds are formed whilst the gel structure is reinforced by the crystalline polymeric regions. It has also been reported that CTS perturbs the formation of PVA crystallites which results in a material with an irregular structure[9]. An increase in CTS content will thus decrease

crosslinking density leading to an increase in free volume, consequently leading to an increase in the amount of water/drug that can be absorbed by the hydrogel[10].

Reinforcement fillers, such as chitin nanowhiskers, which are acid hydrolysis products of chitin[11], or crosslinking agents may improve the mechanical properties of the hydrogel produced. In a study by Ma *et al*., the tensile strength of a composite chitosan membrane with 3 wt% chitin nanowhiskers content, was increased by about 2.3 times that of the neat chitosan membrane[11].

The similarities in the structures of chitosan and chitin contribute to the formation of strong electrostatic interactions and hydrogen bonds between chitosan and chitin. When stress is applied to the material containing the chitin nanowhiskers, the stress is transferred to the chitin nanowhiskers very quickly. This leads to an increase in tensile strength, this only takes place at exceptionally low nanowhisker content. Some studies have reported a decrease in tensile strength at nanowhisker loadings of more than 3 wt%, which was attributed to the aggregation of the nanowhiskers[11]. It is thus important to investigate whether the materials to be prepared will also follow this trend and this nanofiller loading should be determined for the fillers which will be incorporated in this study.

Cellulose nanowhiskers (CNW) are another attractive possibility of a nanofiller that can be used to produce ternary hydrogel blends due to their affordability, renewability, high crystallinity, aspect ratio, and biocompatibility[8]. CNWs are the sulphuric acid hydrolysis product of microcrystalline cellulose (MCC) and it has been reported that an increase in CNW content in the PVA matrix resulted in a decrease in PVA crystallinity[8]. This should lead to larger pore sizes and an increase in water/drug sorption capacity. CNWs also have the advantage of aqueous stability due to their electrostatic charges imparted by the charged sulfate ester groups introduced during hydrolysis.

1.2 Motivation

Chronic wounds may be present in immunosuppressed individuals; thus, the treatment of these wounds is of great concern. A variety of wound dressings in the form of hydrogels already exists but it is vitally important to further investigate and optimize the physical properties of these wound dressings to make them more cost-effective, structurally stable, biodegradable whilst keeping the biocompatibility of novel wound dressings in mind.

Achieving this will improve the care of chronic wounds whilst simultaneously leading to a reduction in the amount of synthetic waste produced and so reduce the impact on the environment.

1.3 Problem statement

Disease in South Africa is of great concern and current disease prevention measures should be altered and improved to increase the quality of life, as well as life expectancy. One of the contributing factors is the human immunodeficiency virus (HIV) and tuberculosis (TB) infections which weaken the immune system and may lead to chronic wounds. The primary objective of this project is to produce a cost-effective, biodegradable, and biocompatible hydrogel blend. These blends can be supplied to communities in need in South Africa in the form of wound dressings to prevent opportunistic skin infections which will increase the quality of life and prevent death in cases where necrotizing soft tissue infections are apparent. Examples of biocompatible polymers that can be used are polyvinyl alcohol (PVA) and chitosan (CTS), including a derivative thereof, *N,O*-carboxymethyl chitosan (NOCC). CTS is a natural polymer and will contribute to the cost-effectiveness of this hydrogel blend. Chitin nanowhiskers (ChNW) and cellulose nanowhiskers (CNW) are also known for their affordability and renewability[12], thus contributing to lowering environmental impact. These polymers will be used to produce binary blends. Before crosslinking occurs, the binary blends will then be impregnated with different loadings of nanofillers such as ChNW and CNW which will result in a ternary hydrogel blend to increase its thermal stability, and structural integrity to improve its antimicrobial properties.

1.4 Aims and objectives

The overarching aim of this study was to incorporate two different nanofillers, namely chitin nanowhiskers and cellulose nanowhiskers, into different matrices and to evaluate the effect thereof. The effect of the incorporation of these fillers was then to be evaluated with regards to pore size, thermal stability, crystallinity, swellability (water sorption capacity), and viscoelastic properties. Furthermore, the effect of a different matrix will also be evaluated using the same methods. To achieve this aim, the following objectives were considered.

- To isolate the respective fillers (CNW and ChNW) by utilizing sulphuric acid hydrolysis and hydrochloric acid hydrolysis, respectively.
- To fluorescently label the respective fillers with FITC in a one-step procedure in an alkaline environment to visualize the distribution within the matrix by employing confocal fluorescence microscopy.
- To produce primary hydrogels of PVA using the freeze-thaw technique.
- To produce binary hydrogels of PVA and either CTS or *N,O*-carboxymethyl chitosan (NOCC) by blending the respective polymers and subjecting the blend to the freeze-thaw technique.

- The production of ternary hydrogels of PVA, either CTS or NOCC, and either CNW or ChNW by blending the respective polymers and fillers and subjecting the blend to the freeze-thaw technique.
- Evaluating the effect of increasing loadings of the fillers (CNW and ChNW).
- Evaluating the effect of a different matrix whilst keeping the respective filler loading constant.

1.5 Thesis outline

- **Chapter 1**: In this chapter, an introduction of the study as well as the objectives are provided.
- **Chapter 2**: An overview of previous research and fundamental concepts related to this study are discussed in this chapter.
- **Chapter 3**: A description of the experimental procedures used are provided in this chapter. This includes all the materials and research methods used as well as the analytical techniques used to characterize all the materials produced in this study.
- **Chapter 4**: Isolation and characterization of the respective nanofillers used in this study are discussed.
- **Chapter 5**: Derivatization of CTS resulting in NOCC and the characterization thereof is discussed.
- **Chapter 6**: The results emanating from this study are outlined and discussed regarding previous literature followed by conclusions.
- **Chapter 7**: This chapter briefly offers recommendations for future research.

1.6 References

1 E. A. Kamoun, X. Chen, M. S. Mohy Eldin and E. R. S. Kenawy, *Arab. J. Chem.*, 2015, **8**, 1–14.

2 S. Kubo and J. F. Kadla, *Biomacromolecules*, 2003, **4**, 561–567.

3 T. K. Giri, A. Thakur, A. Alexander, Ajazuddin, H. Badwaik and D. K. Tripathi, *Acta Pharm. Sin. B*, 2012, **2**, 439–449.

4 R. A. A. Muzzarelli, *Carbohydr. Polym.*, 2009, **77**, 1–9.

5 M. Ignatova, N. Manolova, N. Markova and I. Rashkov, *Macromol. Biosci.*, 2009, **9**, 102–111.

6 N. Bhattarai, Z. Li, J. Gunn, M. Leung, A. Cooper, D. Edmondson, O. Veiseh, M. H. Chen, Y. Zhang, R. G. Ellenbogen and M. Zhang, *Adv. Mater.*, 2009, **21**, 2792–2797.

7 Y. Zu, Y. Zhang, X. Zhao, C. Shan, S. Zu, K. Wang, Y. Li and Y. Ge, *Int. J. Biol. Macromol.*, 2012, **50**, 82–87.

8 T. Abitbol, T. Johnstone, T. M. Quinn and D. G. Gray, *Soft Matter*, 2011, **7**, 2373.

9 H. Zhang, F. Zhang and J. Wu, *React. Funct. Polym.*, 2013, **73**, 923–928.

10 M. Bayat Tork, N. Hemmati Nejad, S. Ghalehbagh, A. Bashari, A. Shakeri-Zadeh and S. K. Kamrava, *J. Ind. Text.*, 2014, **45**, 1399–1416.

11 B. Ma, A. Qin, X. Li, X. Zhao and C. He, *Mater. Lett.*, 2014, **120**, 82–85.

12 C. Casadidio, D. V. Peregrina, M. R. Gigliobianco, S. Deng, R. Censi and P. Di Martino, *Mar. Drugs*, 2019, **17**, 369.

Chapter 2: Background

2.1 Hydrogels

Hydrogels are characterized as network containing three-dimensional structures which are obtained from synthetic or biopolymers which can absorb and retain large volumes of water in their three-dimensional network[1,2]. Hydrophilic groups present in the polymeric network facilitate interaction and bonding with water molecules which result in the hydrogel structure. There has been an increasing interest in biopolymer hydrogels due to their advantageous properties such as biocompatibility, and biodegradability[3,4]. Hydrogels have potential applications in drug delivery[3,5], wound dressings[6,7], tissue engineering[8], sensors[9], and purification[10].

Hydrogels can be classified according to their polymeric composition namely: homopolymeric, copolymeric, and multipolymer interpenetrating polymeric hydrogels. Homopolymeric hydrogels are polymer networks derived from homopolymers, polymers that resulted from the polymerization of a single type of monomer[2]. Copolymeric hydrogels are derived from copolymers, polymers that resulted from two or more different monomers and that contains at least one hydrophilic component[11]. Copolymers include block copolymers, alternating copolymers, or random copolymers. Multipolymer interpenetrating polymeric hydrogels are comprised of two or more independent, crosslinked natural or synthetic polymer components in a three-dimensional network form[12]. Semi interpenetrating polymeric hydrogels contain one crosslinked and one uncrosslinked polymer[12].

Hydrogels can be divided into two categories based on the type of crosslinking, thus the chemical or physical nature of the formation of the crosslinks[13]. Crosslinked networks induced chemically form irreversible covalent bonds whilst networks that were induced physically have reversible links. Reversible links are due to either polymer entanglements or physical interactions. Physical interactions include hydrogen bonding, ionic interactions, and hydrophobic interactions[2].

As mentioned, a versatile method to produce hydrogels involves chemical crosslinking. Crosslinkers are difunctional molecules that allow the formation of bonds between polymer chains[13]. Chemical crosslinkers include di-aldehydes, such as glutaraldehyde, formaldehyde, or ethylene glycol di-glycidyl ether[13]. Reactions of chitosan with aldehydes are well documented[13] where the amine group of chitosan forms covalent imine bonds with the aldehyde[14]. Hydrogels crosslinked by chemical methods usually exhibit exceptional

mechanical properties[15]. A major drawback of chemical crosslinking is that the crosslinking agents are frequently toxic and impair biocompatibility. Consequently, any unreacted crosslinking agent has to be extracted from the hydrogel before its end-use to prevent undesirable reactions with bioactive substances in the matrix[3].

Unfavorable effects are completely avoided if crosslinking occurs by physical methods where gel formation arises without the use of toxic crosslinking agents and organic solvents. The freeze-thaw technique is one of the techniques exhibiting such potential[3]. Macroporous heterophase cryogels result from cryogelation as an effect of being frozen and subsequently undergoing thawing of the initial system in which conditions for gelation are already present or specifically created[16,17]. A prerequisite for the formation of a heterogeneous gel is the crystallization of the majority of the solvent[3]. The subsequent thawing of the cryogel then causes cryostructurates to form[18]. The conversion of water to ice causes an increase in polymer concentration which in turn leads to the alignment of polymer chains and this may provide an explanation for the formation of side-by-side associations of the polymer chains. These associations then remain intact upon subsequent thawing and serve as the crosslinking zones within the hydrogel[3]. Cryogel formation is illustrated in **Figure 2.1**.

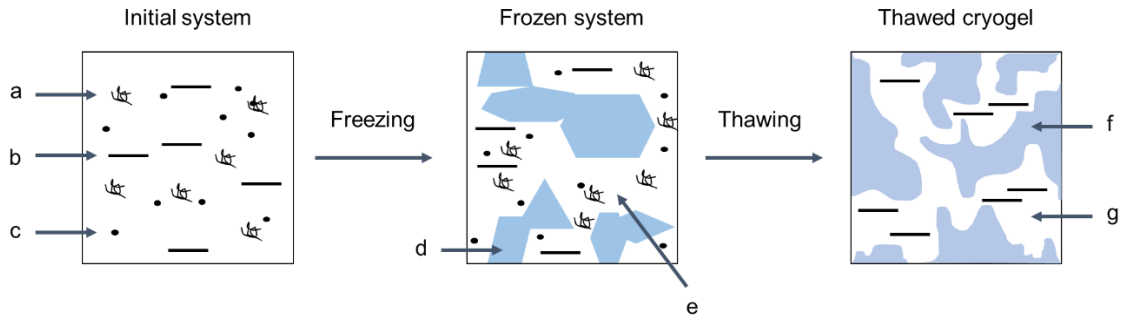

Figure 2.1: Schematic of the formation of a cryogel: (a) macromolecule in solution, (b) solvent, (c) low molecular weight solutes, (d) polycrystals of frozen solvent, (e) unfrozen liquid microphase, (f) polymeric framework, (g) micropores adapted from Zhang *et al.*[3].

Hydrogel composites containing natural polymers hold various applications with the focus on tissue engineering[19]. Chitosan is a polysaccharide with amine functionality and because of its enzymatic biodegradability[20], favorable swelling, solvent retaining, and film-forming ability[10], it is receiving increased interest for possible biomedical and pharmaceutical applications[21]. Carboxymethyl chitosan, an important derivative of chitosan is also useful in the production of hydrogels because its water solubility is much higher than that of chitosan, exhibits very low toxicity, biocompatibility, and biodegradability[22]. Chitosan has poor solubility in neutral aqueous solutions and many organic solvents and even though chitosan can be dissolved in

acidic solutions, these require neutralization before being used in biological applications[23]. Much like chitosan and some of its derivatives, poly(vinyl alcohol) (PVA) is nontoxic and biocompatible. It has a range of desirable properties amongst the ability to form films and its elastic nature[21]. The combination of the advantageous properties of these two polymers and their derivatives are thus a promising perspective.

2.2 Nanocomposites

A nanocomposite can be defined as a multicomponent material with at least one physical dimension having the order of magnitude in nanometres[24]. A polymer composite encompasses characteristics that are not observed in the original polymer matrix or the reinforcement filler used. A variety of fillers may be used in any polymer matrix such as volcanic minerals, glass fibers, carbon fibers, and metal powders and their incorporation may alter the physiochemical properties of the polymer[25]. ChNWs have been incorporated as nanofillers in biomedical materials such as scaffolds, hydrogels, and wound dressings, where the material has to be cytocompatible[19].

Nanomaterials can be classified as either 0, 1, 2, or 3 dimensional (D). Quantum dots, nano lenses, and nano onions make up 0D materials. 1D materials exist in the form of nanowires, nanobelts, or nanotubes[25]. 2D materials are in the form of nanosheets, nanoplates, nanodisks, or nanowalls[25] and 3D materials comprises nano coils, nanocones, nanoballs, nanoflowers, or nanopillers[26,27].

Nanofillers are usually added in quantities of less than 5 wt% and are known to enhance properties such as strength, modulus, heat and scratch resistance, dimensional stability, and thermal properties[25]. There exists a high degree of interaction between the surrounding polymer matrix and the nanofiller because nanofillers feature an increased surface area for interaction with surrounding chemical groups[25].

Because PVA has excellent water solubility and biocompatibility it is useful in the production of biomedical devices[25]. Chitin nanowhisker fillers are getting a lot of attention lately due to their promising reinforcement properties because of their high stiffness and strength[28]. Studies are reported where the authors accomplished the incorporation of chitin nanowhiskers into PVA to produce nanocomposites[5,29]. PVA nanocomposites containing chitin nanowhiskers exhibited increased thermal stability, tensile strength, and water resistance as per a study conducted by Sriupayo *et al.*[30] and Peng *et al.*[5]. Another study investigated chitosan films for multiple applications such as tissue engineering, wound dressings, drug carriers, and films for food packaging[19,31]. One of the problems encountered when using chitosan films for food

packaging is its solubility in water and other aqueous solutions[19]. The combination of α-chitin nanowhiskers with heat treatment has been shown to decrease the affinity of the chitosan/α-chitin nanowhisker composites for water, imparting stability to the composites in an aqueous environment[30].

2.3 Poly(vinyl alcohol)

PVA was first produced in 1924 via the saponification of poly(vinyl acetate) with a sodium hydroxide solution[32]. It is a semi-crystalline, synthetic polymer[33] and exhibits hydrophilic[34], biocompatible, thermostable, and excellent optical properties. The number of hydroxyl groups present in the polymer is determined by the degree of hydrolysis which influences its mechanical and physiochemical properties[35]. Mechanical properties can be further tailored by the addition of nanofillers[25].

Saponification of poly(vinyl acetate) by the controlled partial alkaline hydrolysis of the ester groups into hydroxyl groups results in a precipitate called PVA[25]. The degree of hydrolysis is controlled by controlling the length of the saponification reaction[36]. Different grades of PVA based on molecular mass and degree of hydrolysis exhibiting different physical properties like melting point, viscosity, pH, refractive index and band gap are available commercially[36]. The structure of partially hydrolyzed PVA and its monomeric unit is shown in **Figure 2.2**.

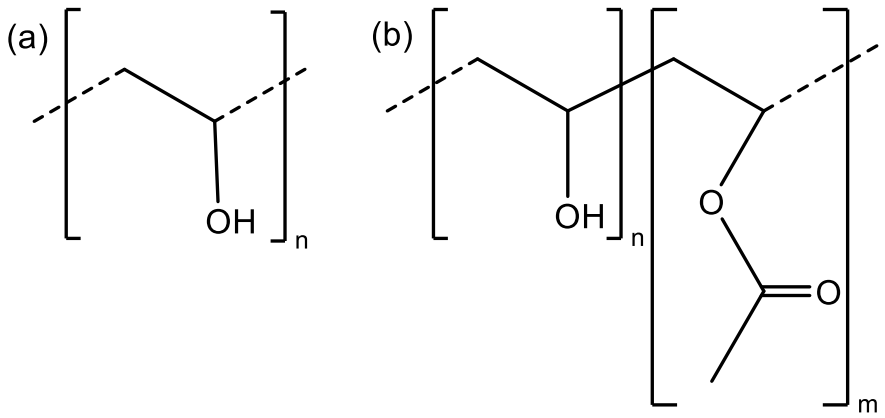

Figure 2.2: (a) Repeat unit of completely hydrolyzed PVA, (b) partially hydrolyzed PVA[25].

2.4 Cellulose

Cellulose is the most abundant renewable biopolymer in nature that can be extracted from plant fibers[37]. Plant fibers are a complex composite in which rigid cellulose microfibrils are rooted within a softer matrix composed of hemicellulose and lignin[38,39]. All cellulosic fibers do not have equal physical properties, and these are influenced by factors such as chemical

composition, the structure of the fiber, microfibril angle, cell dimensions, and of course defects that occur naturally – this variation exists between parts of the same plant and between different plants and origin[40]. Mechanical properties are determined by the crystalline organization within different types of cellulose[41]. Cellulose can also be biosynthesized by various organisms such as lower to higher plants, amoebae, sea creatures as well as fungi and bacteria[42]. It is composed of a linear homopolysaccharide which consists of β-D-glucopyranose units connected via β-1-4-linkages[43] (**Figure 2.3**).

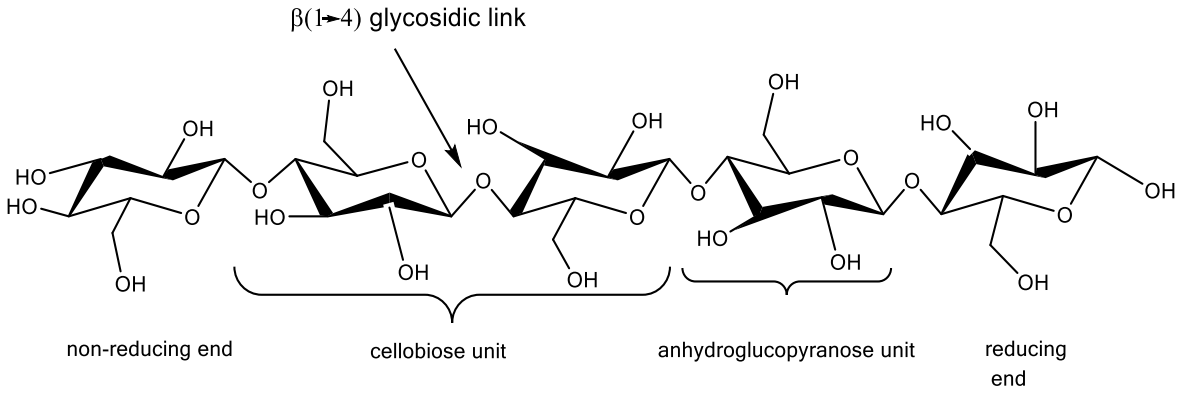

Figure 2.3: Chemical structure of the monomeric repeat unit of cellulose.

Each repeat unit contains three hydroxyl groups that can form hydrogen bonds and will influence the crystalline packing and therefore also influence the physical properties of cellulose[44].

It has been shown by infra-red and x-ray spectroscopy analysis of the organization of cellulose found in plants that the bulk of cellulose is made up of crystallites with interspersed amorphous regions. Two main polymorphs of cellulose exist and can be referred to as either native cellulose – cellulose I or regenerated cellulose – cellulose II. Regenerated cellulose refers to cellulose precipitated out of solution, usually alkaline[37]. The present information on the crystallography of cellulose indicates that the configuration of cellulose I is in parallel chains[45,46] whilst cellulose II has an antiparallel structure[46,47]. Cellulose II is thermodynamically more stable than cellulose I due to the fact cellulose II exhibits intersheet hydrogen bonding[47,48]. Other polymorphs include cellulose III_I, III_{II}, IV_I, and IV_{II} and can be converted to one another with various chemical treatments of the source[49].

After investigations by Atalla and Van der Hart[50] in the 1980s, it became clear that cellulose I have two crystalline forms namely I_α and I_β. Cellulose from different origins consists of different ratios of allomorphs, I_α, and I_β, and this influences some of the physical properties of the

cellulose fibers[47]. Later it was also shown that cellulose I_α and cellulose I_β can be found in the same sample[51] and along the same microfibril[52].

2.5 Cellulose nanowhiskers

There are many different terms in literature to describe these rod-like nanoparticles but they are most often referred to as cellulose nanowhiskers or cellulose nanocrystals[37]. Cellulose fibers and microfibrils display an irregular surface. Apart from the crystalline domains, cellulose also consists of an amorphous state. The random orientation of the amorphous regions results in a lower density, compared to the density of the crystalline regions[47,53]. Amorphous regions are weaker and more susceptible to acid hydrolysis. Under controlled conditions, amorphous regions may be removed whilst the crystalline regions remain unaffected. Amorphous regions are penetrated by hydronium ions and promote hydrolytic cleavage of the glycosidic bond which causes the individual crystallites to be released[53].

Dong *et al.*[54] reported pioneering findings after studying the effects of hydrolysis conditions on the physical properties of the cellulose nanowhiskers. Amongst others, it was proved that increased hydrolysis time results in shorter nanowhiskers and increased surface charge. Moreover, the effects of using hydrochloric acid versus sulfuric acid were studied by Dufresne[55] and it was reported that sulfuric acid provided more stable aqueous systems when compared to hydrochloric acid. Nanowhiskers prepared via sulfuric acid hydrolysis are surface-functionalized with sulfate ester groups which imparts a negative charge to the surface resulting in a decreased tendency for agglomeration in aqueous medium[56,57].

Cellulose nanowhiskers may be isolated from a few different cellulose sources, including but not limited to microcrystalline cellulose[58], bacterial cellulose[59], tunicin[60,61], cotton[62], ramie[63], and sugar beet[64]. Transmission electron micrographs showing the morphology of cellulose nanowhiskers isolated from different sources are illustrated in **Figure 2.4**

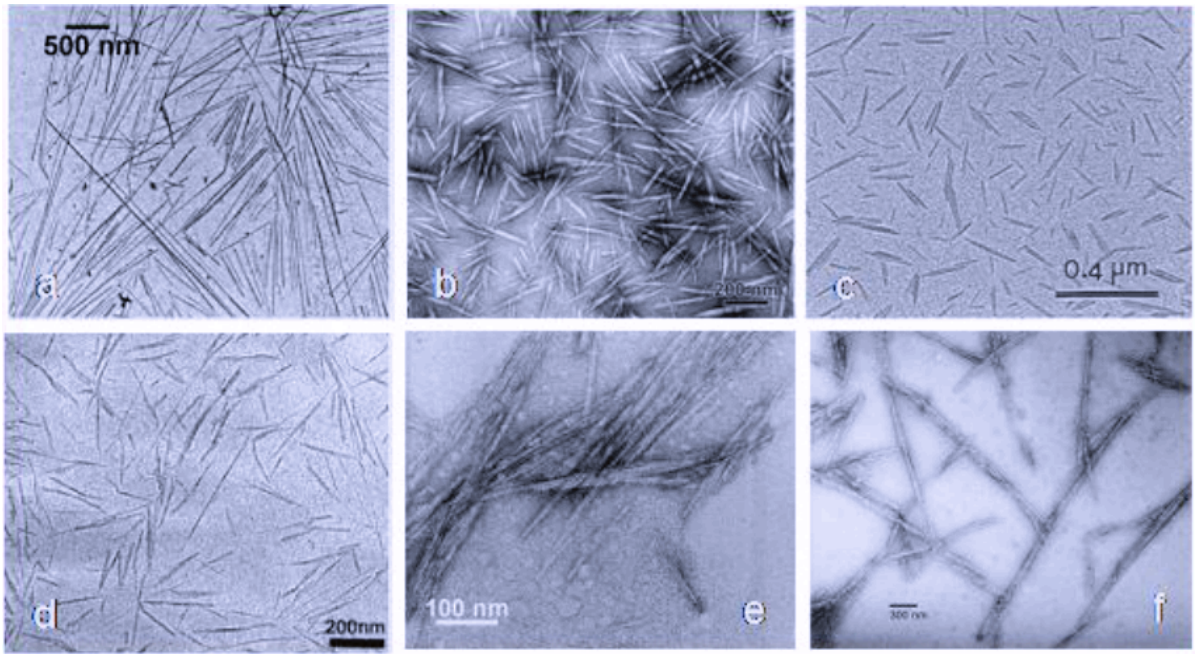

Figure 2.4: TEM micrographs illustrating hydrolyzed (a) tunicin, (b) ramie, (c) cotton, (d) sugar beet, (e) MCC, and (f) bacterial cellulose[37].

2.6 Chitin

Chitin, the second most abundant natural polymer after cellulose, is known to be renewable and biodegradable[65]. It is found in large amounts in the exoskeleton shells of arthropods which include shrimps, crabs, and beetles. It is also found in the internal vertebral column of cephalopods, worms, webs of spiders, and fungal cell walls[66–68]. Even though chitin has such a high abundance in nature and is so easily accessible, it is still an underutilized resource due to its insolubility in water and most organic solvents[19].

Chitin is also non-toxic, odorless, biocompatible with human tissue, and biodegradable[66], its exhibiting antibacterial, moisture-retaining, and wound healing properties[69]. Both chitin and chitosan can be applied in the fields of water purification[70], cosmetic additives[71,72], antibacterial agents[73,74], heavy metal chelating agents, and biomedical applications like wound dressings, antibacterial coatings, and stent coatings[75,76] (**Figure 2.5**).

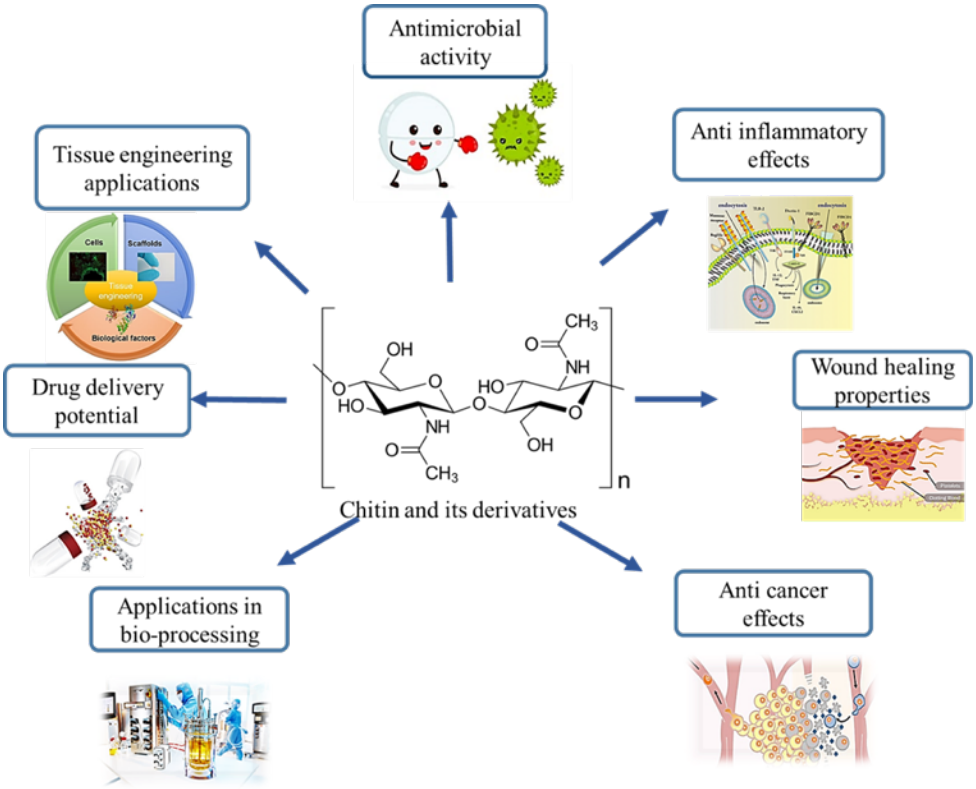

Figure 2.5: Visual representation of the possible applications of chitin and chitin derivatives. (Public domain images.)

Chitin is a linear, polysaccharide of high molecular weight that consists of copolymer repeat units of β-(1→4)-2-acetamido-2-deoxy-β-D-glucose and β-(1→4)-2- amino-2-deoxy-β-D-glucose[77]. Strong hydrogen bonding results due to the inclusion of two hydroxyl groups and an acetamide group in the β-(1→4)-N-acetyl glycosaminoglycan structure. Crystalline fibrils make up native chitin fibers in living organisms – these are referred to as microfibrils and thin filaments, strongly bonded by hydrogen bonds. These fibrils are usually embedded in a protein matrix and depending on their origin, have diameters of 2.5 – 2.8 nm[78].

Samuels[79] showed using X-ray diffraction that native chitin may occur in one of three polymorphic forms namely α-chitin, β-chitin, and γ-chitin, depending on its origin. In α-chitin strong intermolecular hydrogen bonding between molecules is observed and molecules are arranged in an anti-parallel fashion and crystallinity of higher than 80% is observed[80]. α-chitin is also the most abundant form and is obtained from crabs, lobster, krill, and shrimp shells, fungal and yeast cell walls, and insect cuticle[67]. β-chitin is obtained from squid pens and tube worms[81,82] and the molecules are arranged in a parallel fashion. Lastly, in γ-chitin the molecules are arranged in both parallel and anti-parallel fashion[19].

2.6.1 Chitin extraction

As mentioned, the cuticles of various crustaceans are the main source of the primal matter required for the manufacture of chitin. In shellfish, chitin forms part of a multifaceted protein network onto which calcium carbonate is deposited that results in the shell, thus chitin and protein have a specifically intimate interaction and some protein is involved in the polysaccharide-protein complex. The isolation of chitin requires the removal of proteins and inorganic calcium carbonate. Minute quantities of lipids and pigments are also removed by the following two steps: protein is removed by deproteinization whilst inorganic calcium carbonate is removed by demineralization[83]. Deproteinization and demineralization can both occur via chemical or enzymatic treatments applied in any order. Microbial fermentation can also be applied which causes deproteinization and demineralization to occur simultaneously[83].

Chemical deproteinization occurs with the use of NaOH as the preferential agent which is used at concentrations of up to 5.0 M and a temperature of up to 160 °C or enzymatically. The use of NaOH leads to hydrolysis which lowers its molecular weight as well as partial deacetylation of chitin. Enzymatic deproteinization requires the use of proteases which can be derived from animal, microbial or plant sources. These proteolytic enzymes include alcalase, pepsin, papain, pancreatine, devolvase, and trypsin. By using these enzymes, proteins can. Be removed during chitin isolation whilst deacetylation and depolymerization are minimized. It can be performed either before or after demineralization. Enzymatic deproteinization methods are inferior to chemical methods. After enzymatic deproteinization, about 5 – 10% residual protein remains which can be removed by additional NaOH treatment under milder conditions to ensure the purity of the isolated chitin.

Chemical demineralization is performed by acidic treatment. The preferred acid for this treatment is hydrochloric acid. The decomposition of calcium carbonate easily occurs with the use of hydrochloric acid where calcium carbonate is converted to water-soluble calcium salts such as calcium chloride. These salts can then be removed via filtration followed by washing with deionized water.

2.6.2 Chitin nanowhiskers

Various methods may be employed to prepare chitin nanowhiskers which include acid hydrolysis[35,69,81,82], TEMPO-mediated oxidation[80], ultrasonication[84], electrospinning[85], and mechanical treatment[86]. Chitin microfibrils are made up of alternating amorphous and crystalline domains and when these are submitted to strong acid hydrolysis treatment, longitudinal cutting of microfibrils results, leading to the dissolution of the amorphous

domains[87]. The residue of high crystallinity can then be transformed into a stable colloidal suspension by strong mechanical shearing action[88].

Modification through chemical reactions is possible as a result of the fact that the surface of the chitin nanowhiskers is covered with hydroxyl groups. This will impart specific functions and increase the field of application of chitin nanowhiskers. Surface chemical modification also lowers the surface energy of chitin nanowhiskers helping to increase their ability to disperse in low polarity solvets[19].

2.6.3 Chitosan

The term chitosan can refer to a collection of polymers obtained from the deacetylation of chitin as illustrated in **Figure 2.6**. Deacetylation can occur to various degrees and is referred to as the degree of acetylation (DA). When DA is less than 50 mol% the product is referred to as chitosan which will be soluble in acidic aqueous media. To some degree depolymerization also occurs during deacetylation which is clear when looking at the changes in molecular weight[83]. Chemical or enzymatic processes can be used to convert chitin to chitosan[89–91]. A visual representation of the applications of chitosan and chitosan derivatives can be seen in **Figure 2.7.**

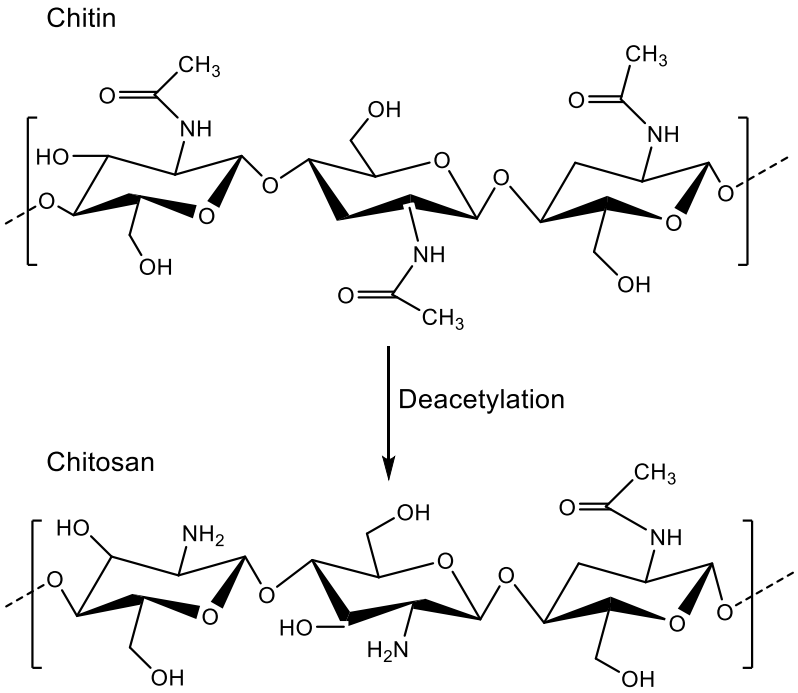

Figure 2.6: Chitin undergoing deacetylation resulting in chitosan.

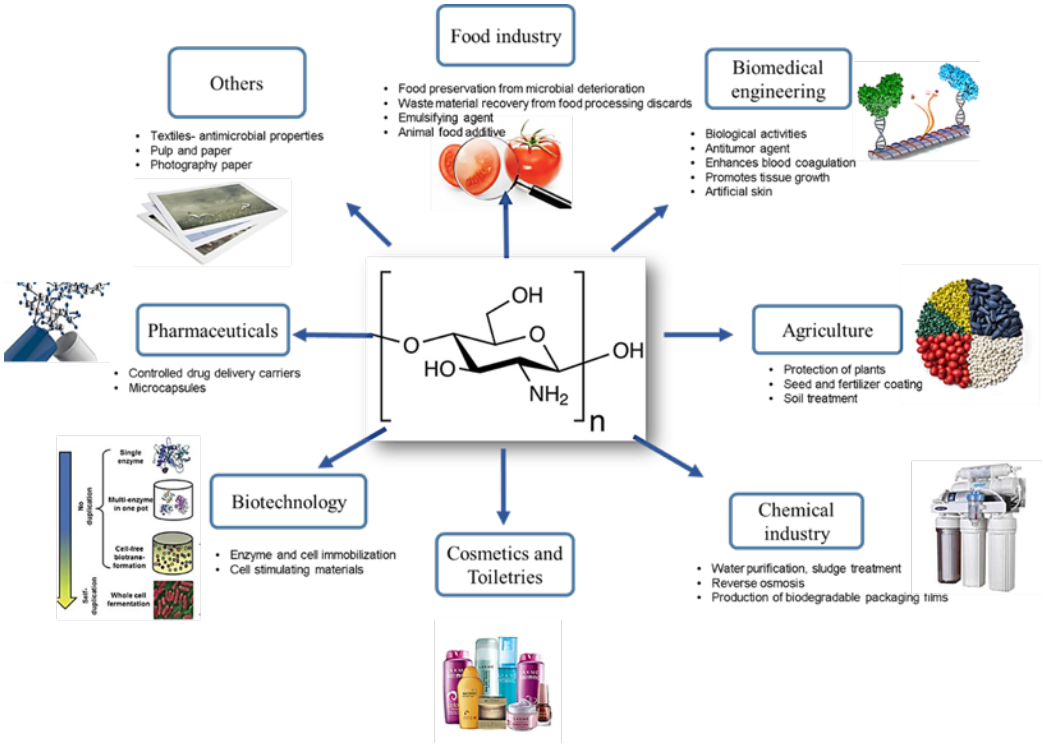

Figure 2.7: Visual representation of the possible application of chitosan and chitosan derivatives. (Public domain images.)

2.6.3.1 Chemical deacetylation

With chemical deacetylation, either acidic or alkaline methods can be used but due to the susceptibility of glycosidic bonds to acidic cleavage, alkaline methods are preferred and used most often[92,93]. *N*-deacetylation of chitin can be achieved homogeneously[94] or heterogeneously[95]. In the homogeneous procedure, chitin is dissolved in an alkaline solution (8% NaOH) through repeated freezing and thawing, and a chitin suspension results. It is the swelling and dissolving of chitin that causes the polymer to become more amorphous. In the case of homogeneous deacetylation, deacetylation is cryoactivated[94]. Basic chitin is prepared via the suspension of chitin in concentrated sodium hydroxide (30 g NaOH/45 g H_2O/3 g Chitin) at 25 °C for about 3 hours, which after dissolution occurs in crushed ice. Soluble chitosan with a DA of 48-55% results[96]. This method produces deacetylation with a uniform distribution of acetyl groups along the polymer chain. During the heterogeneous procedure, chitin is subjected to treatment with concentrated sodium hydroxide at elevated temperature for some hours. Deacetylation will occur rapidly in amorphous regions and to a lower degree in crystalline regions[94]. The insoluble residue that results is chitosan with a DA of 85-99%[83]. It was, however, shown by Aiba[97] that the heterogeneous method results in a non-uniform distribution of the *N*-acetyl-D-glucosamine and D-glucosamine residues, including acetyl groups in block-wise distribution.

2.6.3.2 Enzymatic deacetylation

Chemical deacetylation of chitin does not come without drawbacks. Some of these include high energy consumption, waste of concentrated alkaline solution, and a broad range of soluble and insoluble products[83]. An alternative enzymatic method that exploits chitin deacetylases have been employed to overcome some of these drawbacks. Chitin deacetylases offer a controlled process and result in well-defined chitosan[98]. This enzymatic activity has been reported in several fungi[99–101] as well as insect species[83].

2.6.3.3 Antimicrobial activity

Due to the emergence of antibiotic resistance and formerly unknown pathogenic bacterial strains, bacterial infection remains a significant cause of disease and mortality. This has led to a growing interest in antimicrobial polymers such as chitosan[102] as alternatives to antibiotic treatments for superficial infections. Chemical derivatization is one way of increasing activity and manipulating solubility[103]. Some of the functional groups that have been used to derivatize chitosan are quaternary ammoniumyl, guanidinyl, carboxyalkyl, hydroxyalkyl, thiol-containing groups, and hydrophobic groups (alkyl chains and substituted phenyl and benzyl rings)[102,104–110].

2.6.3.3.1 Mechanism of antibacterial effect

A difference in antimicrobial activity towards gram-negative and gram-positive bacteria is exhibited can be attributed to the variation in the bacterial cell wall. gram-positive bacteria have a thick peptidoglycan layer serving as the cell wall. The cell wall consists of teichoic acids bearing negative charges which are covalently bonded to *N*-acetylmuramic acid whilst lipopolyteichoic acids are covalently bonded to the cytoplasmic membrane. Teichoic acids provide the cell wall with increased strength whilst high-density charges are uniformly ordered within the cell wall and thus influencing the movement of ions through the membrane[103]. In gram-negative bacteria, the peptoglycan layer is covered by an extra layer referred to as the outer membrane. The outer membrane is primarily made up of lipoprotein and lipopolysaccharide. Lipopolysaccharide contains *O*-specific side chains that are hydrophilic and helps to identify bacteria[103]. This outer membrane must first be overcome before hydrophobic molecules and macromolecules can interact with gram-negative bacteria. In an attempt to explain the mechanism of interaction of chitosan with either the cell wall or with the outer membrane, four different models were proposed[103].

The first model and most generally recognized model is based on the electrostatic attraction of the positively charged groups present in chitosan to the negatively charged bacterial

constituents. Antimicrobial effects are however only observed at pH lower than 6 because quaternary ammonium groups ($R\text{-}NH_3^+$) compete with divalent metal ions such as Ca^{2+} and Mg^{2+} which are present in the bacterial cell wall for binding with polyanions[111]. This could limit some applications in neutral and physiological applications. It is commonly assumed that the positive charge in the chitosan backbone in its protonated state at a pH below 6 is a prerequisite for activity against negatively charged bacteria according to the first model[111]. It has also been postulated that this electrostatic interaction is different in gram-negative and gram-positive bacterial species. In gram-positive bacteria, it is proposed that the peptidoglycans get hydrolyzed and this results in leaking of the intracellular components as illustrated in **Figure 2.8**.

A second mechanism states that chitosan can alter the permeability of the outer envelope as a result of bonding to it ionically, in gram-negative bacteria, and thus preventing the passage of nutrients into the cell whilst simultaneously causing a build-up of osmotic pressure inside of the cell. This causes the cell to ultimately die due to a lack of nutrients[112].

The third mechanism states that bacteria are targeted, intracellularly. In this theory chitosan perforates the cell and interacts with its DNA, thus preventing transcription and interrupting protein and mRNA synthesis[113,114]. The penetration ability of chitosan is however one of the key factors that govern the validity of this model so it is unlikely that this model will hold for chitosan and chitosan derivatives of high molecular weight[115].

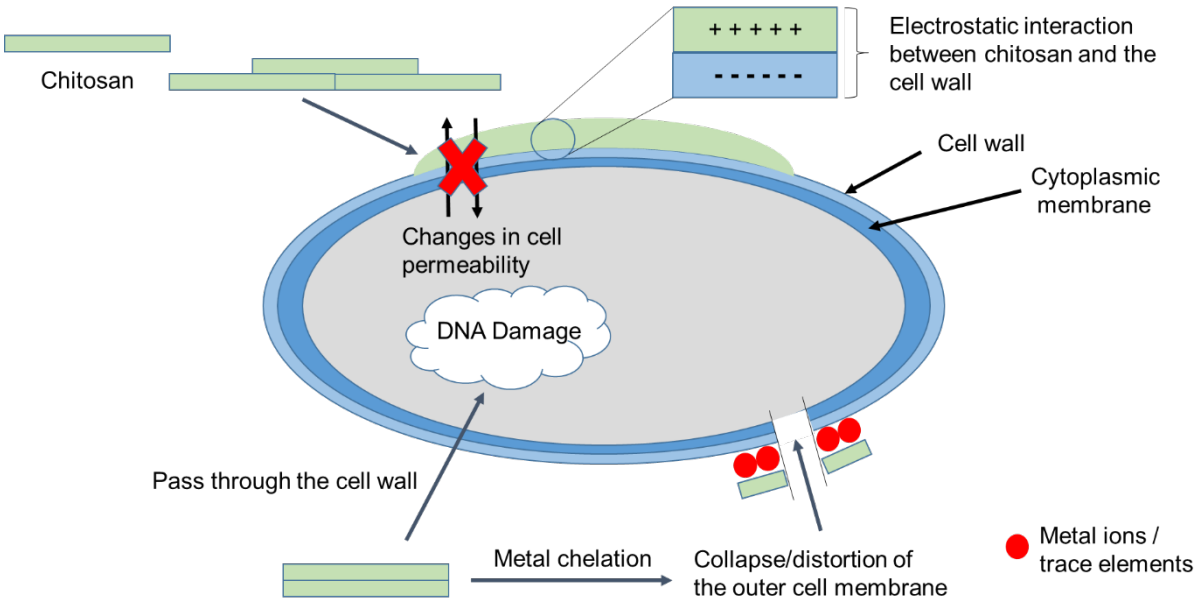

Figure 2.8: Schematic representation of antimicrobial mechanisms of chitosan and its derivatives adapted from Hosseinnejad *et al.*[116].

A fourth mechanism proposes that the amino groups of chitosan chelate the metal ions on the bacterial cell surface. In cases where the pH exceeds the pKa of chitosan, it is suggested that the chelation effect overpowers the electrostatic effect[103]. From previous literature, it is well known that chitosan has excellent metal ion chelating properties[117,118] due to the ability of amine groups in unprotonated form (pH above 6) to donate lone pair electrons metals and forms complexes[103]. Chelation can either take place via the bridge model or by the pendant model. In the bridge model, amine groups of the same or different chitosan chains bind to the metal ions. In the pendant model, metal ions bind to the amine groups forming pendants[119]. Binding of amine groups to divalent metal ions such as Ca^{2+} and Mg^{2+} prevents the production of toxins and the overall growth of the microorganism is retarded[120]. It is only deprotonated chitosan that exhibits this chelating ability. Therefore, when looking at chitosan derivatives where the amine group has been modified with cationic moieties or electron-withdrawing groups this chelating is less likely to be responsible for its antibacterial effects[103].

2.7 Fluorescence

Fluorescent sensors are widely used to detect environmental changes and to visualize the location of biological molecules by the use of fluorescent dyes. Fluorescent labeling in the ultraviolet to the near-infrared region is thus very important for bioanalytical purposes[121]. Labeling with fluorescent compounds can be expanded to a broader range of wavelengths by the use of semiconductor nanocrystals, fluorescent proteins, and organic molecules. Linkages between the sample and the fluorophore may be covalent or noncovalent resulting in conjugates or complexes which exhibit fluorescence over a broad range of wavelengths[121].

2.7.1 Fluorescein

A polycyclic fluorophore, fluorescein, exhibits absorption of electromagnetic radiation at a wavelength of λ_{abs} 490 nm and emission at λ_{em} 512 nm in water. Fluorescein is one of the most utilized fluorescent labels in natural systems. Another advantage of fluorescein is that it exhibits an excitation maximum at 494 nm, very close to the 488 nm spectral line observed with argon laser, which is one of the lasers used in confocal laser-scanning microscopy[121]. Various derivatives of fluorescein exist but the most popular amine-reactive probe is fluorescein 5(6)-isothiocyanate (FITC)[122,123].

To visualize the distribution of fillers such as CNW and ChNW within a certain matrix, fluorescent labeling can be utilized. A simple one-pot procedure described by Junker Nielsen *et al.*[124] can be used to react FITC with the hydroxyl groups in a basic solution on the surface

of CNW and ChNW. **Figure 2.9** illustrates the dual-labeling of CNW with FITC and rhodamine B isothiocyanate (RBITC). It is important to note that only one of these dyes may also be used.

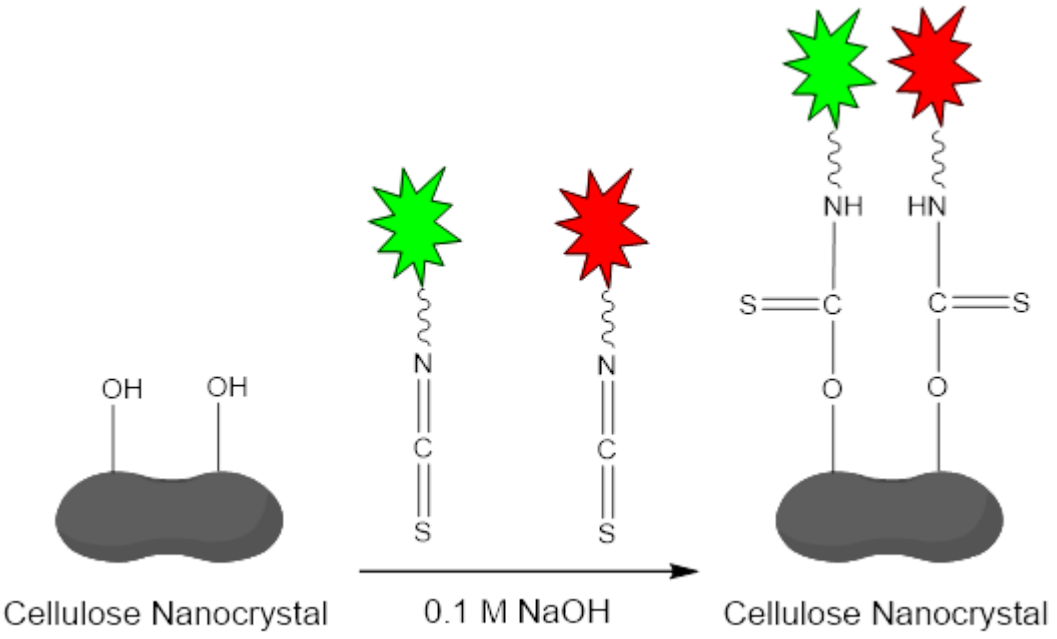

Figure 2.9: The dual-labeling of CNW with FITC (green) and RBITC (red) adapted from Nielsen *et al.*[124].

2.8 References

1 F. Lotfipour, M. Alami-Milani, S. Salatin, A. Hadavi and M. Jelvehgari, *Res. Pharm. Sci.*, 2019, **14**, 175–189.

2 E. M. Ahmed, *J. Adv. Res.*, 2015, **6**, 105–121.

3 H. Zhang, F. Zhang and J. Wu, *React. Funct. Polym.*, 2013, **73**, 923–928.

4 D. N. Iqbal, M. Tariq, S. M. Khan, N. Gull, S. Sagar Iqbal, A. Aziz, A. Nazir and M. Iqbal, *Int. J. Biol. Macromol.*, 2020, **143**, 546–554.

5 C. Peng, J. Xu, G. Chen, J. Tian and M. He, *Int. J. Biol. Macromol.*, 2019, **131**, 336–342.

6 B. Balakrishnan, M. Mohanty, P. R. Umashankar and A. Jayakrishnan, *Biomaterials*, 2005, **26**, 6335–6342.

7 M. Abbas, T. Hussain, M. Arshad, A. R. Ansari, A. Irshad, J. Nisar, F. Hussain, N. Masood, A. Nazir and M. Iqbal, *Int. J. Biol. Macromol.*, 2019, **140**, 871–876.

8 T. Wang, D. Liu, C. Lian, S. Zheng, X. Liu and Z. Tong, *Soft Matter*, 2012, **8**, 774–783.

9 J. Sorber, G. Steiner, V. Schulz, M. Guenther, G. Gerlach, R. Salzer and K. F. Arndt, *Anal. Chem.*, 2008, **80**, 2957–2962.

10 A. Kausar, *J. Plast. Film Sheeting*, 2017, **33**, 384–412.

11 L. Yang, J. S. Chu and J. A. Fix, *Int. J. Pharm.*, 2002, **235**, 1–15.

12 J. Djonlagić and Z. S. Petrović, *J. Polym. Sci. Part B Polym. Phys.*, 2004, **42**, 3987–3999.

13 H. Hamedi, S. Moradi, S. M. Hudson and A. E. Tonelli, *Carbohydr. Polym.*, 2018, **199**, 445–460.

14 O. A. . Monteiro and C. Airoldi, *Int. J. Biol. Macromol.*, 1999, **26**, 119–128.

15 J.-Y. Sun, X. Zhao, W. R. K. Illeperuma, O. Chaudhuri, K. H. Oh, D. J. Mooney, J. J. Vlassak and Z. Suo, *Nature*, 2012, **489**, 133–6.

16 V. I. Lozinsky, I. Y. Galaev, F. M. Plieva, I. N. Savina, H. Jungvid and B. Mattiasson,

Trends Biotechnol., 2003, **21**, 445–451.

17 V. I. Lozinsky, *Russ. Chem. Rev.*, 2002, **71**, 489–511.

18 V. I. Lozinsky, *Russ. Chem. Rev.*, 1998, **67**, 573–586.

19 M. Mincea, A. Negrulescu and V. Ostafe, *Rev. Adv. Mater. Sci.*, 2012, **30**, 225–242.

20 R. A. A. Muzzarelli, *Cell. Mol. Life Sci.*, 1997, **53**, 131–140.

21 J. R. Khurma, D. R. Rohindra and A. V. Nand, *J. Macromol. Sci. - Pure Appl. Chem.*, 2006, **43**, 749–758.

22 T. Chivangkul, S. Pengprecha, P. Padungros, K. Siraleartmukul, S. Prasongsuk and N. Muangsin, *Carbohydr. Polym.*, 2014, **108**, 224–231.

23 D. Wei, Q. Liu, Z. Liu, J. Liu, X. Zheng, Y. Pei and K. Tang, *Int. J. Biol. Macromol.*, 2019, **135**, 561–568.

24 D. K. Mishra, K. S. Yadav, B. Prabhakar and R. S. Gaud, *Nanocomposite for cancer targeted drug delivery*, Elsevier Inc., 2018.

25 M. Aslam, M. A. Kalyar and Z. A. Raza, *Polym. Eng. Sci.*, 2018, **58**, 2119–2132.

26 J. N. Tiwari, R. N. Tiwari and K. S. Kim, *Prog. Mater. Sci.*, 2012, **57**, 724–803.

27 X. Han, Z. Zhang and Z. L. Wang, *Nano*, 2007, **02**, 249–271.

28 A. Watthanaphanit, P. Supaphol, H. Tamura, S. Tokura and R. Rujiravanit, *J. Appl. Polym. Sci.*, 2008, 890–899.

29 M. Peesan, R. Rujiravanit and P. Supaphol, *Polym. Test.*, 2003, **22**, 381–387.

30 J. Sriupayo, P. Supaphol, J. Blackwell and R. Rujiravanit, *Carbohydr. Polym.*, 2005, **62**, 130–136.

31 P. Aksungur, A. Sungur, S. Ünal, A. B. Iskit, C. A. Squier and S. Şenel, *J. Control. Release*, 2004, **98**, 269–279.

32 N. Ben Halima, *RSC Adv.*, 2016, **6**, 39823–39832.

33 E. Marin, J. Rojas and Y. Ciro, *African J. Pharm. Pharmacol.*, 2014, **8**, 674–684.

34 M. Aslam, M. A. Kalyar and Z. A. Raza, *Appl. Phys. A Mater. Sci. Process.*, 2017, **123**, 1–12.

35 R. K. Tubbs, *J. Polym. Sci. Part A-1 Polym. Chem.*, 2003, **4**, 623–629.

36 C. C. Demerlis and D. R. Schoneker, 2003, **41**, 319–326.

37 G. Siqueira, J. Bras and A. Dufresne, *Polymers (Basel).*, 2010, **2**, 728–765.

38 Majid Ali, *J. Civ. Eng. Constr. Technol.*, 2012, **3**, 80–89.

39 S. Srisuwan, N. Prasoetsopha, N. Suppakarn and P. Chumsamrong, *Energy Procedia*, 2014, **56**, 19–25.

40 A. Gandini, *Monomers, Polymers and Composites*, 2008.

41 A. Bledzik and J. Gassan, *Prog. Polym. Sci.*, 1993, **24**, 221–74.

42 L. Heux, E. Dinand and M. R. Vignon, *Carbohydr. Polym.*, 1999, **40**, 115–124.

43 E. Brännvall, *Aspect on Strength Delivery and Higher Utilisation of Strength Potential of Soft Wood Kraft Pulp Fibres*, 2007.

44 M. J. John and S. Thomas, *Carbohydr. Polym.*, 2008, **71**, 343–364.

45 E. Dinand, M. Vignon, H. Chanzy and L. Heux, *Cellulose*, 2002, **9**, 7–18.

46 J. Sugiyama, J. Persson and H. Chanzy, *Macromolecules*, 1991, **24**, 2461–2466.

47 I. M. Saxena and R. M. Brown, *Ann. Bot.*, 2005, **96**, 9–21.

48 R. C. R. Nunes, *Rubber nanocomposites with nanocellulose*, Elsevier Ltd, 2017.

49 A. C. O'sullvian, *Cellulose*, 1997, **4**, 173–207.

50 R. H. Atalla and D. L. Van der Hart, *Science*, 1984, **223**, 283–285.

51 J. Sugiyama, T. Okano, H. Yamamoto and F. Horii, *Macromolecules*, 1990, **23**, 3196–3198.

52 J. Sugiyama, R. Vuong and H. Chanzy, *Macromolecules*, 1991, **24**, 4168–4175.

53 M. M. De Souza Lima and R. Borsali, *Macromol. Rapid Commun.*, 2004, **25**, 771–787.

54 X. M. Dong, J. F. Revol and D. G. Gray, *Cellulose*, 1998, **5**, 19–32.

55 J. Araki, M. Wada, S. Kuga and T. Okano, *Colloids Surfaces A Physicochem. Eng. Asp.*, 1998, **142**, 75–82.

56 S. Beck-Candanedo, M. Roman and D. G. Gray, *Biomacromolecules*, 2005, **6**, 1048–1054.

57 H. Angellier, J. L. Putaux, S. Molina-Boisseau, D. Dupeyre and A. Dufresne, *Macromol. Symp.*, 2005, **221**, 95–104.

58 D. Bondeson, A. Mathew and K. Oksman, *Cellulose*, 2006, **13**, 171–180.

59 A. Hirai, O. Inui, F. Horii and M. Tsuji, *Langmuir*, 2009, **25**, 497–502.

60 C. Bonini, L. Heux, J.-Y. Cavaillé, P. Lindner, C. Dewhurst and P. Terec, *Langmuir*, 2002, **18**, 3311–3314.

61 V. Favier, H. Chanzy and J. Y. Cavaille, *Macromolecules*, 1995, **28**, 6365–6367.

62 W. Thielemans, C. R. Warbey and D. A. Walsh, *Green Chem.*, 2009, **11**, 531–537.

63 Y. Habibi, A. L. Goffin, N. Schiltz, E. Duquesne, P. Dubois and A. Dufresne, *J. Mater. Chem.*, 2008, **18**, 5002–5010.

64 M. A. S. A. Samir, F. Alloin, M. Paillet and A. Dufresne, *Macromolecules*, 2004, **37**, 4313–4316.

65 J. Li, J. -F. Revol and R. H. Marchessault, *J. Appl. Polym. Sci.*, 2002, **65**, 373–380.

66 M. Rani, A. Agarwal and Y. S. Negi, *J. Biomater. Nanobiotechnol.*, 2011, **02**, 71–84.

67 R. Siala, I. Hammemi, S. Sellimi, T. Vallaeys, A. S. Kamoun and M. Nasri, *Adv. Biosci. Biotechnol.*, 2015, **06**, 105–119.

68 P. M. Visakh and S. Thomas, *Waste and Biomass Valorization*, 2010, **1**, 121–134.

69 A. Mera, J. Araki and T. Ohtsuki, *J. Biotechnol. Biomater.*, 2011, **01**, 1–6.

70 J. P. Wang, Y. Z. Chen, S. J. Yuan, G. P. Sheng and H. Q. Yu, *Water Res.*, 2009, **43**, 5267–5275.

71 J. Li, J. -F. Revol and R. H. Marchessault, *J. Appl. Polym. Sci.*, 1997, **65**, 373–380.

72 S. Gautier, E. Xhauflaire-Uhoda, P. Gonry and G. E. Piérard, *Int. J. Cosmet. Sci.*, 2008, **30**, 459–469.

73 M. Potara, E. Jakab, A. Damert, O. Popescu, V. Canpean and S. Astilean, *Nanotechnology*, 2011, **22**, 135101.

74 X. Jiang, K. Cai, J. Zhang, Y. Shen, S. Wang and X. Tian, *J. Hazard. Mater.*, 2011, **185**, 1482–1488.

75 R. Jayakumar, N. Nwe, S. Tokura and H. Tamura, *Int. J. Biol. Macromol.*, 2007, **40**, 175–181.

76 M. Mattioli-Belmonte, A. Zizzi, G. Lucarini, F. Giantomassi, G. Biagini, G. Tucci, F. Orlando, M. Provinciali, F. Carezzi and P. Morganti, *J. Bioact. Compat. Polym.*, 2007, **22**, 525–538.

77 T. Lertwattanaseri, N. Ichikawa, T. Mizoguchi, Y. Tanaka and S. Chirachanchai, *Carbohydr. Res.*, 2009, **344**, 331–335.

78 J. F. Revol and R. H. Marchessault, *Int. J. Biol. Macromol.*, 1993, **15**, 329–335.

79 R. J. Samuels, *J. Polym. Sci. Polym. Phys. Ed.*, 2003, **19**, 1081–1105.

80 Y. Fan, T. Saito and A. Isogai, *Biomacromolecules*, 2008, **9**, 192–198.

81 M. Paillet and A. Dufresne, *Macromolecules*, 2001, **34**, 6527–6530.

82 A. Morin and A. Dufresne, *Macromolecules*, 2002, **35**, 2190–2199.

83 I. Younes and M. Rinaudo, *Mar. Drugs*, 2015, **13**, 1133–1174.

84 H. P. Zhao, X. Q. Feng and H. Gao, *Appl. Phys. Lett.*, 2007, **90**, 97–99.

85 B. M. Min, S. W. Lee, J. N. Lim, Y. You, T. S. Lee, P. H. Kang and W. H. Park, *Polymer (Guildf).*, 2004, **45**, 7137–7142.

86 S. Ifuku, M. Nogi, K. Abe, M. Yoshioka, M. Morimoto, H. Saimoto and H. Yano, *Biomacromolecules*, 2009, **10**, 1584–1588.

87 Y. Lu, L. Weng and L. Zhang, *Biomacromolecules*, 2004, **5**, 1046–1051.

88 K. Gopalan Nair and A. Dufresne, *Biomacromolecules*, 2003, **4**, 657–665.

89 D. Kafetzopoulos, A. Martinou and V. Bouriotis, *Proc. Natl. Acad. Sci.*, 2006, **90**, 2564–2568.

90 Y. Y. Jo, K. J. Jo, Y. L. Jin, W. J. Jung, J. H. Kuk, K. Y. Kim, T. H. Kim and R. D. Park, *J. Microbiol. Biotechnol.*, 2003, **13**, 960–968.

91 A. V Ilyina, N. Y. Tatarinova and V. P. Varlamov, *Process Biochem.*, 1999, **34**, 875–878.

92 H. K. No and S. P. Meyers, *J. Aquat. Food Prod. Technol.*, 2005, **4**, 27–52.

93 S. Hajji, I. Younes, O. Ghorbel-Bellaaj, R. Hajji, M. Rinaudo, M. Nasri and K. Jellouli, *Int. J. Biol. Macromol.*, 2014, **65**, 298–306.

94 S. V. Nemtsev, A. I. Gamzazade, S. V. Rogozhin, V. M. Bykova and V. P. Bykov, *Appl. Biochem. Microbiol.*, 2002, **38**, 521–526.

95 K. L. B. Chang, G. Tsai, J. Lee and W.-R. Fu, *Carbohydr. Res.*, 1997, **303**, 327–332.

96 K. Kurita, T. Sannan and Y. Iwakura, *Makromol. Chemie*, 1977, **178**, 3197–3202.

97 S. ichi Aiba, *Int. J. Biol. Macromol.*, 1991, **13**, 40–44.

98 I. Tsigos, A. Martinou, D. Kafetzopoulos and V. Bouriotis, *TibTech*, 2000, **18**, 129–135.

99 I. Tsigos and V. Bouriotis, *J. Biol. Chem.*, 1995, **270**, 26286–26286.

100 X.-D. Gao, T. Katsumoto and K. Onodera, *J. Biotechnol.*, 1995, **117**, 257–263.

101 C. Alfonso, O. M. Nuero, F. Santamaría and F. Reyes, *Curr. Microbiol.*, 1995, **30**, 49–54.

102 P. Sahariah, V. S. Gaware, R. Lieder, S. Jónsdóttir, M. Hjálmarsdóttir, O. E. Sigurjonsson and M. Másson, *Mar. Drugs*, 2014, **12**, 4635–4658.

103 P. Sahariah and M. Másson, *Biomacromolecules*, 2017, **18**, 3846–3868.

104 M. Kong, X. G. Chen, K. Xing and H. J. Park, *Int. J. Food Microbiol.*, 2010, **144**, 51–63.

105 G. Geisberger, E. B. Gyenge, D. Hinger, A. Käch, C. Maake and G. R. Patzke, *Biomacromolecules*, 2013, **14**, 1010–1017.

106 M. Kaya, Y. S. Cakmak, T. Baran, M. Asan-Ozusaglam, A. Mentes and K. O. Tozak,

Biotechnol. Bioprocess Eng., 2014, **19**, 58–69.

107 E. I. Rabea, M. E. I. Badawy, W. Steurbaut and C. V. Stevens, *Eur. Polym. J.*, 2009, **45**, 237–245.

108 L. J. Pei, Z. S. Cai, S. Bin Shang and Z. Q. Song, *Chem. Ind. For. Prod.*, 2014, **34**, 44–50.

109 N. A. Mohamed and N. A. Abd El-Ghany, *Int. J. Polym. Mater. Polym. Biomater.*, 2017, **66**, 410–415.

110 L. Hu, X. Meng, R. Xing, S. Liu, X. Chen, Y. Qin, H. Yu and P. Li, *Bioorganic Med. Chem. Lett.*, 2016, **26**, 4548–4551.

111 Y. C. Chung and C. Y. Chen, *Bioresour. Technol.*, 2008, **99**, 2806–2814.

112 A. B. Vishu Kumar, M. C. Varadaraj, L. R. Gowda and R. N. Tharanathan, *Biochem. J.*, 2006, **391**, 167–175.

113 R. C. Goy, D. De Britto and O. B. G. Assis, 2009, **19**, 241–247.

114 E. I. Rabea, M. E. T. Badawy, C. V. Stevens, G. Smagghe and W. Steurbaut, *Biomacromolecules*, 2003, **4**, 1457–1465.

115 D. Raafat and H. G. Sahl, *Microb. Biotechnol.*, 2009, **2**, 186–201.

116 M. Hosseinnejad and S. M. Jafari, *Int. J. Biol. Macromol.*, 2016, **85**, 467–475.

117 D. Kołodyńska, *Chem. Eng. J.*, 2012, **179**, 33–43.

118 D. Liu, Z. Li, Y. Zhu, Z. Li and R. Kumar, *Carbohydr. Polym.*, 2014, **111**, 469–476.

119 E. Guibal, *Sep. Purif. Technol.*, 2004, **38**, 43–74.

120 Y. C. Chung, H. L. Wang, Y. M. Chen and S. L. Li, *Bioresour. Technol.*, 2003, **88**, 179–184.

121 M. S. T. Goncalves, *ChemInform*, 2009, **40**, 190–212.

122 C. Hoffmann, J. Leroy-Dudal, S. Patel, O. Gallet and E. Pauthe, *Anal. Biochem.*, 2008, **372**, 62–71.

123 L. Fülöp, B. Penke and M. Zarándi, *J. Pept. Sci.*, 2001, **7**, 397–401.

124 L. J. Nielsen, S. Eyley, W. Thielemans and J. W. Aylott, *Chem. Commun.*, 2010, **46**, 8929–8931.

Chapter 3: Experimental

3.1 Introduction

In this chapter, the materials, experimental methods, and characterization techniques adopted for this study are outlined and discussed.

Primary, binary, and ternary hydrogel blends were fabricated by combining PVA and the respective polymers in a suitable ratio via methods discussed in Section 3.3. This was followed by the characterization of the neat polymers as well as the hydrogel blends as discussed in Section 3.4. The fillers used in these hydrogel blends were characterized by transmission electron microscopy (TEM), confocal fluorescence microscopy (CFM), as well as attenuated total reflectance-Fourier, transform infrared spectroscopy (ATR-FTIR). The hydrogel blends were characterized by scanning electron microscopy (SEM), confocal fluorescence microscopy (CFM), gravimetrical methods, and rheological methods. Thermal analysis included thermogravimetric analysis (TGA) and differential scanning calorimetry (DSC). Antimicrobial studies were performed to visualize the effect the different fillers and filler loadings have on the hydrogel blends.

3.2 Materials

Chitosan (medium molecular weight; degree of deacetylation, 75 – 85%), chitin from shrimp shells (practical grade, powder), fluorescein 5(6)-isothiocyanate (≥90%, HPLC), isopropyl alcohol, methanol, nitrotetrazolium blue chloride, alamarBlue (resazurin), Luria Bertani media, poly(vinyl alcohol) (M_w 89,000-98,000, 99+% hydrolysed), and deuterium chloride (DCl) (99 atom% D) were purchased from Sigma-Aldrich. Sodium hydroxide was purchased from Scienceworld. Monochloric acetic acid was purchased from Acros Organics. Deuterium oxide (D_2O) (99.96 atom% D), Dimethyl sulfoxide - *d6* (DMSO-*d6*) (99.8 atom% D), hydrochloric acid (32%), glacial acetic acid (100%), and sulfuric acid (96 wt%) was purchased from Merck. Distilled deionized water was produced in the laboratory by an Elga Purelab instrument. The microcrystalline cellulose (MCC), from which the CNWs were isolated was obtained from JRS Pharma, with the product name VIVAPUR101. All the chemicals were used as received from the supplier.

3.3 Methods

3.3.1 Isolation of chitin nanowhiskers by acid hydrolysis

A similar method to that used by Mincea *et al.*[1] was used to isolate ChNW by the acid hydrolysis of chitin. A solution of 3.0 M hydrochloric acid (90 mL) was prepared whereafter it was added to chitin (3.0 g) in a round bottom flask with a stir bar. The reaction was then stirred at 105 °C for four hours; ice-cold water (90 mL) was then added to dilute the reaction mixture. Centrifuging at 4000 rpm for 5 minutes followed to wash away the larger, unwanted particles. The centrifugation step was repeated six times (or until the supernatant was clear), making sure the solution is homogeneous after each cycle. After centrifugation, the supernatant was transferred into dialysis tubes and placed in distilled deionized water for 7-10 days whilst changing the distilled deionized water three times per day. After this, the solution was lyophilized to obtain the dried ChNW.

3.3.2 Isolation of cellulose nanowhiskers by acid hydrolysis

Microcrystalline cellulose (MCC) was subjected to hydrolysis by sulphuric acid using a similar process as described by Bondeson *et al.*[2]. To MCC (1 g) a 64 wt% solution of sulphuric acid (8.75 mL) was added dropwise whilst stirring vigorously with an overhead stirrer. The beaker with the MCC was kept in an ice bath to prevent temperature-induced crosslinking. The ice bath was removed and the reaction temperature was increased to 45 °C whilst stirring at 800 rpm for 2 hours. Hydrolysis was then terminated by diluting, tenfold, with cold deionized water. The resulting suspension was then subjected to centrifugation to remove the remaining acid and dissolved amorphous regions. The supernatant was replaced with deionized water as solvent after centrifugation. Centrifugation was repeated until the supernatant became turbid. This turbid suspension which contained the cellulose nanowhiskers was collected. Centrifugation was continued with the collection of the turbid suspension and replacement of the supernatant with deionized water until the supernatant became clear. The collected supernatant was then subjected to dialysis to neutralize the solution and to remove any remaining acid or impurities. This was followed by lyophilization to obtain the dried CNW.

3.3.3 Fluorescent labeling of chitin nanowhiskers and cellulose nanowhiskers

Fluorescein 5(6)-isothiocyanate (FITC) was used to fluorescently label the ChNW and CNW. A one-pot procedure, adapted from a multistep procedure by Nielsen *et al.*[3] was used. FITC reacts with the alkoxide groups of cellulose in an alkaline solution to form thiocarbamate bonds[3]. ChNW or CNW (500 mg) was suspended in sodium hydroxide (0.1 M, 50 mL) in a round bottom flask before adding FITC (21.6 mg, 5.55 x 10^{-5} mol)[3]. This mixture was stirred in

the absence of light for 72 hours at room temperature. The solution was then extensively washed by centrifugation with 0.1 M sodium hydroxide solution until the supernatant became clear. The remaining pellet was suspended in sodium hydroxide (0.1 M, 250 mL) and dialyzed for a few days, changing the distilled deionized water three times a day to neutralize the solution and to remove impurities. This was followed by lyophilization to obtain the fluorescently tagged ChNW and CNW.

3.3.4 Synthesis of *N*, *O*-carboxymethyl chitosan

A 250 mL round bottom flask was charged with chitosan (5 g) and isopropyl alcohol (50 mL). This slurry was then stirred at 25 °C until mixed thoroughly. To this slurry, 10 N aqueous NaOH (12.6 mL, 0.126 mol) was added over 20 minutes in 6 equal portions. The slurry was then stirred for a further 45 minutes, whereafter solid monochloroacetic acid (6 g, 0.0635 mol) was added in five equal portions in five-minute intervals. The resulting mixture was then stirred for three hours at 60 °C. Next, cold distilled deionized water (5 mL) was added and the pH of the slurry adjusted to 7 by the addition of glacial acetic acid. The product was then washed with distilled deionized water, filtered, and subsequently washed with a 70% v/v methanol/water mixture. The product was then dried in a vacuum oven, overnight.

3.3.5 Production of primary, binary and ternary hydrogels

3.3.5.1 Production of primary hydrogels

PVA (5 g) was dissolved in deionized water (100 mL) by stirring for 24 hours whilst slowly heating the mixture to 90 °C. This was followed by slowly cooling the solution to room temperature for a few hours with continuous stirring. Primary hydrogels were fabricated from an aqueous solution of PVA by injecting 1 mL of the PVA solution into a polytop. The solution was then subjected to freezing (-20 °C, 18 hours) whereafter it was thawed (room temperature, 4 hours)[4]. The freeze-thaw cycle was repeated for 5 cycles and resulted in a physically crosslinked hydrogel.

3.3.5.2 Production of binary hydrogels

An aqueous solution of PVA was prepared as described earlier in Section 3.3.5.1 whilst both CTS and NOCC was prepared by suspending CTS (3 g) or NOCC (3 g) powder in 1% acetic acid (100 mL), respectively. This solution was then stirred overnight at 40 °C and left to cool to room temperature for a few hours whilst stirring continued. To create binary blends PVA and CTS or NOCC were blended at a ratio of 90:10 (PVA:CTS or PVA:NOCC). This was achieved by transferring 0.9 mL of the PVA solution into a polytop and adding 0.1 mL of either

CTS or NOCC to the polytop to result in a final volume of 1.0 mL. The mixture was then subjected to stirring for an hour followed by sonication for half an hour to ensure homogeneity throughout the sample. The mixture was then subjected to 5 cycles of the freeze-thaw procedure and physically crosslinked hydrogels resulted, as described in Section 3.3.5.1, earlier.

3.3.5.3 Production of ternary hydrogels

PVA and CTS or NOCC solutions were prepared as described in Sections 3.3.5.1 and 3.3.5.2 and blended according to Section 3.3.5.2. Ternary hydrogels were produced by the addition of either ChNW or CNW to the uncrosslinked binary blends. Filler loadings were 1, 2, and 3 wt%, respectively. After the respective fillers were added to the binary mixtures it was subjected to stirring for an hour followed by sonication for half an hour to ensure that the fillers were homogeneously dispersed throughout the matrix. The resulting ternary blends were then subjected to five cycles of the freeze-thaw procedure and resulted in physically crosslinked ternary hydrogel blends.

3.3.6 Rheology

Rheologic measurements were performed on a Molecular Compact Rheometer MCR 500 to quantify the viscoelastic properties of the various hydrogel specimens. Before rheological measurements, all samples were allowed to reach equilibrium swelling in neutral water before measurements were taken. Parallel plates with a diameter of 2.5 cm were used with the distance between the plates kept constant at 1.5 mm for each measurement. Tests were performed on wet samples, with excess water removed by filter paper at a temperature of 32 °C. The linear viscoelastic (LVE) range of the composite samples was determined by using amplitude sweep tests. Amplitude sweep tests were performed at a constant frequency of 10 Hz whilst varying the applied strain from 0.01 – 100%. Frequency sweep tests were performed at a constant strain value of 1% whilst varying the oscillating frequency of 0.1 – 100 Hz.

3.3.7 Swelling studies

Swelling studies were performed to analyze the dynamic swelling behavior of the respective hydrogel blends. Deionized water was used as the swelling agent at ambient temperature and a constant pH of 7. Each sample was weighed on an electronic balance before immersing in water and the mass was noted as m_0. Each sample was then immersed in water for a definite swelling time t_1. After this time the sample was removed and excess water was carefully removed with blotting paper where after the mass was noted as m_1. After this samples were immersed again and the process was repeated until an equilibrium mass was reached (5

hours). One weight measurement was also taken after 24 hours. The normalized swelling ratio (M_t) was used to report the results in units of percentage and was calculated using the following equation[5].

$$M_t = \frac{m_t - m_0}{m_0} \times 100$$

Equation 3.1[5]

3.3.8 Antimicrobial studies

The antimicrobial activity of the materials was tested against a gram-positive (*Staphylococcus aureus* ATCC 25923) by employing a variation of the disk diffusion method. To do this, the *Staphylococcus aureus* test microorganisms were inoculated into Luria Bertani broth (Merck, Darmstadt, Germany) and incubated at 37 ºC for 24 h. Following incubation, the bacterial suspension was diluted to approximately 10^5 colony-forming units/mL and spread plated onto Mueller Hinton agar (MHA) (Merck, Germany) to create a microbial lawn. The fabricated materials were then added to the plates. First, one of the sides of the sample (top part) was exposed to the microorganism for 5 seconds, leading to contact with about 1000 microorganisms per cm^2. The other side of the sample was then placed on the LB agar plates to visualize halo formation. The top part of the samples was then stained with 5 μL of a 3% alamarBlue solution to obtain an immediate result as to whether microbial inhibition is at play. AlamarBlue consists of resazurin which is an oxidation-reduction (REDOX) indicator. The reduced form is called resorufin. When resazurin (blue) is exposed to the metabolic activity of organisms it undergoes reduction to resofurin (pink) and thus alamarBlue is an excellent indicator of cell viability. The plates were then incubated at 37 °C for ± 60 hours and inspected after being stained with nitrotetrazolium blue chloride (NBC) to visualize microbial growth.

3.4 Characterization techniques used

3.4.1 Transmission electron microscopy (TEM)

TEM is a powerful method for the evaluation of the structural morphology[6] of nanoparticles and can be applied to CNW[7,8] as well as ChNW. Morphological analysis of CNW utilizing TEM is well documented[9,10]. The samples were characterized using an FEI Tecnai 20 transmission electron microscope operating at 200kV (Lab6 emitter) that was fitted with a Tridiem energy filter and Gatan CCD camera (Gatan, UK). Each of the CNWs and ChNWs was diluted to 0.01 wt% and transferred to a carbon-coated TEM grid. The CNW and ChNW were then negatively stained with a solution of uranyl acetate where after the excess solution was blotted with filter

paper and the grids were left until completely dry before analysis was carried out. Images obtained were analyzed with the use of Carl Zeiss AxioVision LE image processing software.

3.4.2 Fluorescence spectroscopy

The analysis was performed on a Perkin Elmer LS 50 B luminescence spectrometer. Before analysis, ChNWs and CNWs were suspended in distilled water which resulted in a 2 wt% solution of the respective nanofillers. This solution was then transferred to a spectrometer cuvette and the absorbance was measured between 200 and 600 nm prior to processing where the signals resulting from the lasers were excluded. These wavelengths were chosen because in water FITC exhibits an excitation peak at 490 nm and an emission peak at 520 nm[3].

3.4.3 Confocal fluorescence microscopy (CFM)

Samples were analyzed by confocal fluorescence microscopy (CFM) to visualize the distribution of the ChNW. A Carl Zeiss Confocal LSM 780 Elyra S1 with SR-SIM super-resolution microscopy was used. The lasers employed had a wavelength of 488 nm and a magnification of 40x was used to visualize filler (CNW/FITC or ChNW/FITC) distribution throughout the matrix. Sample preparation included the production of hydrogels with labeled fillers as discussed earlier but in a CFM sample tray rather than a polytop.

Nanofillers were also analyzed by CFM to confirm the attachment of FITC to the CNW and ChNW fillers. Sample preparation included making a 0.01 wt% suspension of the respective fillers followed by sonication. A drop of this suspension was then transferred to a microscope slide and left to dry.

3.4.4 UV/vis spectroscopy

UV/vis spectroscopy was performed on an Analytic Jena SPECORD 210 PLUS UV/vis spectrophotometer. Prior to analysis, both the ChNWs and the CNWs were suspended, respectively in distilled deionized water, resulting in a 2 wt% suspension. This suspension was transferred into a 1 mL spectrometry cuvette and the absorbance was recorded between 300 and 600 nm.

3.4.5 Attenuated total reflectance-Fourier transform infrared (ATR-FTIR)

Spectra of pure CTS and NOCC were obtained for comparison with the aid of a Thermo Scientific Nicolet iS10 Smart iTR spectrometer. The operation was carried out in transmission mode from 4000 to 400 cm^{-1} with the attenuated total reflectance (ATR) accessory applied. A

background scan was performed before each measurement. Thermo Fisher Scientific Inc. provided the Omnic 8.1 data processing software.

3.4.6 Nuclear magnetic resonance (NMR)

^{13}C NMR spectroscopy in the liquid state was performed on CTS and NOCC using a Varian VXR-Unity, 600 MHz at 25 °C. Samples were prepared by swelling 20 mg of the individual CTS and NOCC in a combination of DMSO-d_6, D_2O (DMSO-d_6:D_2O = 70:30), and a drop of DCl, overnight in a polytop whilst subjecting the sample to stirring. The total volume of each of the NMR spectroscopy samples was 1.0 mL. The sample was then injected into an NMR tube and analysis was performed. Tetramethylsilane (TMS) was used as internal standard (δ = 0 ppm).

3.4.7 Scanning electron microscopy (SEM)

SEM can be applied in many fields. It is an effective method to analyze the surface morphology of inorganic and organic specimens on the micrometer scale. The application of SEM results in detailed grey-scale images. SEM can easily reach magnification of 300000X and in the modern models' magnification of up to 1000000X can be reached[11]. The analysis was carried out on a Carl Zeiss MERLIN SEM instrument at an accelerating voltage of 3.0 kV. Sample preparation included the mounting of samples on SEM stubs followed by conductive carbon coating. The pore diameter distribution was evaluated by using Carl Zeiss AxioVision LE image processing software where 200 measurements were taken to determine the average pore size.

3.4.8 Thermogravimetric analysis (TGA)

In TGA the change in weight as a function of temperature is measured to obtain the decomposition profile of the relevant sample. TGA was conducted on a TGA Q500 instrument to obtain the decomposition profiles of the hydrogel composites. Portions of 2 – 5 mg of the samples were evaluated in a nitrogen atmosphere with a nitrogen flow rate of 60 $mL \cdot min^{-1}$. The heating rate was 10 $°C \cdot min^{-1}$ and the heating profile ranged from 0 °C – 600 °C. This was kept constant for all samples evaluated.

3.4.9 Differential scanning calorimetry (DSC)

Differential Scanning Calorimetry is a sensitive and invaluable technique that can be used to study the thermotropic properties such as crystallization, glass transition, and melting temperature of synthetic and natural macromolecules. DSC thermograms were obtained by

running samples on a DSC Q20 TA instrument. Samples of 3.0 – 5.0 mg were evaluated by placing it into ordinary DSC aluminum pans and then subjecting the samples to the heat profile to record the melting endotherm and the crystallization exotherm. The heating and cooling rate was 10 °C·min^{-1} for all the heating cycles. All samples were subjected to three cycles. The heating profile ranged from -10 °C – 250 °C. In the first cycle, samples were heated to 250 °C and the temperature was kept constant and isothermal for 5 minutes followed by cooling to -10 °C and heating to 250°C. The nitrogen flow rate was 2 mL·min^{-1} and the second and third cycles were evaluated to determine the crystallization exotherm and melting endotherm.

3.5 References

1 M. Mincea, A. Negrulescu and V. Ostafe, *Rev. Adv. Mater. Sci.*, 2012, **30**, 225–242.

2 D. Bondeson, A. Mathew and K. Oksman, *Cellulose*, 2006, **13**, 171–180.

3 L. J. Nielsen, S. Eyley, W. Thielemans and J. W. Aylott, *Chem. Commun.*, 2010, **46**, 8929–8931.

4 T. Abitbol, T. Johnstone, T. M. Quinn and D. G. Gray, *Soft Matter*, 2011, **7**, 2373–2379.

5 J. Liu, X. J. Zheng and K. Y. Tang, 2013, **33**, 452–458.

6 Z. L. Wang, *J. Phys. Chem. B*, 2002, **104**, 1153–1175.

7 G. Siqueira, J. Bras and A. Dufresne, *Polymers (Basel).*, 2010, **2**, 728–765.

8 S. J. Eichhorn, A. Dufresne, M. Aranguren, N. E. Marcovich, J. R. Capadona, S. J. Rowan, C. Weder, W. Thielemans, M. Roman, S. Renneckar, W. Gindl, S. Veigel, J. Keckes, H. Yano, K. Abe, M. Nogi, A. N. Nakagaito, A. Mangalam, J. Simonsen, A. S. Benight, A. Bismarck, L. A. Berglund and T. Peijs, *J. Mater. Sci.*, 2010, **45**, 1–33.

9 Z. Yang, H. Peng, W. Wang and T. Liu, *J. Appl. Polym. Sci.*, 2010, **116**, 2658–2667.

10 N. J. Loader, I. Robertson, A. C. Barker, V. R. Switsur and J. S. Waterhouse, *Chem. Geol.*, 1997, **136**, 313–317.

11 A. Mohammed and A. Abdullah, in *Proceedings of 2018 International Conference on Hydraulics and Pneumatics - HERVEX*, 2018, pp. 85–90.

Chapter 4: Preparation and characterization of chitin nanowhiskers and cellulose nanowhiskers

4.1 Introduction

Chitin nanowhiskers (ChNW) and cellulose nanowhiskers (CNW) were isolated from chitin and MCC, respectively. Even though a range of different isolation methods for the isolation of both ChNWs and CNWs are discussed in literature[1], ChNWs were isolated by means of hydrochloric acid hydrolysis as described by Mincea *et al.*[1] and CNWs were isolated by means of sulphuric acid hydrolysis as described by Bondeson *et al.*[2]. Sulphuric acid hydrolysis was chosen for the hydrolysis of the CNW filler because it induces charged sulfate ester groups on the surface of the cellulose chains[3]. This will reduce the tendency for aggregation in aqueous media, seen when hydrolysis is carried out by using hydrochloric acid[3]. Both the ChNWs and CNWs were lyophilized as a final step to isolate the dried whiskers as described in Sections 3.3.1 and 3.3.2. Isolated ChNW and CNW were both labeled with a marker that exhibits fluorescence, namely fluorescein 5(6)-isothiocyanate (FITC) according to Nielsen *et al.*[3]. To visualize attachment of FITC, labeled ChNWs and CNWs was compared to unlabeled ChNWs and CNWs, respectively, utilizing confocal fluorescence microscopy (CFM). Further characterization techniques employed included transmission electron microscopy (TEM) to visualize the morphology of the ChNW sans CNWs, and fluorescence spectroscopy and UV-vis spectroscopy to confirm the attachment of FITC to the ChNWs and CNWs.

4.2 Transmission electron microscopy (TEM)

The morphology of the ChNWs and CNWs were evaluated by employing TEM. The resulting images were analyzed with the aid of AxioVision LE image processing software to determine the dimensions of the individual nanowhiskers. These values were compared to the values reported in literature[4,5]. TEM images of ChNW and CNW are shown in **Figure 4.1** and **Figure 4.2**, respectively.

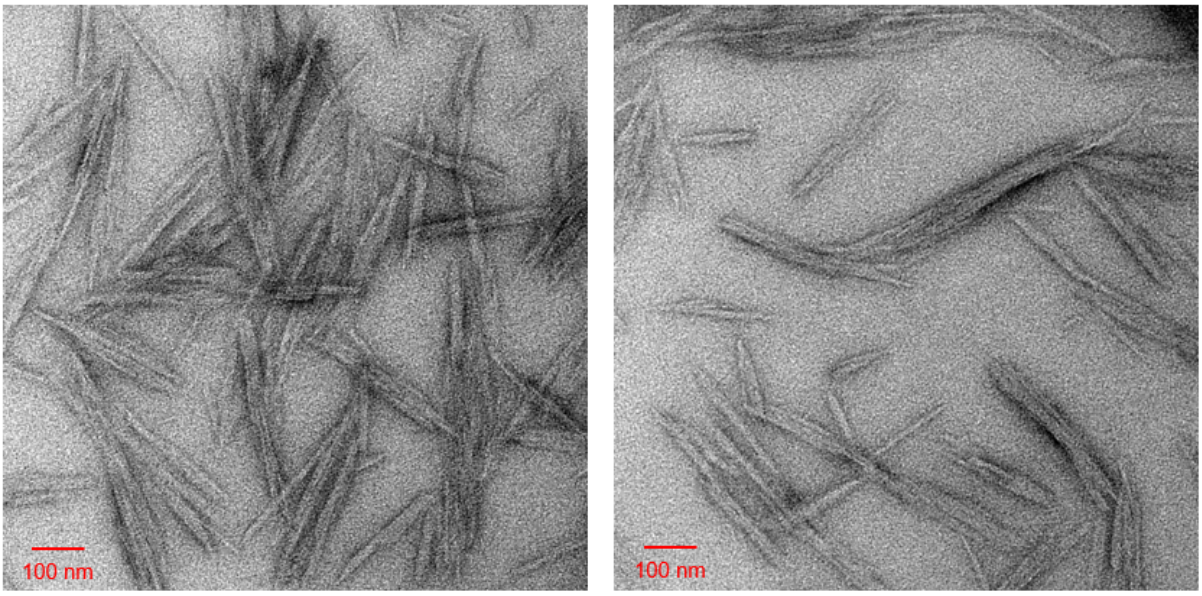

Figure 4.1: TEM images obtained of the ChNW by means of hydrochloric acid hydrolysis.

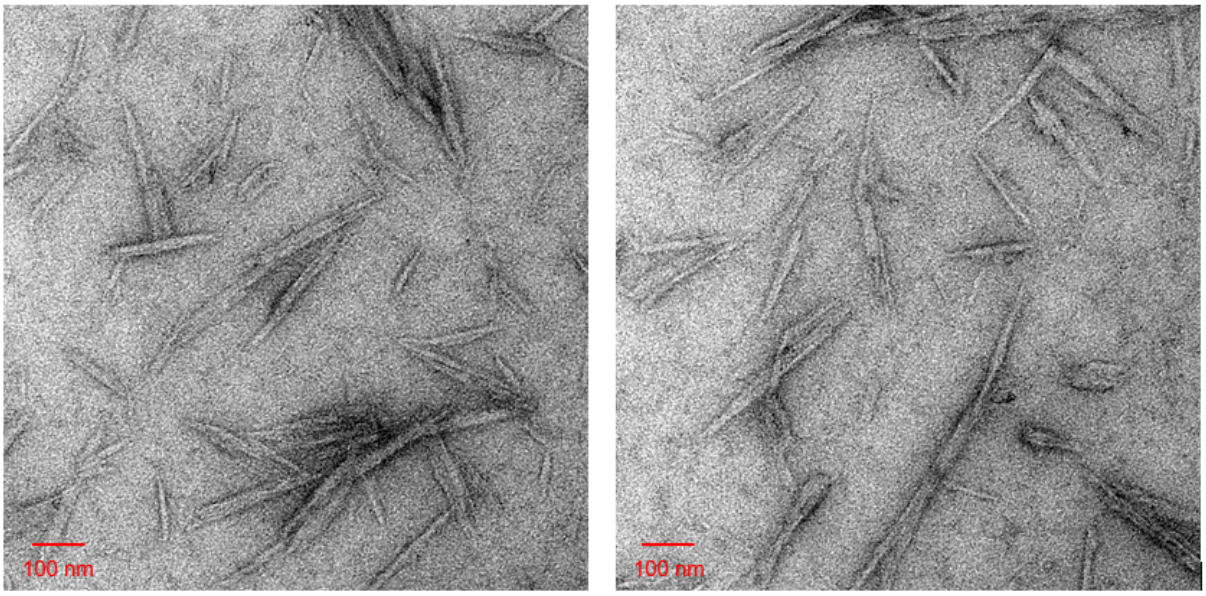

Figure 4.2: TEM images obtained of the CNW by means of sulphuric acid hydrolysis.

TEM images were analyzed and results are reported in **Table 4.1**. An average of 200 measurements on five different images was taken of the length and width of the ChNWs and CNWs, respectively. Histograms displaying the distribution of the measurements can be seen in **Figure 4.3**. It was found that the width of the ChNW varied from 7.00 – 17.0 nm with an average of 11.3 nm whilst their length varied from 95.0 – 266 nm with an average of 170 nm. The average length-to-width aspect ratio was found to be 17.7. This corresponds to values reported in literature[1]. The width of the CNW varied from 3.30 – 17.0 nm with an average width of 10.1 nm whilst their length varied from 86.9 – 266 nm with an average length of 156 nm

and an average length-to-width aspect ratio of 15.4, which corresponds to values reported in literature[5].

Table 4.1: Dimensions of the ChNW and CNW nanofillers

	Average width (nm)	Average length (nm)	Length-to-width aspect ratio
ChNW	11.3 ± 2.29	170 ± 38.9	17.7
CNW	10.1 ± 2.69	156 ± 34.7	15.4

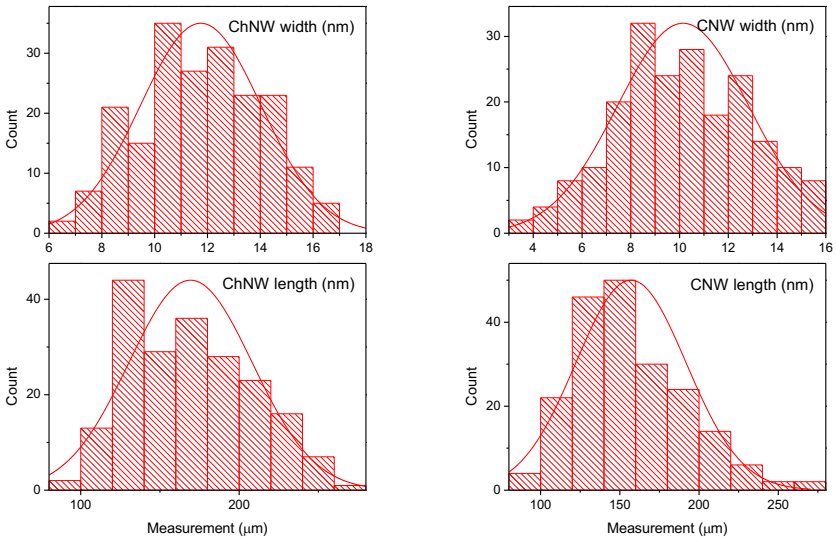

Figure 4.3: Histograms displaying the distribution of the width and length measurements of ChNWs and CNWs.

4.3 Fluorescence

The presence of FITC can be seen visually and attachment was confirmed in Section 4.3.1 and 4.4. Whilst unlabeled nanowhiskers (labeled (a) and (c) in **Figure 4.3**) appeared bright white, their FITC labeled counterparts appeared to have a slight yellow tinge (labeled (b) and (d) in **Figure 4.3**). From now on labeled whiskers will be referred to as either FITC/ChNW in the case of the FITC labeled ChNW or FITC/CNW in the case of the FITC labeled CNW. **Figure 4.3** shows the difference in FITC/ChNW and FITC/CNW compared to ChNW and CNW, respectively.

Figure 4.4: (a), ChNW; (b), FTIC/ChNW; (c), CNW; (d), FITC/CNW.

4.3.1 Fluorescence spectroscopy

Lyophilized FITC/ChNW and FITC/CNW were redispersed in distilled water as described earlier. The analysis was performed to confirm FITC successfully attached to the ChNWs and CNWs, respectively. In water, FITC has an absorption maximum at 490 nm and an excitation maximum at 520 nm[3]. This is observed when looking at the absorption and emission spectra of pure FITC in **Figure 4.5** (a) and (b).

Figure 4.5 (c) and (d) shows the fluorescence spectra obtained from FITC/ChNW and FITC/CNW, respectively. FITC/ChNW and FITC/CNW were extensively washed after the labeling process to ensure that all unreacted dye was removed. Therefore, the peaks observed in (c) and (d) could only be a result of the successful attachment of FITC to the ChNWs and CNWs, respectively.

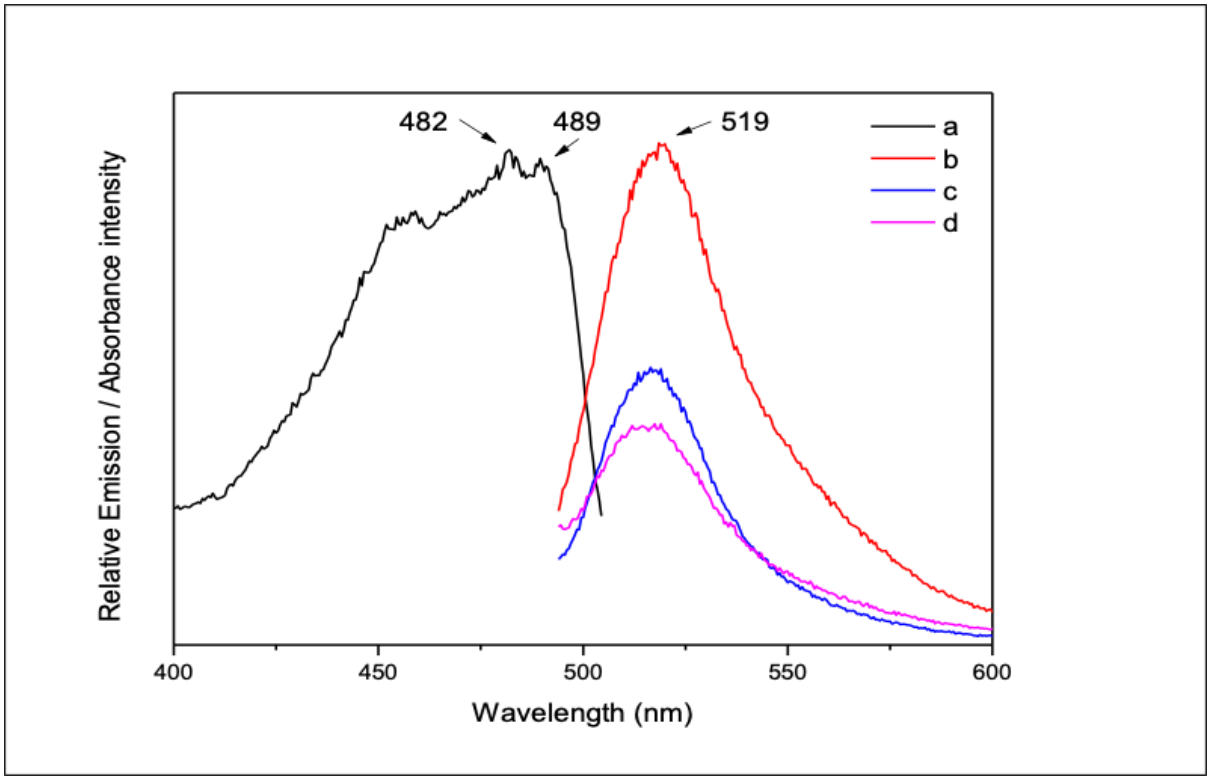

Figure 4.5: (a), Excitation spectrum of (a), an aqueous suspension of FITC (0,05 wt%); (b), emission spectrum of an aqueous suspension FITC (0,05 wt%); (c), emission spectrum of an aqueous suspension of FITC/ChNW (2 wt%); (d), emission spectrum of an aqueous suspension of FITC/CNW (2 wt%)

4.3.2 Confocal fluorescence microscopy (CFM)

Labeled ChNW and CNW were analyzed by employing confocal fluorescence microscopy (CFM).

Unlabeled CNW and ChNW were also analyzed to serve as a control. The CFM results for CNW can be seen in **Figure 4.6** and for ChNW in **Figure 4.8**. The CFM results for FITC/CNW can be seen in **Figure 4.7** and for FITC/ChNW in **Figure 4.9**.

The presence of FITC can be observed in **Figure 4.7** and **Figure 4.9**. This is a good indication that FITC was successfully attached to the CNW and ChNW. When looking at **Figure 4.7 (b)** and **Figure 4.9 (b)**, the rod-like structures can be seen when looking closely although the majority of the nanowhiskers are agglomerated. When the fluorescent signals (**Figure 4.7 (a)** and **Figure 4.9 (a)**) are overlaid with **Figure 4.7 (b)** and **Figure 4.9 (b)** to produce **Figure 4.7 (c)** and **Figure 4.9 (c)** it is also clear that those signals are originating from the same areas as to where the nanowhiskers are found. Pure CNW and ChNW, depicted in **Figure 4.6** and

Figure 4.8 respectively, exhibited no fluorescent signals and thus confirming that the fluorescent signals obtained are only as a consequence of the presence of FITC.

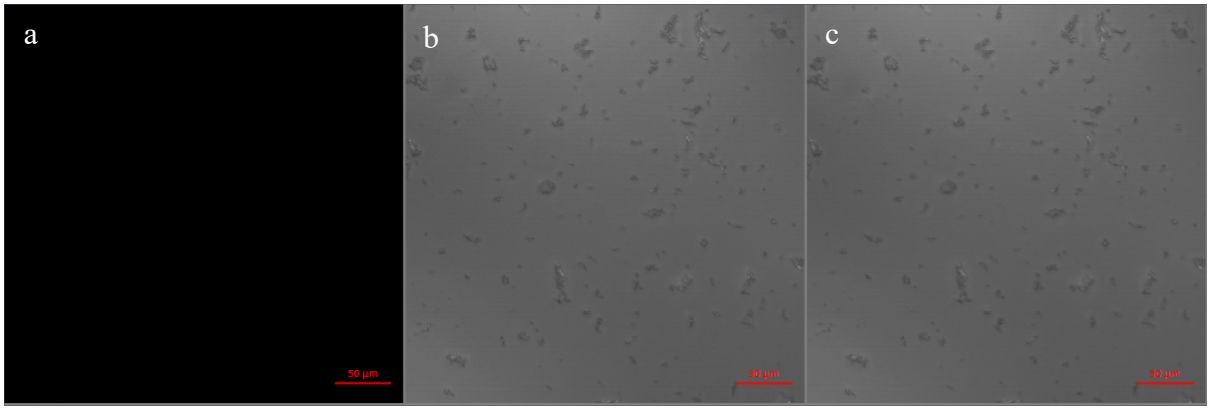

Figure 4.6: CFM images of a CNW dispersion in deionized water (a) 488 nm, (b) T PMT filter, (c) an overlay of images (a) and (b).

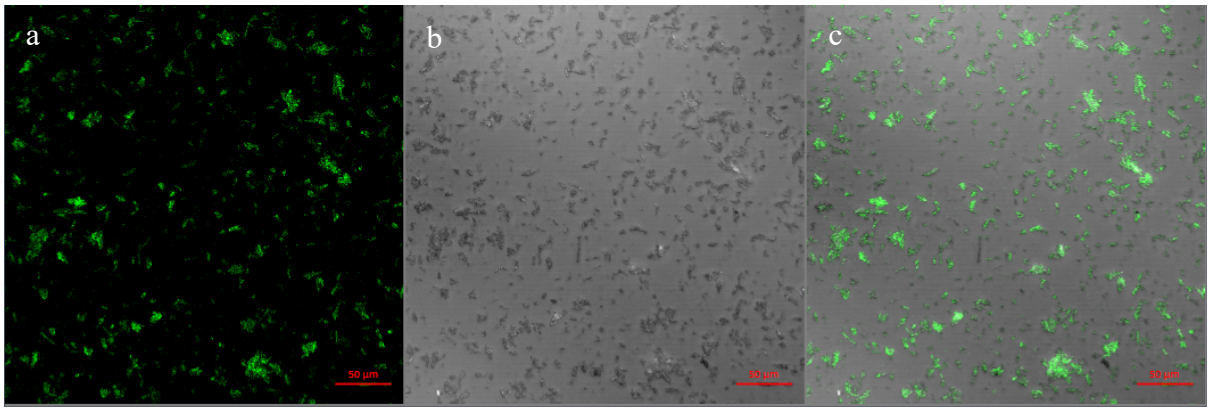

Figure 4.7: CFM images of an FITC/CNW dispersion in deionized water (a) 488 nm, (b) T PMT filter, (c) an overlay of images (a) and (b).

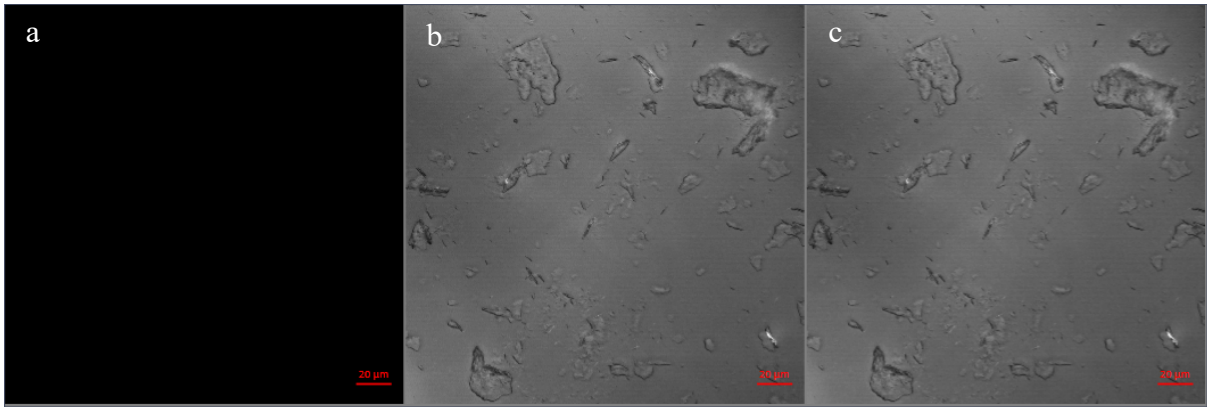

Figure 4.8: CFM images of a ChNW dispersion in deionized water (a) 488 nm, (b) T PMT filter, (c) an overlay of images (a) and (b).

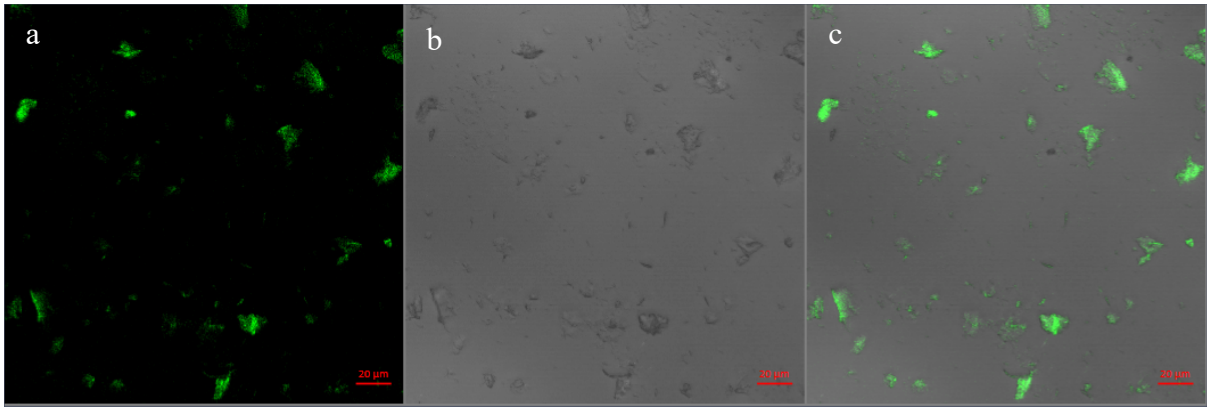

Figure 4.9: CFM images of an FITC/ChNW dispersion in deionized water (a) 488 nm, (b) T PMT filter, (c) an overlay of images (a) and (b).

4.4 UV/vis Spectroscopy

To confirm the attachment of FITC to ChNW and CNW these respective fillers were evaluated by UV/vis spectroscopy between 300 and 600 nm. In water, FITC has an absorption maximum at 490 nm[3]. This can also be observed when looking at **Figure 4.10** and **Figure 4.11** where the UV absorption spectra of FITC as well as the respective fillers can be seen.

As mentioned earlier in Section 4.3.1, the FTIC/ChNW and FITC/CNW were extensively washed after labeling to ensure that all unreacted dye is removed so the absorbance peaks observed in **Figure 4.10** and **Figure 4.11** must be due to the successful attachment of FITC to the respective samples.

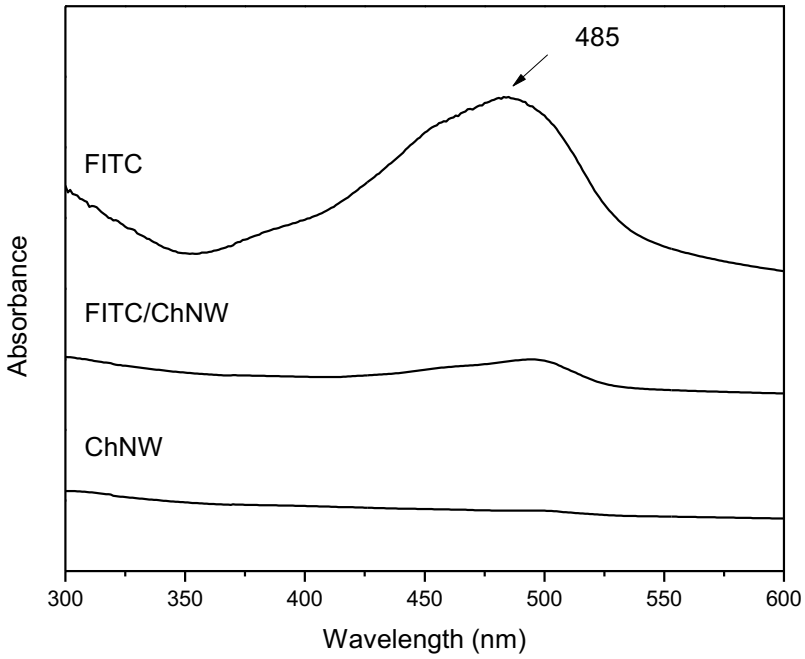

Figure 4.10: The UV/vis spectra of an aqueous suspension of FITC (0,05 wt%), an aqueous suspension of FITC/ChNW (2 wt%), and an aqueous suspension of ChNW (2 wt%)

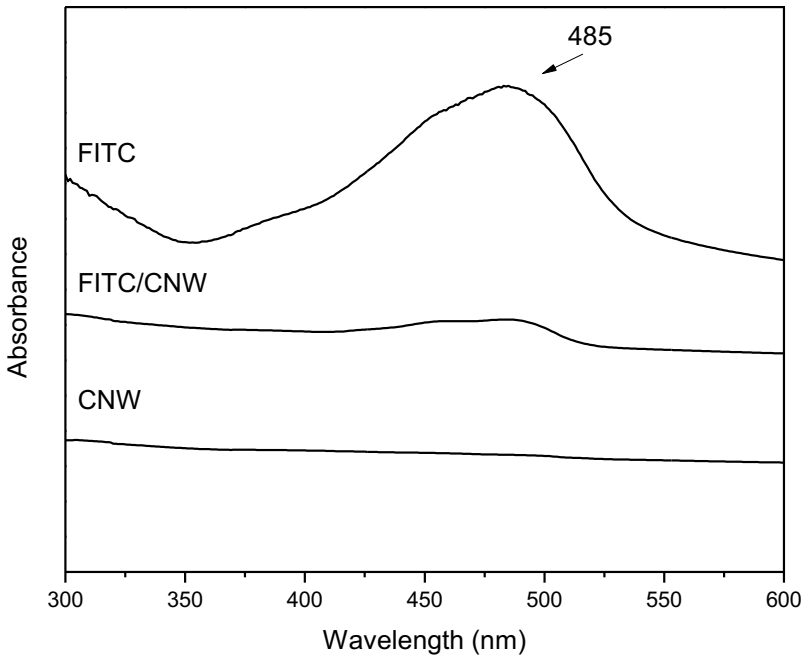

Figure 4.11: The UV/vis spectra of an aqueous suspension of FITC (0,05 wt %), an aqueous suspension of FITC/CNW (2 wt %), and an aqueous suspension of CNW (2 wt %)

4.5 Conclusion

ChNWs and CNWs were successfully isolated via hydrochloric and sulphuric acid hydrolysis, respectively. Morphological analysis by TEM confirmed the presence of the rod-like ChNWs and CNWs. CFM was employed to visually observe the presence of the FITC in the labeled samples and fluorescent signals were easily detected, even in dilute suspensions. The attachment of FITC to the ChNWs and CNWs was confirmed by fluorescence spectroscopy and UV-Vis spectroscopy.

4.6 References

1 M. Mincea, A. Negrulescu and V. Ostafe, *Rev. Adv. Mater. Sci.*, 2012, **30**, 225–242.

2 D. Bondeson, A. Mathew and K. Oksman, *Cellulose*, 2006, **13**, 171–180.

3 E. Mascheroni, R. Rampazzo, M. A. Ortenzi, G. Piva, S. Bonetti and L. Piergiovanni, *Cellulose*, 2016, **23**, 779–793.

4 L. J. Nielsen, S. Eyley, W. Thielemans and J. W. Aylott, *Chem. Commun.*, 2010, **46**, 8929–8931.

5 W. T. Goodrich, J. D. Winter, *Biomacromolecules*, 2007, **8**, 252− 257.

6 Y. Habibi, L. A. Lucia and O. J. Rojas, *Chem. Rev.*, 2010, **110**, 3479–3500.

Chapter 5: Preparation and characterization of NOCC form CTS

5.1 Introduction

Chitosan exhibits a large range of favorable properties for the use in biomedical systems including biodegradability, biocompatibility, non-toxicity, and intrinsic antimicrobial properties against bacteria and fungi[1]. It is, however insoluble in organic/inorganic solvents and water[2,3]. It is only soluble in dilute aqueous acetic acid, formic acid, and lactic acid solutions with pH < 6[3–5]. Chemical derivatization of chitosan can be performed to improve certain properties, such as solubility, hydrophilicity[6], gelling ability, and affinity towards bioactive molecules[7]. Several water-soluble derivatives of chitosan have been reported which have been prepared by quaternization[8] or by the introduction of hydrophilic groups such as hydroxypropyl, dihydroxyethyl, hydroxyalkylamine[9–11], sulfate[12], phosphate or carboxyl groups such as carboxymethyl, carboxyethyl, or carboxybutyl[3].

Chitosan can undergo modification by utilizing either of its two nucleophilic sites, namely its primary amine and its primary hydroxyl group[13]. Nucleophilic substitution through the primary amine facilitates alkylation, carboxylation, acetylation, and quaternization[3]. In comparison to the other water-soluble derivatives of chitosan, carboxymethyl chitosan is well reported on[3]. It is hydrophilic in nature and soluble in either acidic, neutral, or alkaline mediums[5] with ample possible applications[3]. In this study NOCC will be prepared from CTS according to **Figure 5.1** by carboxymethylation of the amine and primary hydroxyl group in CTS, resulting in NOCC.

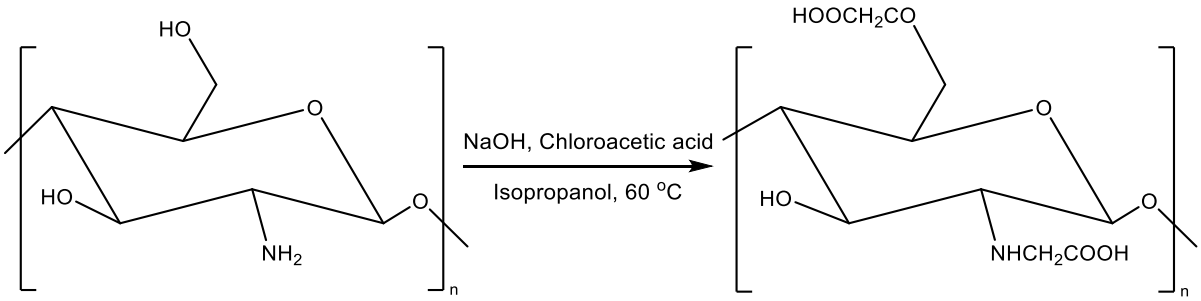

Figure 5.1: Preparation of NOCC from CTS

5.2 Results and discussion

5.2.1 Attenuated total reflectance-Fourier transform infrared (ATR-FTIR)

One of the experimental techniques used to characterize the modification of CTS was ATR-FTIR. The FTIR spectra are shown in **Figure 5.2**. The peak for the primary hydroxyl group (C-O stretch in -CH_2-OH) can be observed at 1029 cm^{-1} [14]. When looking at the peak observed at 3285 cm^{-1} in the spectrum of CTS, it is the stretching vibration of -NH_2 and -OH groups, and the peak at 1650 cm^{-1} is the -NH_2 deformation[4]. Carboxymethylation is indicated in the spectrum of NOCC by the peak at 1600 cm^{-1} which is indicative for a carboxylic acid salt (-COO^- asymmetric stretch)[4,14]. The presence of the stretching vibration of C-O-C at 1321 cm^{-1} in the spectrum of NOCC also indicates successful carboxymethylation[4]. Additionally, the broadening of the peak at 3265 cm^{-1} can also be observed in the spectrum of NOCC which is indicative of carboxymethylation in both the amine and the primary hydroxyl functional group[4].

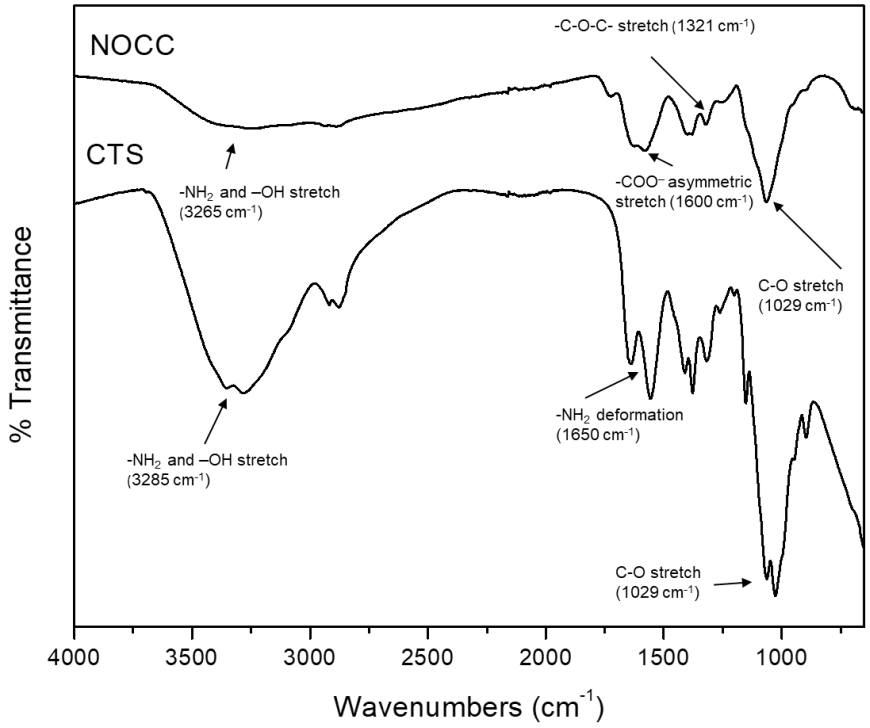

Figure 5.2: The FTIR spectra of NOCC and CTS.

5.2.2 Carbon 13 nuclear magnetic resonance (^{13}C-NMR)

The ^{13}C-NMR spectra of pure CTS and NOCC were obtained to supplement the ATR-FTIR results discussed in Section 4.3.1 and to prove successful carboxymethylation at the oxygen and nitrogen atom in the structure of CTS. The ^{13}C-NMR spectrum for pure CTS is shown in **Figure 5.4** whilst the ^{13}C-NMR spectrum for NOCC is shown in **Figure 5.6**.

5.2.2.1 ^{13}C nuclear magnetic resonance of CTS

The solvent combination used comprised DMSO-*d6*, D_2O (DMSO:D_2O = 70:30), and a drop of DCl. Signals occurring at 173.2 ppm and 23.4 ppm are due to the carbonyl (C7') and methyl carbons (C8') of chitin, respectively[15]. This is due to incomplete deacetylation of chitin during the conversion of chitin to CTS as discussed in Section 2.4.3. The monomeric units of both CTS and chitin can be seen in **Figure 5.3**. The signal at the chemical shift of 98.2 ppm can be assigned to C1, 78.1 ppm to C4, 75.7 ppm to C5, 70.8 ppm to C3, 60.9 ppm to C6, and 56.6 ppm to C2[15].

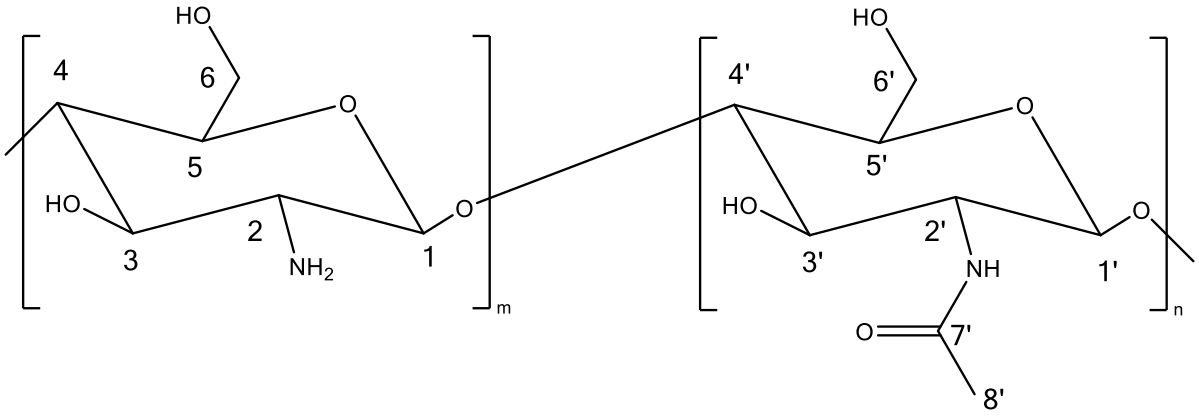

Figure 5.3: The chemical structure of CTS (left) and chitin (right).

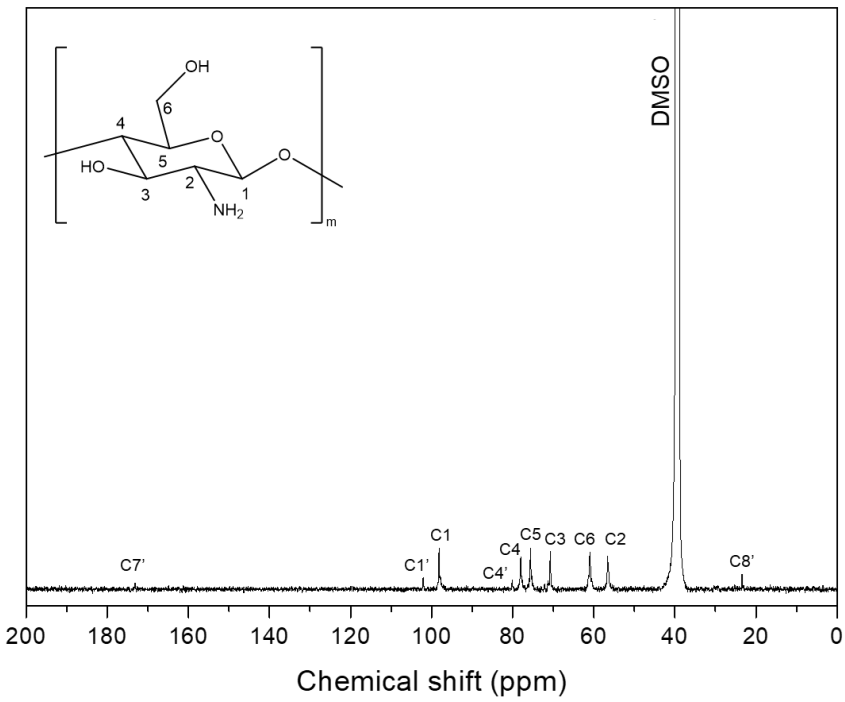

Figure 5.4: ^{13}C-NMR spectrum of CTS.

5.2.2.2 ^{13}C nuclear magnetic resonance of NOCC.

The ^{13}C-NMR spectrum for NOCC is shown in **Figure 5.6**.

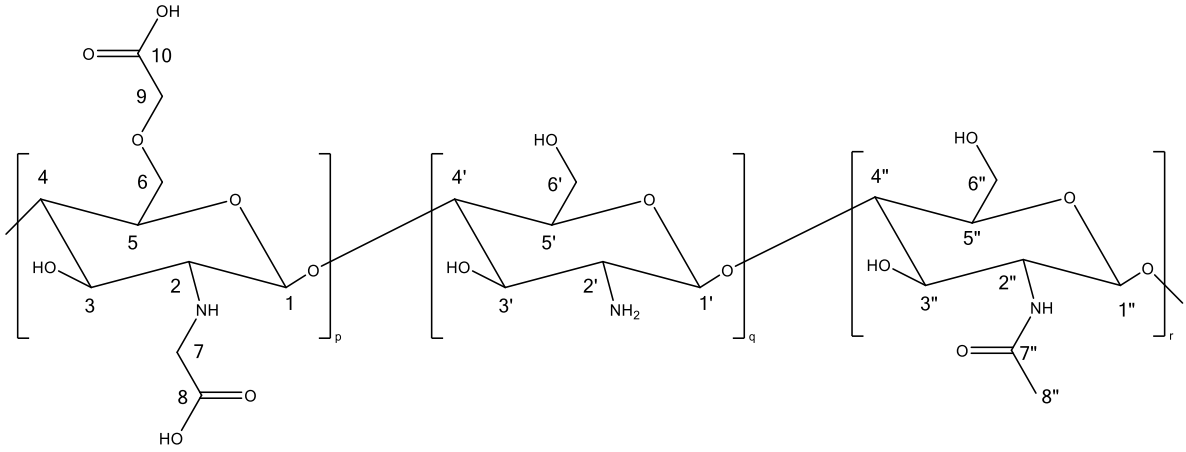

Figure 5.5: The chemical structure of NOCC (left), CTS (middle), and chitin (right).

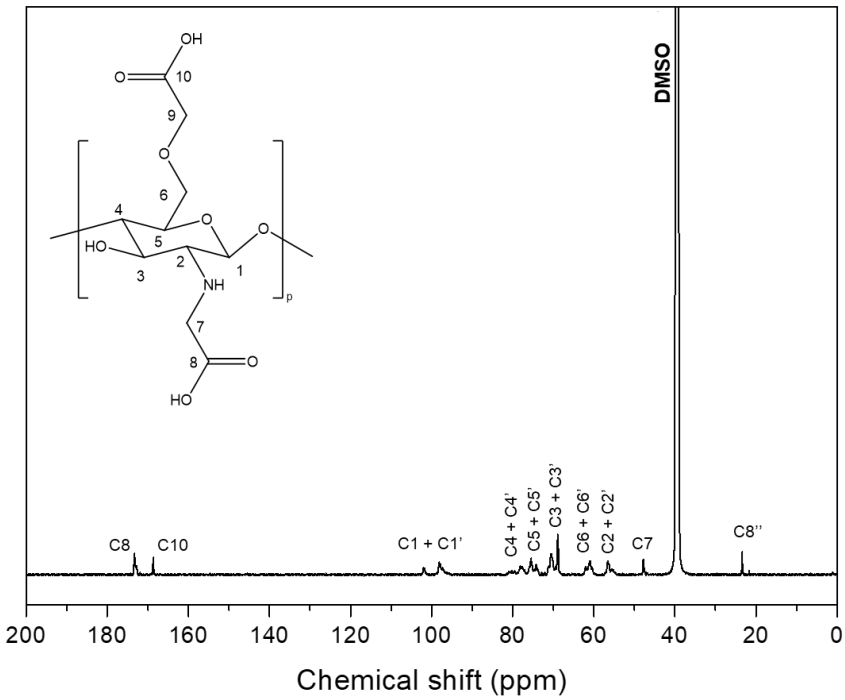

Figure 5.6: ^{13}C-NMR spectrum of NOCC.

The solvent combination used comprised DMSO-*d6*, D_2O (DMSO:D_2O = 70:30), and a drop of DCl to aid the solubility. The signal observed at a chemical shift of 173.4 ppm and 168.7 ppm can be assigned to the carbonyl carbons C8 and C10 respectively[15]. The signal at around 98.3 ppm can be assigned to C1 and C1', 78.1 ppm to C4 and C4', 75.4 ppm to C5 and C5',

69.0 ppm to C3 and C3', 61.0 ppm to C6 and C6', 56.2 ppm to C2 and C2' and 47.7 to C7[15]. The signal observed at 23.4 ppm is due to the methyl carbon (C8'') of chitin[15].

5.3 Conclusion

Carboxymethylation of both the amine and primary hydroxyl group of CTS was successfully achieved to produce a derivative of CTS namely NOCC by the reaction of chitosan with monochloroacetic acid in an alkaline reaction medium. Derivatization was confirmed by comparing the ATR-FTIR and ^{13}C-NMR spectra of pure CTS to that of the resulting NOCC.

5.4 References

1 M. W. Jøraholmen, A. Bhargava, K. Julin, M. Johannessen and N. Škalko-Basnet, *Mar. Drugs*, 2020, **18**, 1–15.

2 M. S. Riaz Rajoka, L. Zhao, H. M. Mehwish, Y. Wu and S. Mahmood, *Appl. Microbiol. Biotechnol.*, 2019, **103**, 1557–1571.

3 V. K. Mourya, N. N. Inamdar and A. Tiwari, *Adv. Mater. Lett.*, 2010, **1**, 11–33.

4 H. S. Kusuma, A. F. Al-sa'bani and H. Darmokoesoemo, *Procedia Food Sci.*, 2015, **3**, 35–51.

5 H. Homayoni, S. A. H. Ravandi and M. Valizadeh, *Carbohydr. Polym.*, 2009, **77**, 656–661.

6 A. Rafique, K. Mahmood Zia, M. Zuber, S. Tabasum and S. Rehman, *Int. J. Biol. Macromol.*, 2016, **87**, 141–154.

7 W. Argüelles-Monal, J. Lizardi-Mendoza, D. Fernández-Quiroz, M. Recillas-Mota and M. Montiel-Herrera, *Polymers (Basel).*, 2018, **10**, 342–343.

8 Z. Jia, D. Shen and W. Xu, *Carbohydr. Res.*, 2001, **333**, 1–6.

9 K. Kurita, *Prog. Polym. Sci.*, 2001, **26**, 1921–1971.

10 H. Sashiwa, Y. Makimura, R. Roy and Y. Shigemasa, *Chem. Commun.*, 2000, 909–910.

11 H. Sashiwa, N. Kawasaki, A. Nakayama, E. Muraki, H. Yajima, N. Yamamori, Y. Ichinose, J. Sunamoto and S. Aiba, *Carbohydr. Res.*, 2003, **338**, 557–561.

12 K. R. Holme and A. S. Perlin, *Carbohydr. Res.*, 1997, **302**, 7–12.

13 O. Vernaez, K. J. Neubert, R. Kopitzky and S. Kabasci, *Polymers (Basel).*, 2019, **11**, 1939–1940.

14 C. C. Lin and C. W. Lin, *Drug Deliv.*, 2009, **16**, 458–464.

15 F. R. de Abreu and S. P. Campana-Filho, *Polímeros*, 2005, **15**, 79–83.

Chapter 6: Primary, binary, and ternary hydrogel blends by the freeze-thaw method

6.1 Introduction

The use of hydrogel blends in wound dressing applications has been well reported[1]. Hydrogels are biocompatible, three dimensional, and hydrophilic polymer lattices which are capable of absorbing large amounts of biological fluids or water[1,2]. Biodegradability of these hydrogels may be facilitated through enzymatic, hydrolytic, or environmental pathways[1]. Due to their soft consistency and it's high water content, hydrogels simulate natural living tissue to the largest extent when compared to any other synthetic biometerials[3]. Hydrogels are preferred drug carrier systems because their porosity allows for the loading of drugs into the gel matrix[4]. When hydrogels are applied in the biomedical industry, one of the attractive properties that hydrogels may offer is the ability to either absorb or donate moisture to the wound environment[5]. This ensures a moist wound healing environment which leads to faster wound healing[6].

These hydrogel blends can be crosslinked by either chemical or physical methods to achieve structural integrity. Chemical crosslinking is reported to impart a range of adverse effects on the biocompatibility of the resulting hydrogels[7]. Any left-over crosslinker has to be removed before the hydrogels can be used in a biological environment and even after removal, trace amounts of the chemical crosslinker may still be present[7]. Crystallization through the freeze-thaw method is a facile technique for the production of physically crosslinked PVA hydrogels[8]. During the freeze-thaw method, crystalline regions are induced by phase separation[9] and this is attributed to molecular arrangements that serve as the junction points within the hydrogel structure[8]. Phases are separated into a PVA-rich phase and a water-rich phase during freezing[9]. When water is frozen, PVA is expelled and this leads to regions with a higher PVA concentration[2,9]. PVA chains are then in close contact with another where crystallite and hydrogen bonding occurs[9]. Upon thawing, these interactions remain intact, which results in a 3D hydrogel network[9]. Water, which acted as a porogen may then be removed by lyophilization. If the majority of the solvent does not undergo freezing, this heterogeneous gel will not form[7] and no phase separation will occur. If no phase separation occurs, then no pore formation will be observed, as phase separation is the main driving force behind pore formation[9].

PVA can be used in many applications such as biodegradable films, tissue engineering, drug delivery, and wound dressings to promote healing[10]. The blending of PVA with biopolymers

such as CTS and chitin proved to be very suitable for the production of biometerials[10]. The most important property of hydrogels is their biocompatibility[11], but their antimicrobial properties are also to be considered if these hydrogels will be used on areas that could be subject to bacterial infection. CTS has been widely used in the production of hydrogels for wound dressing purposes[11]. CTS possesses several attractive properties, including biocompatibility, low toxicity, immune-stimulatory effects, and antimicrobial activity has been reported[11,12]. As a result, chitosan exhibits favorable effects with regards to wound healing[13]. Some of the drawbacks of CTS include the fact that it is only soluble below a pH of 6[14–16], it often has poor mechanical performance and high production costs[10]. These drawbacks can, however, easily be overcome by using CTS in a blend with a synthetic polymer such as PVA. PVA also exhibits favorable properties and combining these polymers will lead to the combination of the advantageous properties of the polymers contained in the blend[10]. Solubility issues can be overcome by the derivatization of CTS, resulting in hydrophilic polymers[16]. Hydrogel blends with a derivative of chitosan, NOCC, which also exhibits many of the favorable properties of chitosan with additional properties such as its water solubility has been reported[16].

In this study, a series of hydrogel blends, consisting of a blend of PVA and CTS or NOCC were produced. These were reinforced with nanofillers in the form of ChNWs or CNWs. The hydrogel blends were all crosslinked utilizing a physical crosslinking method, known as the freeze-thaw method. The resulting primary, binary, and ternary hydrogel blends were then evaluated. Morphological analysis was facilitated by employing scanning electron microscopy (SEM). Thermal properties were investigated through thermogravimetric analysis (TGA) and differential scanning calorimetry (DSC). The distribution of the respective fillers throughout the matrices were visualized by employing confocal fluorescence microscopy (CFM). Rheological methods were used to probe the viscoelastic properties of these hydrogel blends and to confirm the successful hydrogel formation. Swelling studies were also performed to quantify the extent of water uptake in a neutral environment as a percentage. Finally, antimicrobial studies were performed to investigate the effects of changing the matrix and the addition of nanofillers to the primary hydrogel consisting of PVA.

6.2 Results and discussion

6.2.1 Rheology

Rheological characterization was carried out to obtain information about the viscoelastic properties of the various, crosslinked hydrogel blends by performing an amplitude and frequency sweep. To obtain a valid characterization, it is important that G’ and G” are

measured within the LVE region of the sample[17]. To do this an amplitude sweep was performed. The limit of the LVE region is defined where G' deviates by more than 5% according to the standards ISO 6721-10 and EN/DIN EN 14770. The amplitude sweep results can be seen in **Figure 6.1** - **Figure 6.3**.

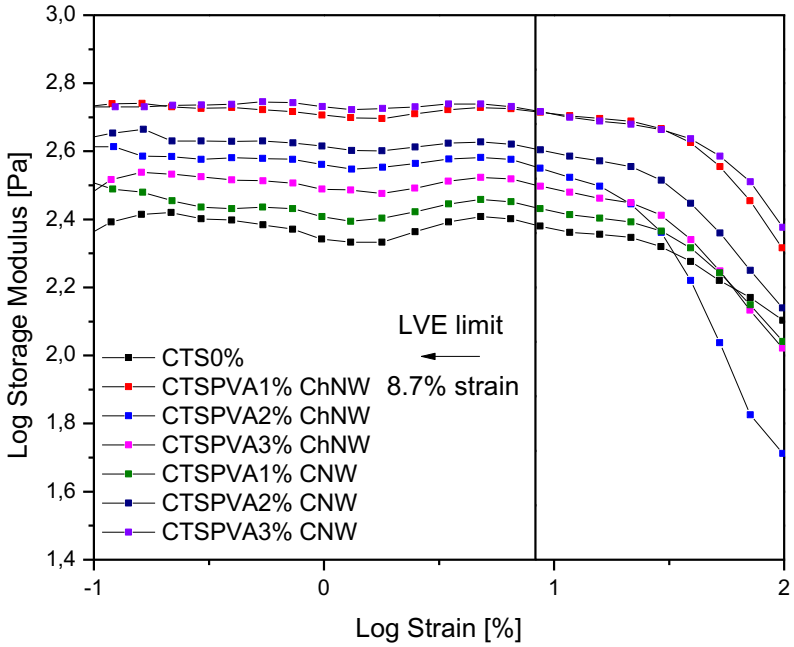

Figure 6.1: Determination of the LVE region for the CTSPVA sample with different loadings of ChNW and CNW filler.

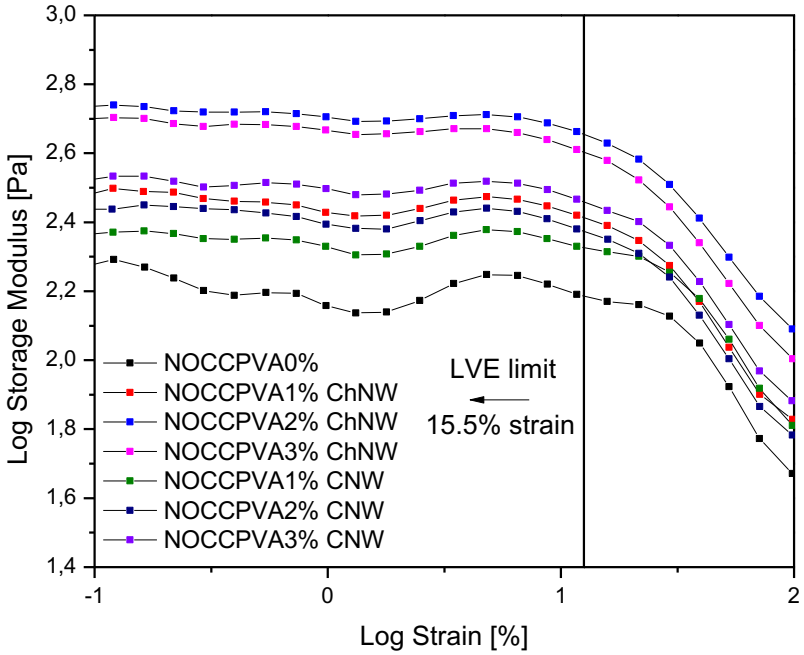

Figure 6.2: Determination of the LVE region for the NOCCPVA sample with different loadings of ChNW and CNW filler.

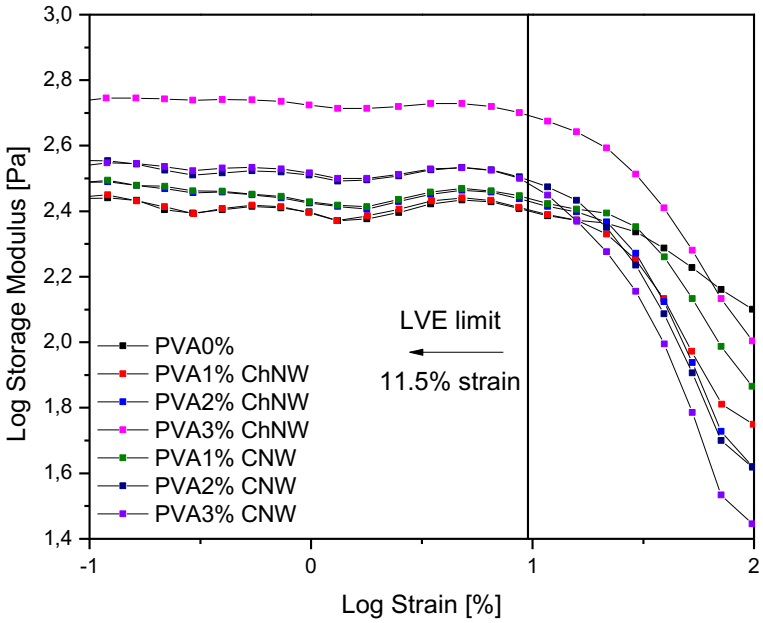

Figure 6.3: Determination of the LVE region for the PVA sample with different loadings of ChNW and CNW filler.

The end of the LVE region is identified by a remarkable decrease in G'. This is due to the destruction of the network and is called the Payne effect[18].

The Payne effect was observed for all samples, evaluated. When the strain percentage reached a certain value, a remarkable decrease in G' was observed. In the case of the hydrogel samples, it is due to the breakdown of the physical network, induced during crosslinking.

When looking at **Figure 6.1** - **Figure 6.3**, the vertical line indicates the first sample to reach the LVE limit. It became clear from **Figure 6.2** that the NOCCPVA series had the highest LVE limit when compared to the other two matrices. This means that the NOCCPVA matrix had the most stable crosslinked network, taking the effect of the fillers into account, as the breakdown of this network only started at a strain of 15.5%, as opposed to 8.7 and 11.5% for the CTSPVA and the PVA matrices, respectively.

The pure CTSPVA matrix reached the LVE limit at 38.9%. When comparing the effect of the ChNW and CNW filler loadings on the different matrices it was observed that the addition of 1% of the ChNW filler to the CTSPVA matrix, shown in **Figure 6.1**, increased the LVE limit to 52.5% strain due to the enhancement of the physical crosslink network. However, ChNW loadings of 2 and 3%, respectively, resulted in a decrease of the LVE limit as it was reached

at 15.4 and 8.7%, respectively. Upon the addition of the CNW filler to the CTSPVA matrix, a decreased in the LVE limit was observed when comparing it to the pure CTSPVA matrix. CNW filler loadings of 1, 2, and 3% resulted in the LVE limit being reached at strains of 21.4, 29.3, and 8.8%, respectively. From this, it is clear that the addition of the CNW filler into the CTSPVA matrix had adverse effects on physical network formation during crosslinking.

The limit of the LVE region for the pure NOCCPVA matrix was reached at a strain percentage of 15.5%. This can be seen when looking at **Figure 6.2**. Upon addition of the ChNW filler, loadings of 1, 2, and 3% all increased the LVE limit to 21.4% thus having a stabilizing effect on the matrix. The addition of the CNW loadings of 1, 2, and 3% resulted in an increase of the LVE limit to 28.8, 21.5, and 21.6%, respectively. Here we can see that the addition of both the ChNW and the CNW filler resulted in increased network stability.

When looking at **Figure 6.3**, the pure PVA matrix reached the LVE limit at a strain percentage of 38.9%. Upon evaluation of the LVE limits with the addition of the ChNW filler, it was observed that the addition of 1, 2, and 3%, respectively, resulted in the decrease of the LVE limit to 28.4, 21.4, and 11.69%, respectively. After the addition of the CNW filler in loadings of 1, 2, and 3%, the LVE limit decreased to 29.3, 21.6, and 16.0%, respectively.

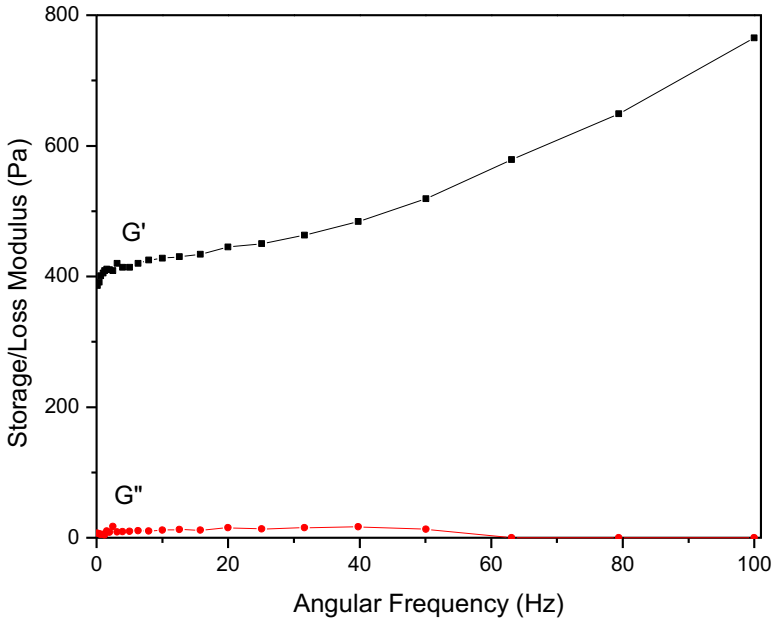

Figure 6.4: The storage (G') and loss modulus (G") of the pure CTSPVA matrix.

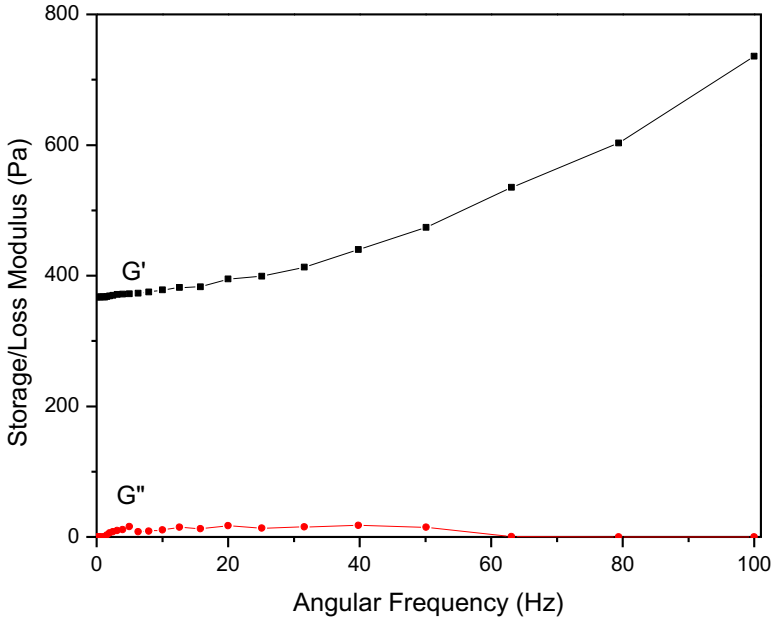

Figure 6.5: The storage (G') and loss (G") modulus of the pure PVA matrix.

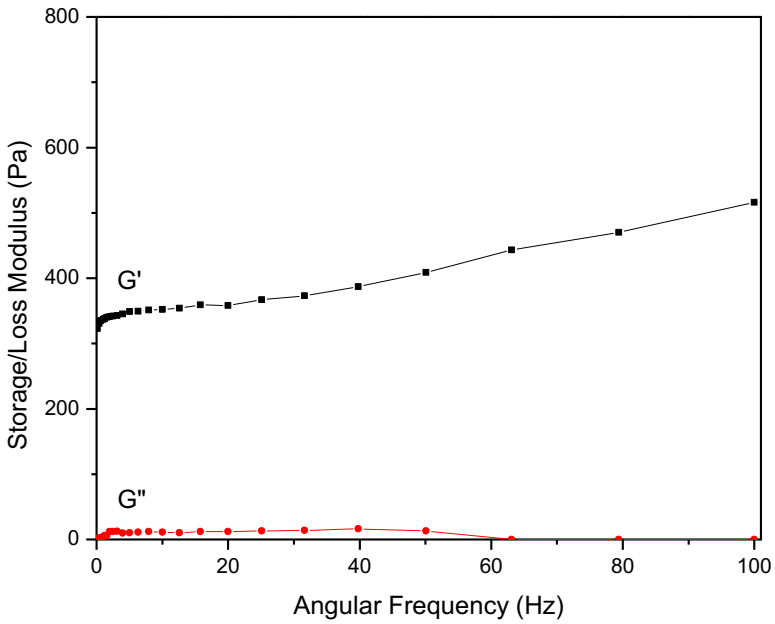

Figure 6.6: The storage (G') and loss (G") modulus of the pure NOCCPVA matrix.

Frequency sweep experiments were performed at a constant stress of 1%. This percentage was chosen to ensure that no degradation of the respective samples takes place. Using the

data from the frequency sweep study, **Figure 6.4** - **Figure 6.6** was produced. From these plots, it is clear that G' is much larger than G" thus, samples exhibit gel-like behavior, proving successful hydrogel formation for all the pure matrices.

Furthermore, the LVE limit for the CTSPVA and the PVA matrices were the highest. This corresponds to the higher G' measured for the CTSPVA and the PVA matrices as seen in **Figure 6.4** and **Figure 6.5**. The increased G' compared to the NOCCPVA matrix in **Figure 6.6** is also indicative of a higher extent of crosslinking with more energy being stored elastically.

6.2.2 Swelling studies

The swelling behavior of the various hydrogel blends was evaluated to investigate the effect of the respective fillers used as well as the difference in polymers used in the various matrices. The results are graphically illustrated in **Figure 6.7** - **Figure 6.9**. When looking at these figures it is clear that all the matrices that contained the CNW filler had the largest weight gain (%) when swelled in neutral water (pH 7). This can be explained by looking at the functional groups present on the respective nanofillers. The ChNW filler contains hydroxyl and acetyl functional groups whilst the CNW filler contains only hydroxyl groups[19]. The hydrophilicity of the hydroxyl group is facilitated by the hydroxyl group acting as hydrogen-bond donors to water[20]. Cellulose, constituting of glucose units contain ample hydroxyl groups so good interaction with water is expected[20]. ChNWs also contain hydroxyl functional groups which should facilitate some interaction with water. Due to the presence of the acetyl group, some hydrophobicity is imparted and this also results in chitin being insoluble in aqueous media[21,22]. It is due to the hydrophobic acetyl group present in the ChNW filler that the swelling in water is less for the matrices containing ChNWs. No trends were observed concerning filler content.

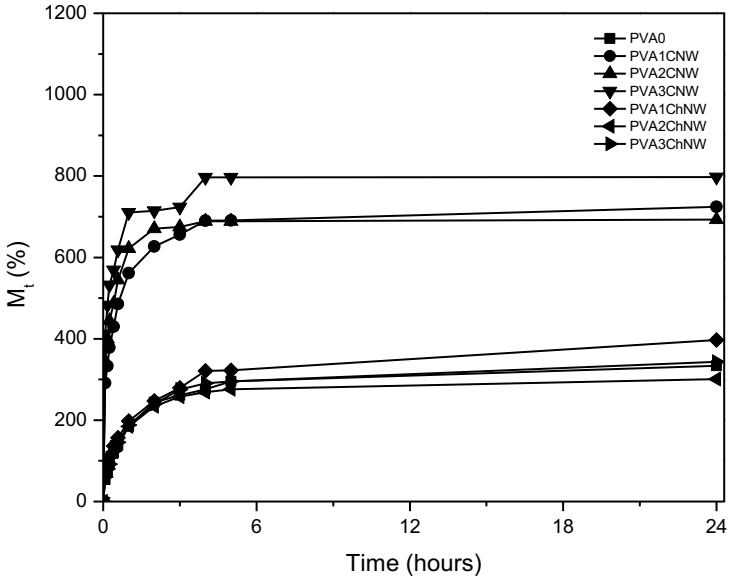

Figure 6.7: The swelling behavior of the PVA matrix, containing different loadings of CNW and ChNW nanofiller as a function of time.

When comparing the effect that different matrix compositions had on the swelling behavior of these hydrogels it can be seen in **Figure 6.7** that the PVA matrix had the least weight gain as a function of time. This could be attributed to the ability of the PVA chains to pack closer in the absence of CTS and NOCC as it was previously found that CTS hindered spherulite formation[23]. A study on films that used similar blends with PVA and NOCC also concluded that the addition of PVA to the matrices reduced equilibrium water uptake[24].

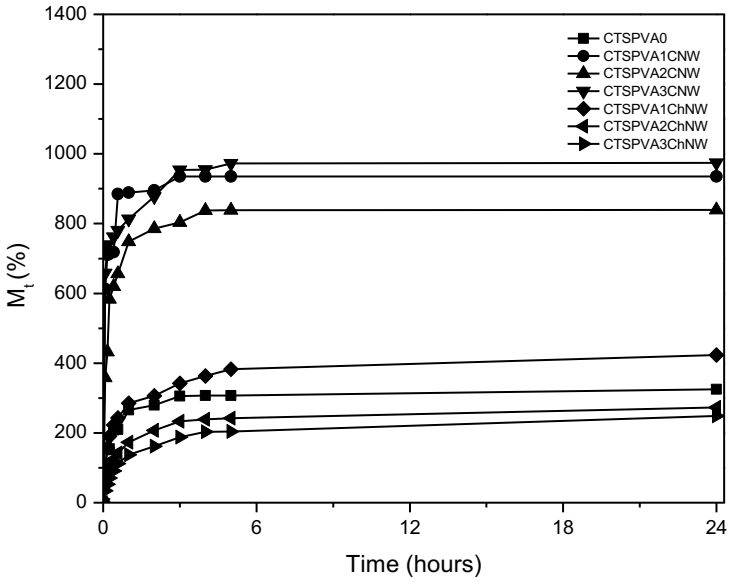

Figure 6.8: The swelling behavior of the CTSPVA matrix, containing different loadings of CNW and ChNW nanofiller as a function of time.

In **Figure 6.8** it is observed that the addition of CTS to the PVA matrix resulted in an increased equilibrium percentage weight gain compared to the pure PVA matrix in **Figure 6.7**. CTS contains acetyl functional groups[19] which imparts hydrophobicity[21,22] so it is expected that the addition of this polymer will result in lower equilibrium swelling when compared to a more hydrophilic polymer such as NOCC. CTS also perturbs the formation of PVA crystallites and a reduction in crystallinity could cause more water molecules to penetrate the polymer network[23].

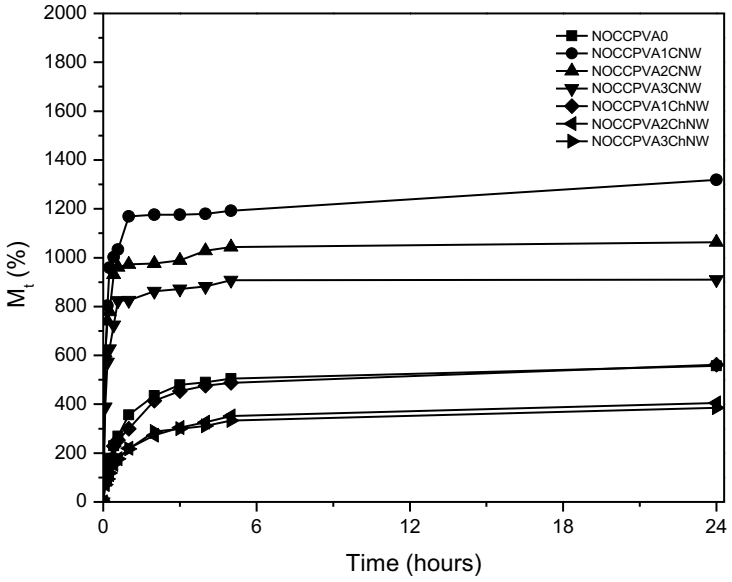

Figure 6.9: The swelling behavior of the NOCCPVA matrix, containing different loadings of CNW and ChNW nanofiller as a function of time.

The greatest weight gain was observed upon evaluation of the NOCCPVA matrix in **Figure 6.9**. CTS that underwent carboxymethylation contains carboxyl groups at the O-position and the N-position in the glucosamine and N-acetylglucosamine units of CTS, resulting in NOCC. Carboxyl groups have a pKa value of ca. 4.5[25], thus it is expected that all carboxylic groups will be deprotonated at pH 7 at which swelling tests were conducted. The deprotonated carboxylic acid groups will facilitate more interaction with water because COO^- is more polar than COOH and greater dipole-dipole interactions will be possible. This resulted in higher water absorption compared to pure PVA and the CTSPVA matrix.

6.2.3 Antimicrobial studies

The antimicrobial activity of the various samples was evaluated against the gram-positive *Staphylococcus aureus* which is a very common skin pathogen. The reported technique is well

reported in literature[26–28]. It is a visual technique that is widely used as a determinant of positive and negative antimicrobial activity. A blue color indicates antimicrobial activity or no microbial growth (no reduction of the dye by living organisms) while a pink/purple colour indicates the presence of bacteria (metabolic activity detection), therefore no antimicrobial activity.

Figure 6.10 shows the samples after a few hours at room temperature. When looking at the different matrices, it is observed that the samples labeled “Matrix” in the petri dishes are all blue (the dye has not been reduced by living organisms) – this is an indication of no microbial growth. This means that microbial growth was inhibited over a few hours. The same observation could be made for all the loadings of ChNW (1 – 3%) in all the matrices (PVA, CTSPVA, and NOCCPVA). When evaluating the CNW filler in the PVA and PVANOCC matrix (samples labeled 1%CNW, 2%CNW, and 3%CNW) the reduced form of the dye (pink/purple) was observed in all samples. This indicates microbial metabolic activity. However, when evaluating the CTSPVA matrix no microbial activity was observed. From this, we can conclude that the presence of CTS caused the hydrogel blend to act as a better inhibitor of microbial activity than NOCC and PVA whilst CNW may be used as a food source for *S. aureus.* This was a good indication of the short-term behavior of the different matrices with the respective fillers. The evaluation of longer-term antimicrobial activity follows below.

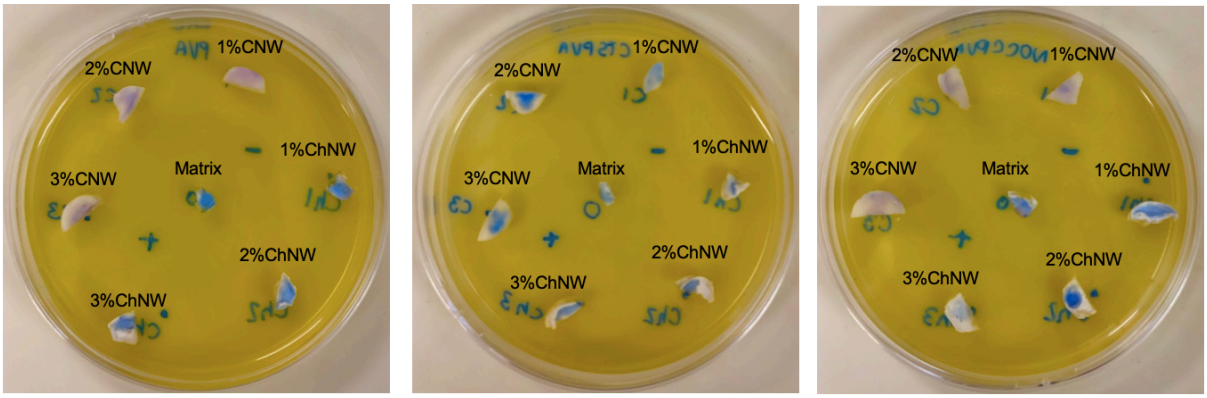

Figure 6.10: Preliminary results after a few hours at room temperature, stained with alamarBlue. Left -the PVA matrix, Middle – the CTSPVA matrix, and Right – the NOCCPVA matrix. Fillers and loadings are indicated

For the evaluation of the behavior of these matrices over a longer period all samples were exposed to *S. aureus* and incubated to create an ideal environment for bacterial growth. These samples were then evaluated after 60 hours of incubation at 37 ºC and stained with NBC to visualize microbial growth.

For **Figure 6.11** similar results are observed as above. When evaluating the CNW filler, all the loadings (1 – 3%) facilitated microbial growth (microbial growth appears purple) in all the matrices (PVA, CTSPVA, and NOCCPVA). When looking at the ChNW filler it is clear that this filler revealed an inhibiting effect on microbial growth. (Where less purple areas were observed it means that much less microbial growth took place).

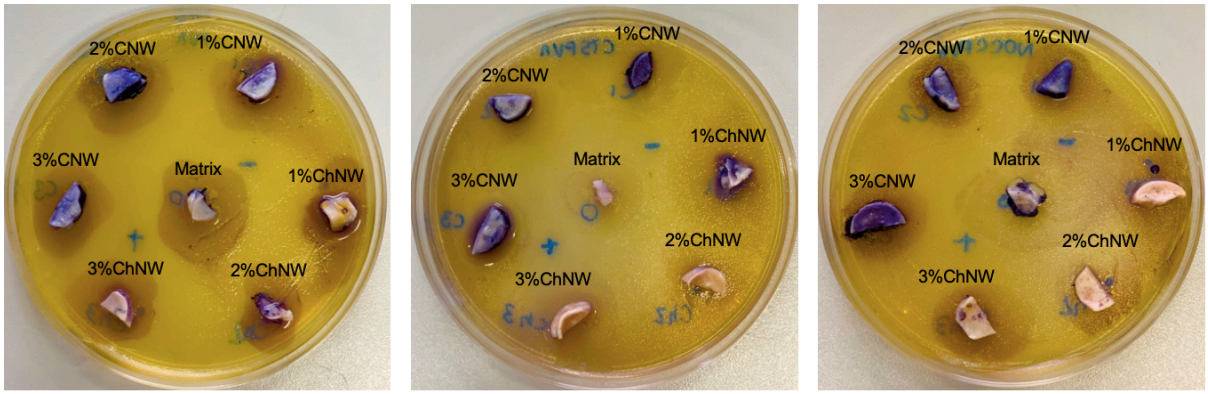

Figure 6.11: Results after 60 hours of incubation, stained with NBC. Left -the PVA matrix, Middle – the CTSPVA matrix, and Right – the NOCCPVA matrix. Fillers and loadings are indicated

6.2.4 Confocal fluorescence microscopy (CFM)

Ternary hydrogel blends containing ChNW and CNW were analyzed by confocal fluorescence microscopy to visualize nanofiller distribution throughout the respective matrices. The Z – stack images were used to visualize the spatial orientation of the fluorescent signals. **Figure 6.12** - **Figure 6.14** shows the respective filler distribution in the different matrices at a nanofiller loading of 2%. Overall, when comparing all the images below, the ChNW filler seemed to show more agglomeration presumably due to the strong intermolecular interaction due to the presence of hydroxyl and acetyl groups[19] which could indicate stronger intermolecular forces between ChNWs and CNWs respectively[6]. The ChNW filler showed the most agglomeration in the PVA matrix (**Figure 6.12** left) followed by the CTSPVA matrix (**Figure 6.13** left). This could be due to the increased interfacial adhesion between ChNWs and CTS which has been reported[23]. An increase in interaction between the filler and the matrix increase the degree of dispersion of nano fillers[29,30]. The NOCCPVA matrix (**Figure 6.14** left) exhibited the least aggregation which indicated good compatibility between ChNWs and the NOCCPVA matrix. Areas with higher filler concentration appear bright green whilst areas where the filler is more dispersed appear as dispersed green dots. Cyan and magenta lines in the figures below represent folds. Folding in these sides will result in a box shape so that one can acquire a 3D image. The grey squares in the top right corner of each image would thus be eliminated when the sides are folded in. The green and red lines represent the x- and y-coordinates whilst the

blue line shows the z-coordinate. These coordinates can be manipulated during image processing by ZEISS ZEN microscope software to compare the spatial orientation of fluorescent signals. Even though agglomeration was observed, the nanofiller was distributed throughout the matrices[69].

When looking at the CNW nanofiller (**Figure 6.12** right - **Figure 6.14** right) it seemed to be equally compatible with all three matrices and dispersed throughout the samples.

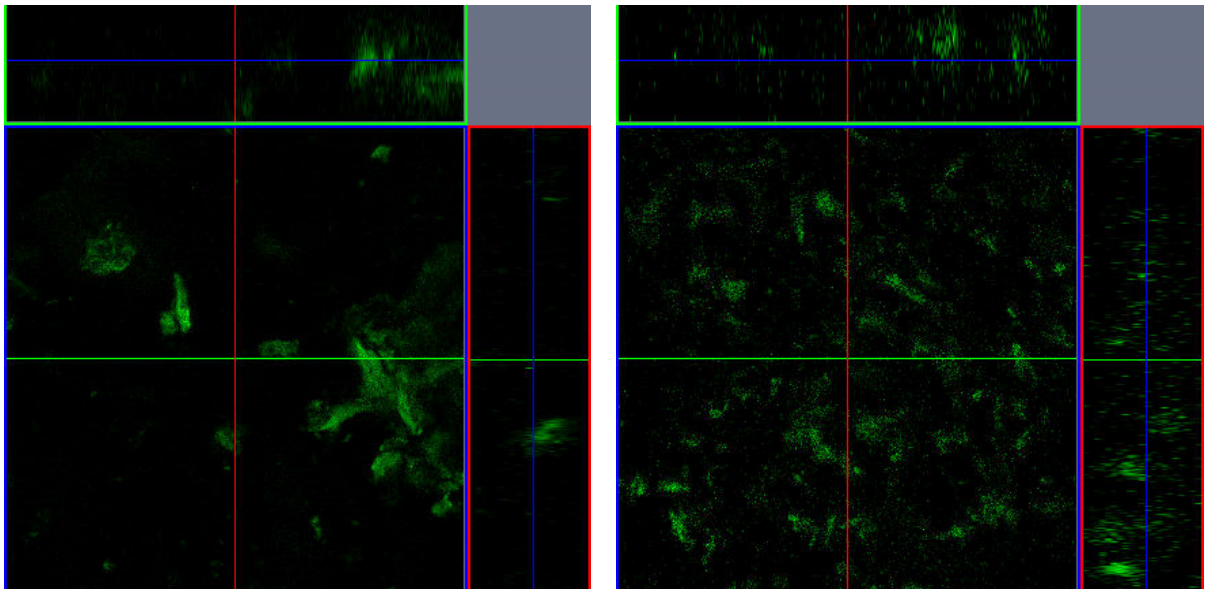

Figure 6.12: Left – the fluorescently labeled PVA2%ChNW sample. Right – the fluorescently labeled PVA2%CNW sample.

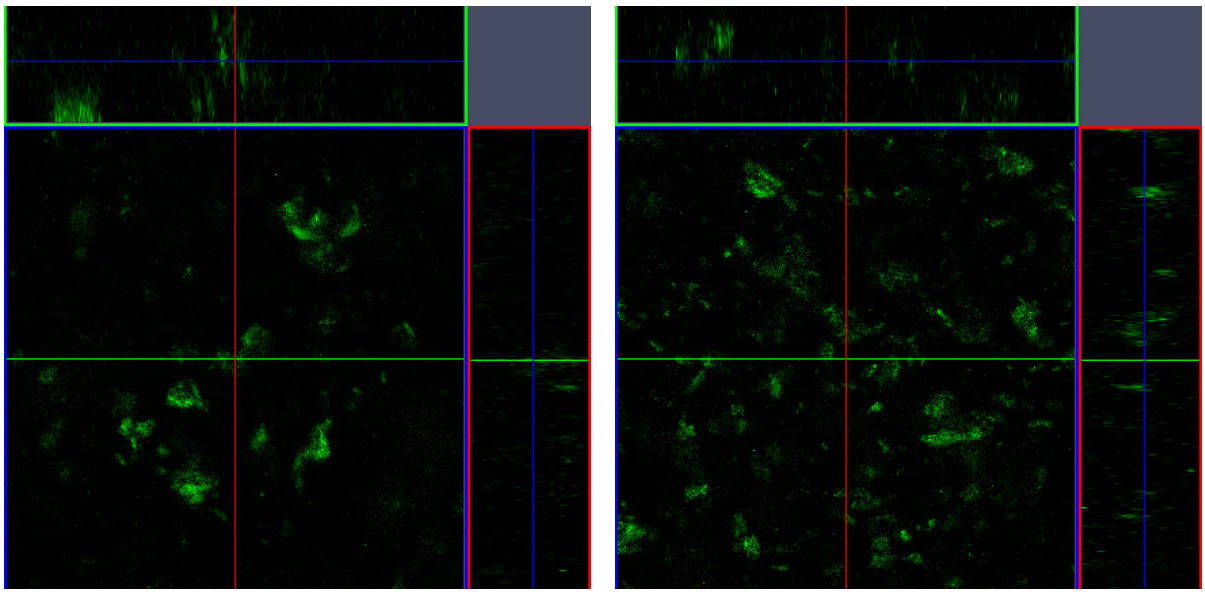

Figure 6.13: Left – the fluorescently labeled CTSPVA2%ChNW sample. Right - the fluorescently labeled CTSPVA2%CNW sample.

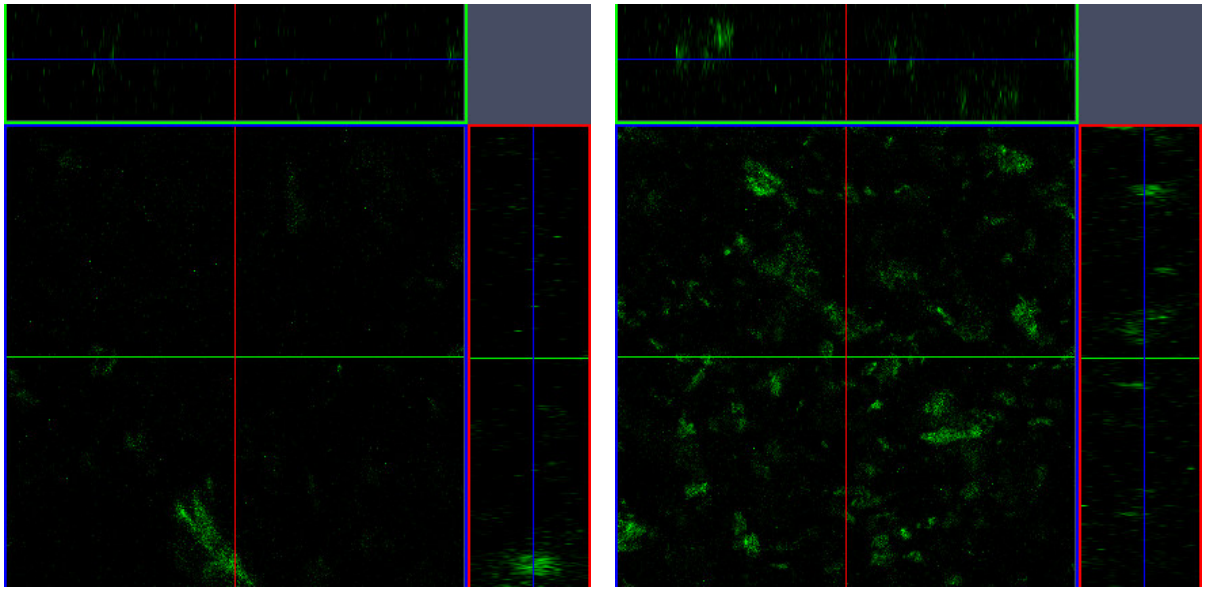

Figure 6.14: Left - the fluorescently labeled NOCCPVA2%ChNW sample. Right – the fluorescently labeled NOCCPVA2%CNW sample.

To further visualize the distribution of the samples, a gallery of filler distribution images at different depths was compiled and is shown in **Figure 6.15** to **Figure 6.20**. The first 51.9 µm of the matrices were probed and compared. Analysis at a deeper level was not performed because out of focus images were produced when the samples were scanned at a deeper level which resulted in weaker signals until they finally disappeared.

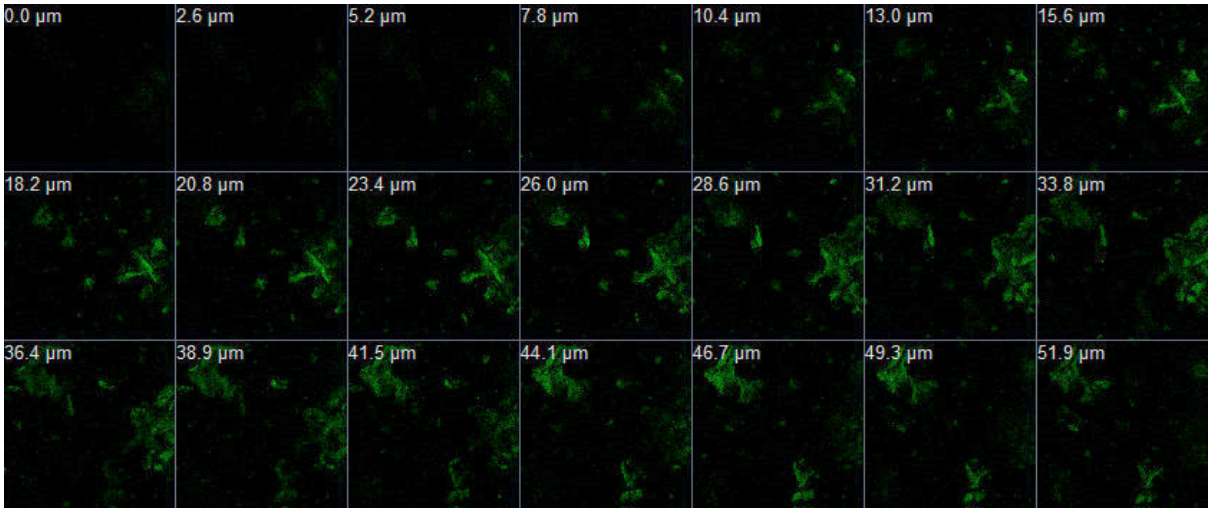

Figure 6.15: Gallery of fluorescent signals at different depths of the PVA2%ChNW sample.

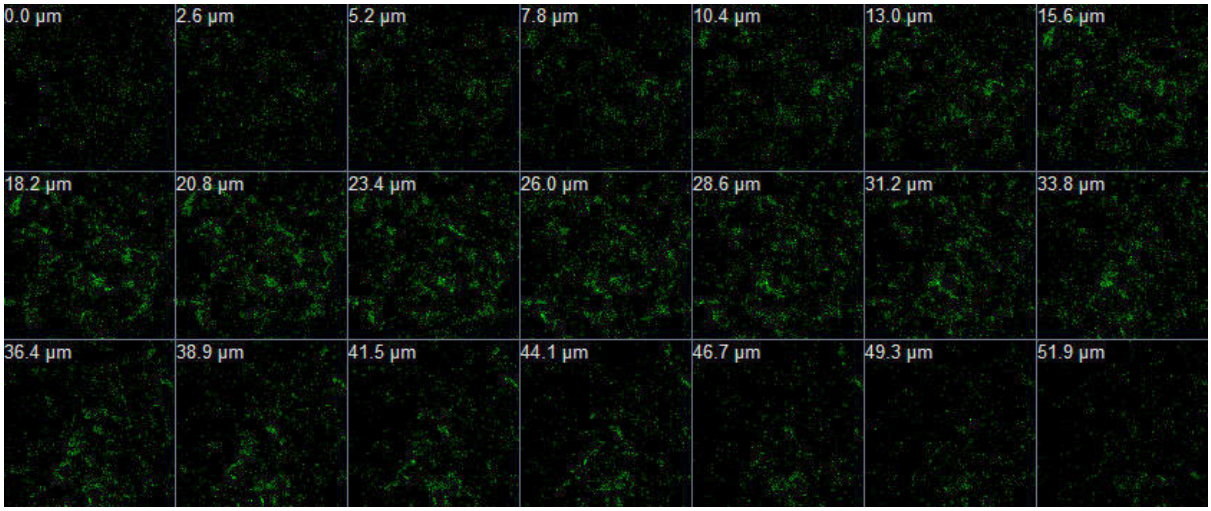

Figure 6.16: Gallery of fluorescent signals at different depths of the PVA2%CNW sample.

Figure 6.15 and **Figure 6.16** show the nanofiller distribution of the PVA matrix with the ChNW and CNW nanofiller, respectively. Very weak fluorescent signals were observed at 0.0 µm, which will be the surface of the sample. As the sample was scanned in progressively deeper levels the fluorescent signal increased in intensity before starting to decrease at about 36.4 µm for both the ChNW and the CNW nanofiller. This is a clear indication that both the ChNW and CNW filler is distributed throughout the matrices as opposed to concentrated on the surface of the sample. **Figure 6.15** shows more agglomeration of the ChNW filler whilst **Figure 6.16** shows that the CNW nanofiller is more dispersed throughout the PVA matrix.

Figure 6.17 and **Figure 6.18** show the nanofiller distribution in the CTSPVA matrix. As seen in the PVA matrix, weak fluorescent signals were observed at 0.0 µm for both the ChNW and CNW filler, which means that the fillers were not predominantly observed at the surface. As the sample was investigated at deeper levels, fluorescent signals also became more prominent where after signals diminished as a depth of 51.9 µm was approached and signals became more distorted due to difficulty in producing images that were in focus. This is, however, a good indication that both the ChNW and CNW fillers were distributed throughout the matrix.

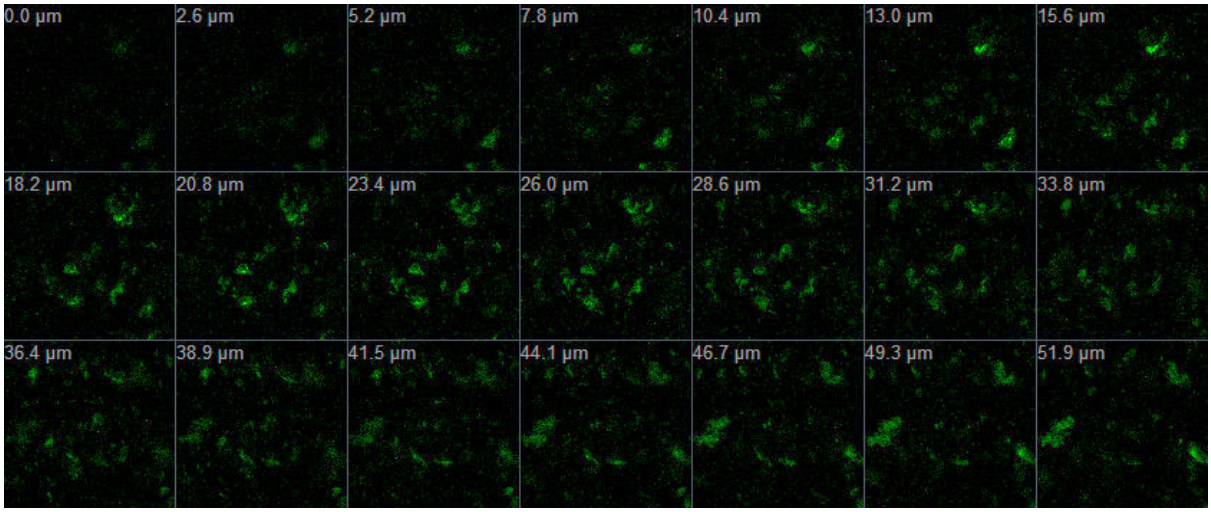

Figure 6.17: Gallery of fluorescent signals at different depths of the CTSPVA2%ChNW sample.

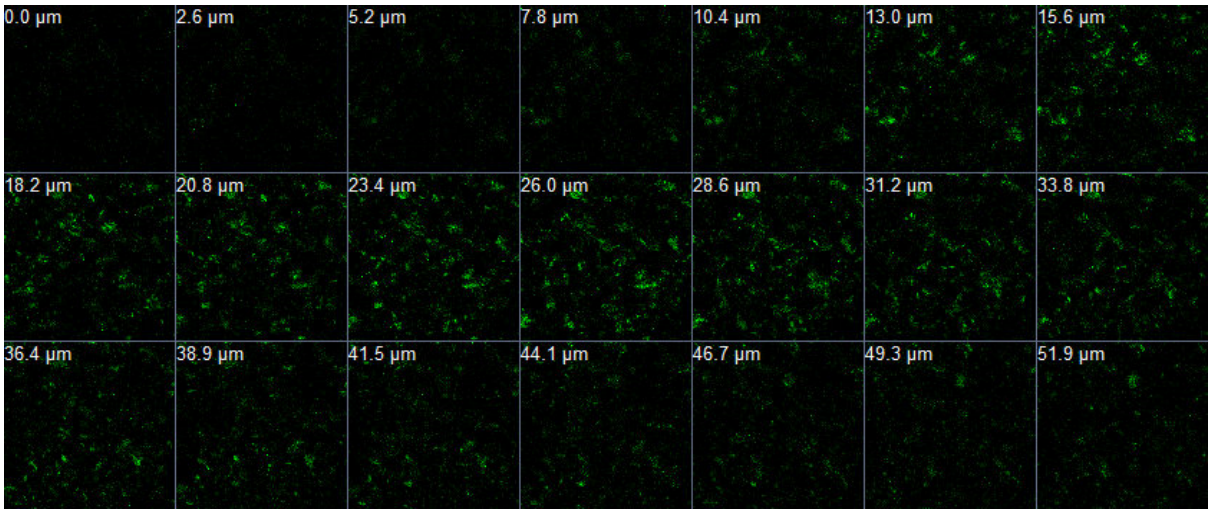

Figure 6.18: Gallery of fluorescent signals at different depths of the CTSPVA2%CNW sample.

Figure 6.19 and **Figure 6.20** show a gallery of the distribution of ChNW and CNW in the NOCCPVA matrix, respectively. In these figures, it is clear that as the sample is probed at deeper and deeper levels the fluorescent signals became stronger until the signals started to diminish due to the distortion of out-of-focus images. This is a good indication that both the ChNW and CNW nanofillers are evenly distributed throughout the sample and does not occur on the surface. These observations are supplemented by results from **Figure 6.12** to **Figure 6.14**.

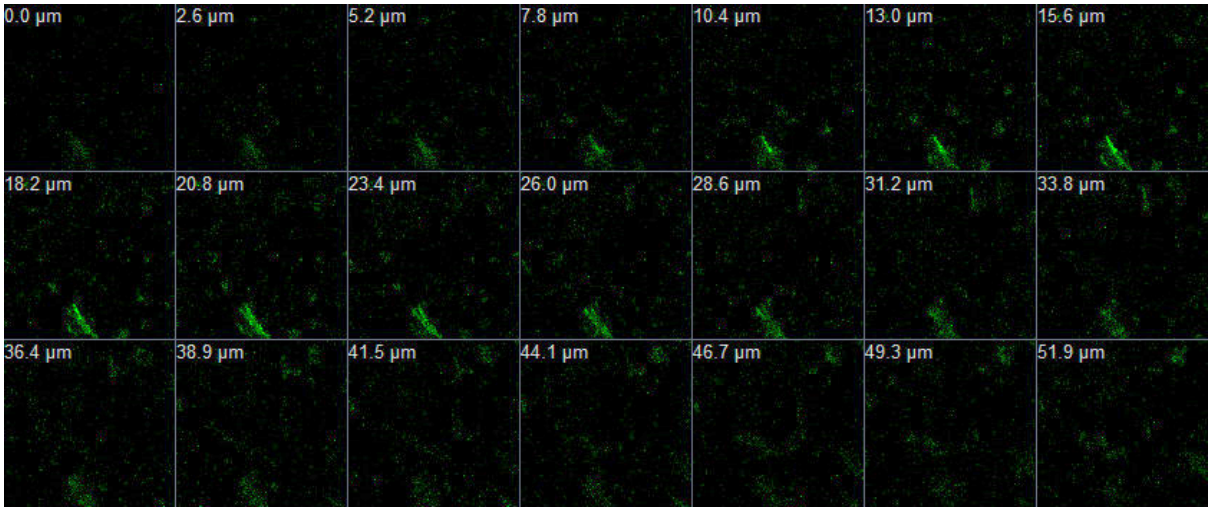

Figure 6.19: Gallery of fluorescent signals at different depths of the NOCCPVA2%ChNW sample.

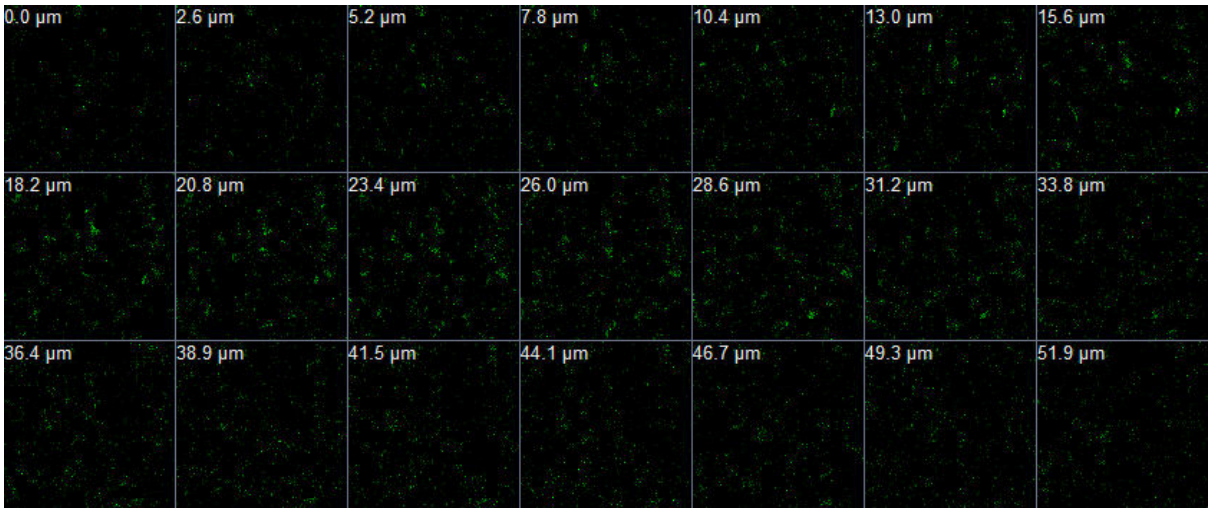

Figure 6.20: Gallery of fluorescent signals at different depths of the NOCCPVA2%CNW sample.

6.2.5 Scanning Electron Microscopy

Scanning electron micrographs of the primary, binary, and ternary hydrogel blends are shown below (**Figure 6.22** - **Figure 6.25**). SEM was performed to visualize the morphology of these hydrogel blends and to evaluate the effects, that blending of these polymers and the addition of nanofillers to the matrices might have had on the pore size and pore size distribution. During the freeze-thaw method, water served as porogen. After crosslinking, water may be removed by lyophilization and the pores will be created[31], with pore stabilization provided by the crystalline walls[2]. An example of a ternary hydrogel blend, including a typical pore and its measurement can be seen in **Figure 6.21**.

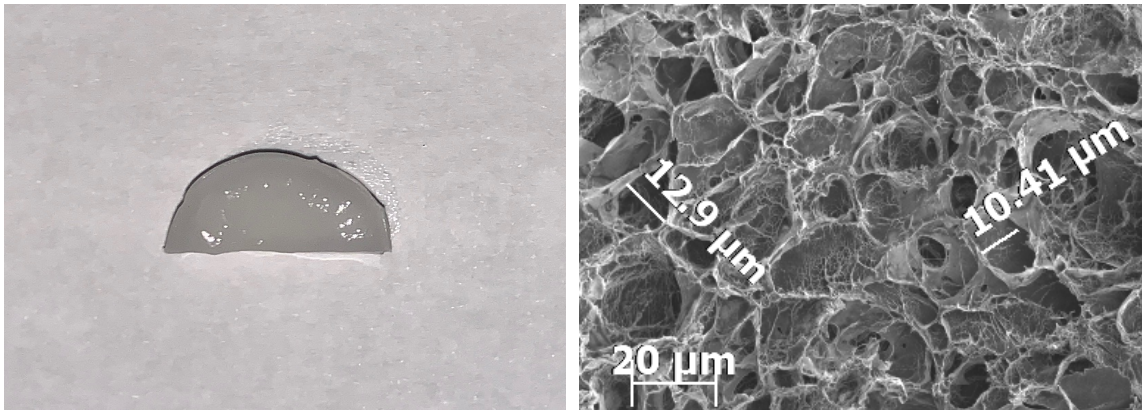

Figure 6.21: Left – The wet CTSPVA1ChNW sample. Right – SEM micrograph of the lyophilized CTSPVA1ChNW sample.

Upon evaluation of the pore size, it is clear from **Figure 6.26** and **Figure 6.27** that all the matrices and the nanofillers that were evaluated had average pore size measurements with large standard deviations. This could be a result of the fact that we do see some agglomeration upon analysis with CFM, as discussed and confirmed by CFM imaged in Section 6.2.4. Agglomeration in polysaccharide nanowhiskers such as ChNWs and CNWs can be easily explained when looking at their molecular structures in Section 2.4 and Section 2.6. The presence of ample hydroxyl groups in CNW and hydroxyl and acetyl groups in ChNW units facilitates interaction between the nanofiller and the polymer matrix but also results in strong hydrogen bonding between respective ChNW and CNW units which could cause agglomeration[19]. Generally, uniform particle or nanofiller dispersion is preferred as this will maximize the interaction of the nanofiller with the polymer[30]. Non-uniform nanofiller dispersion is often observed as a result of the strong interaction between individual nanoparticles or nanowhiskers and it is very difficult to redisperse these nanofillers after drying[32].

In a recent study[33], it was reported that the size, shape, and weight percentage of the nanofiller had a noteworthy effect on the crystallization kinetics and the final crystallinity of the matrix. It was also found that for the same particle size, an increase in the filler weight percentage resulted in a decrease in crystal growth rate and consequently a decrease in final crystallinity. This phenomenon is confinement related and the combined effects of particle size and weight percentage are captured by interparticle space[33]. A significant reduction in crystallinity will result when this free space between particles is smaller than the extended length of the molecule or the specific size of the crystal lamella thickness[33]. Thus, in this confinement limit, the final crystallinity and the crystal growth rate is controlled by the interparticle free space. It has been reported that there exists a greater tendency for aggregation during the preparation of nano-composites which may lead to secondary particles[34]. Many aggregates of

polysaccharide nanowhiskers will simply result in secondary particles - micron fillers[35]. This will reduce the interparticle free space and will impair crystallization in the matrix to a large extent. In a study by Holloway *et al.*[9], it is reported that the crystallinity increased with increased freeze-thaw cycles and that is proportional to an increase in pore size. A preliminary conclusion can be made that pore size is linked to crystallinity and that crystallinity is in turn dependent on the number of freeze-thaw cycles and filler content, according to literature[9,33].

When evaluating the effect of the ChNW nanofiller on the respective matrices as seen in **Figure 6.26** it seems that the incorporation of increasing loadings of ChNW filler caused a decrease in pore size in all the matrices as observed in literature[33] but the difference between these measurements is not statistically significant as illustrated by **Figure 6.26**, this is also difficult to see when looking at the SEM images. Although Jabbarzadeh *et al.*[33] found that crystallinity increased with an increase in weight percentage of nanofiller in the matrix, other studies provided contradicting evidence which means that it very much depends on the interaction of the specific nanofiller with the matrix. A study conducted by Bosq *et al.*[36] showed enhanced crystallization with the addition of nanofillers whilst other studies showed reduced crystallization[33] and some, no effect at all[37].

The effect that rod-shaped particles (CNWs) had on the crystallinity of polymer composites were evaluated by Zhou *et al*.[38]. The authors reported that the incorporation of CNWs accelerated gel formation and enhanced the formation of effective crosslinks[38]. When evaluating the effect of the CNW nanofiller on the respective matrices as seen in **Figure 6.27** it seems that the incorporation of increasing loadings of CNW filler caused an increase in average pore size in all the matrices, but these measurements are not statistically different when looking at the standard error bars in **Figure 6.27**.

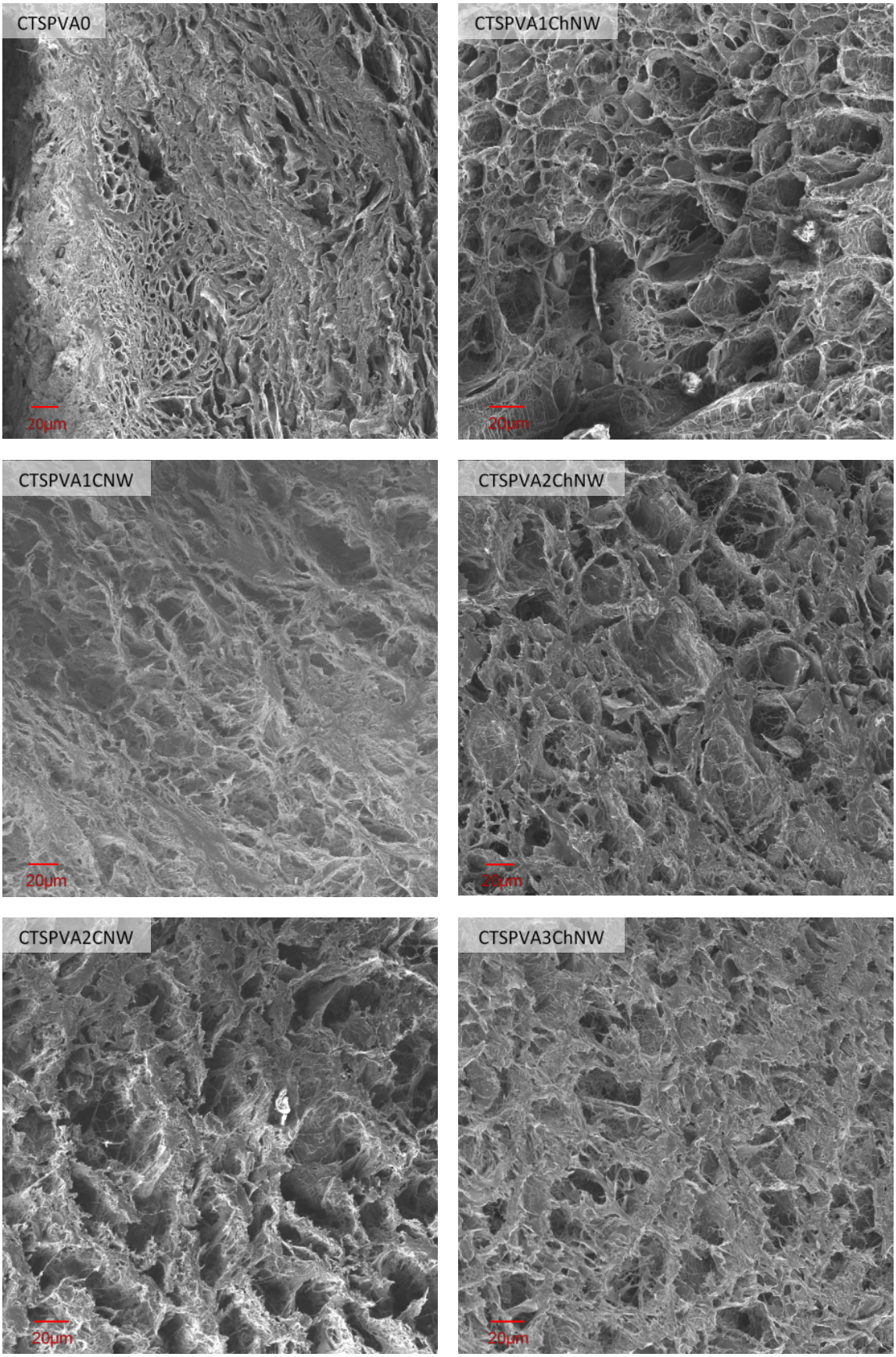

Figure 6.22: SEM micrographs of various matrices (labels on image).

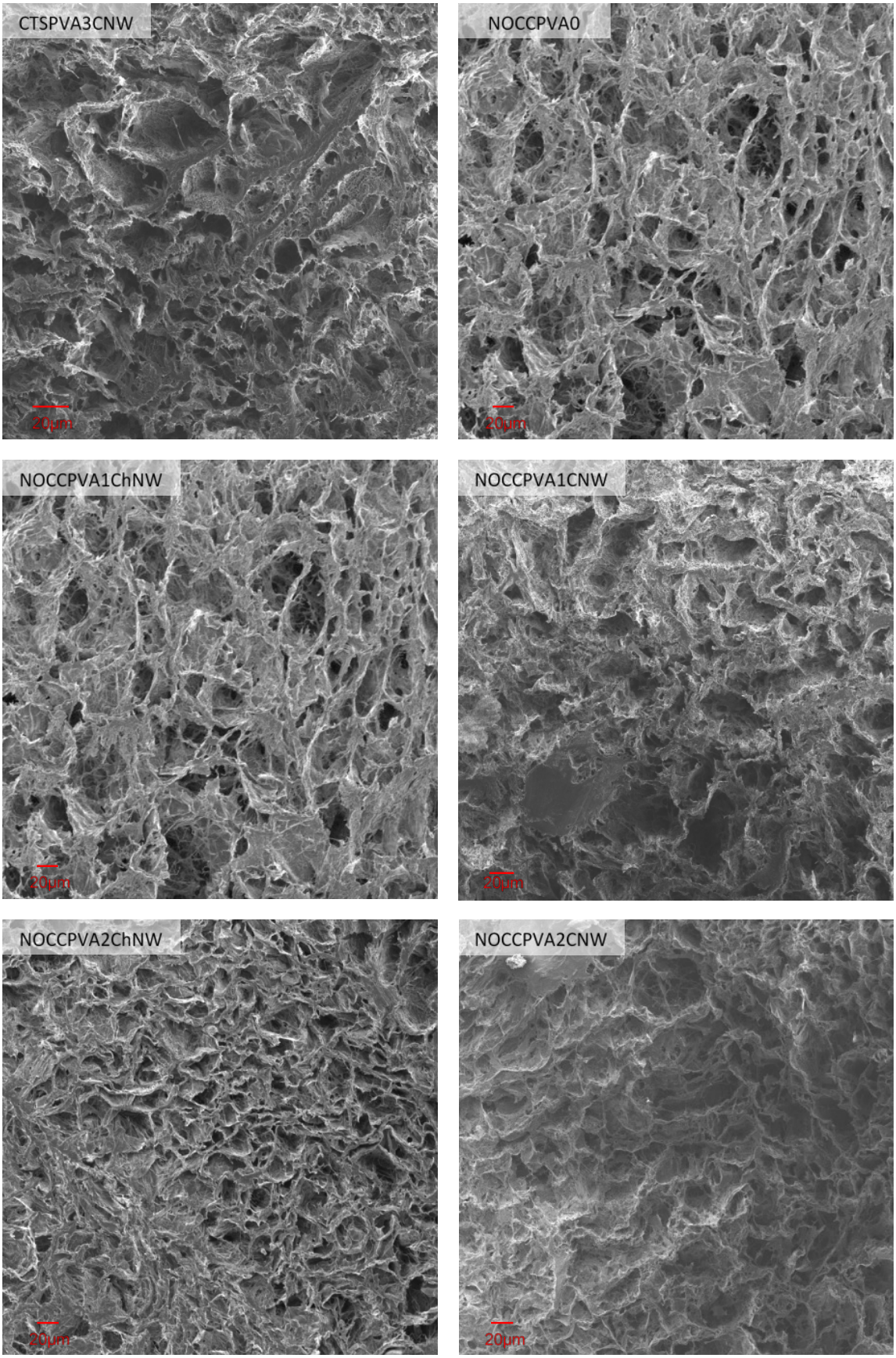

Figure 6.23: SEM micrographs of various matrices (labels on image).

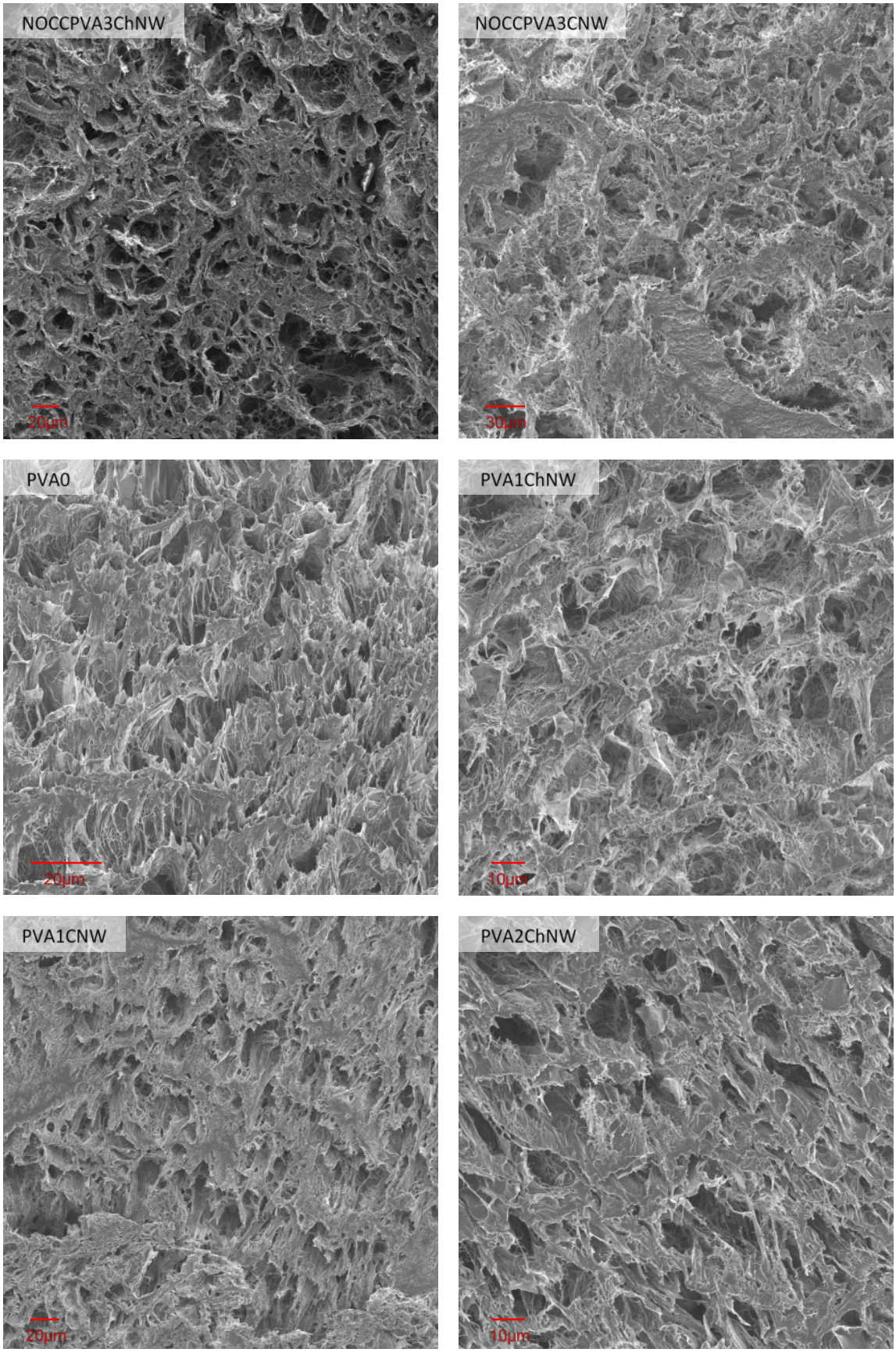

Figure 6.24: SEM micrographs of various matrices (labels on image).

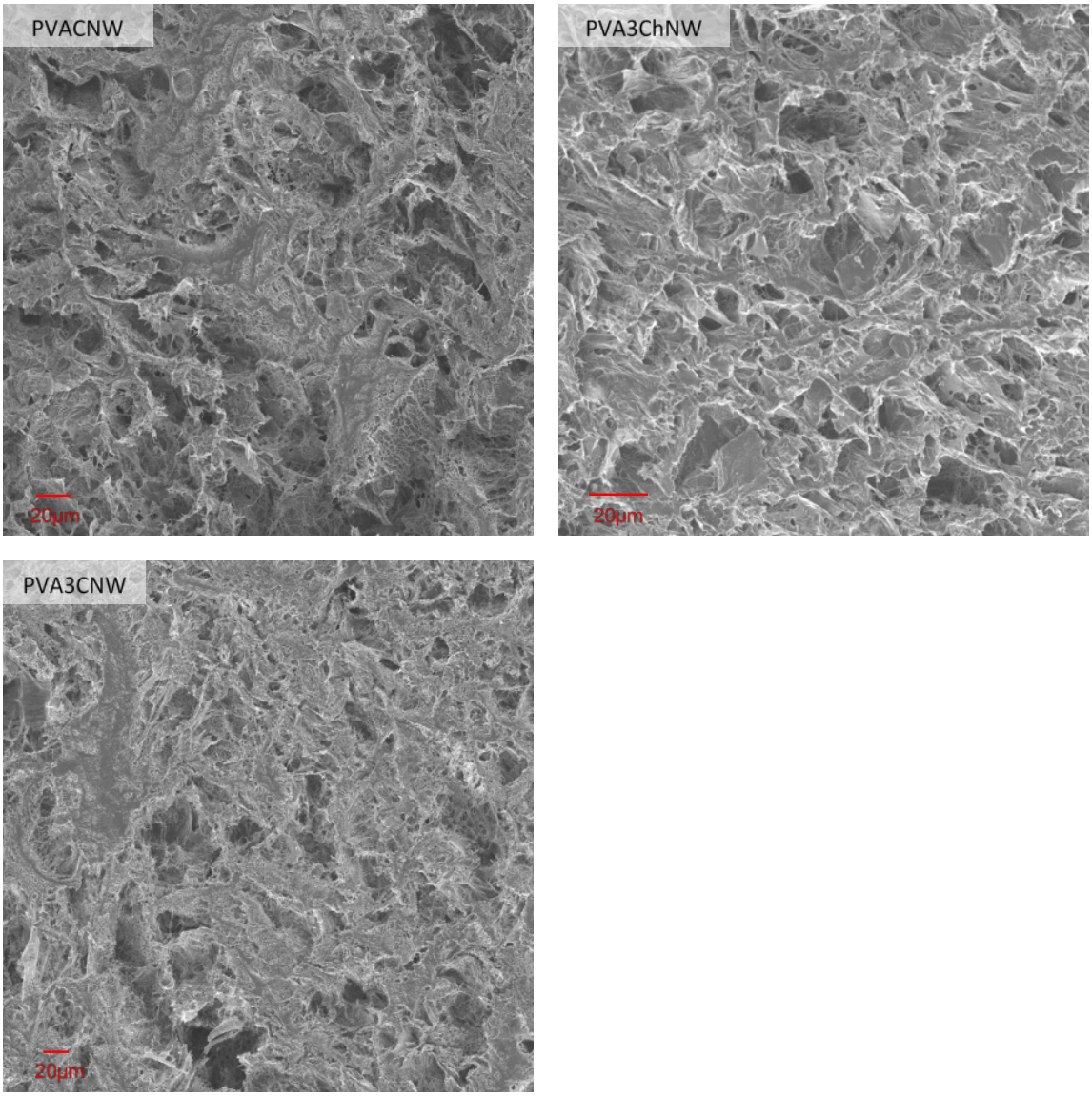

Figure 6.25: SEM micrographs of various matrices (labels on image).

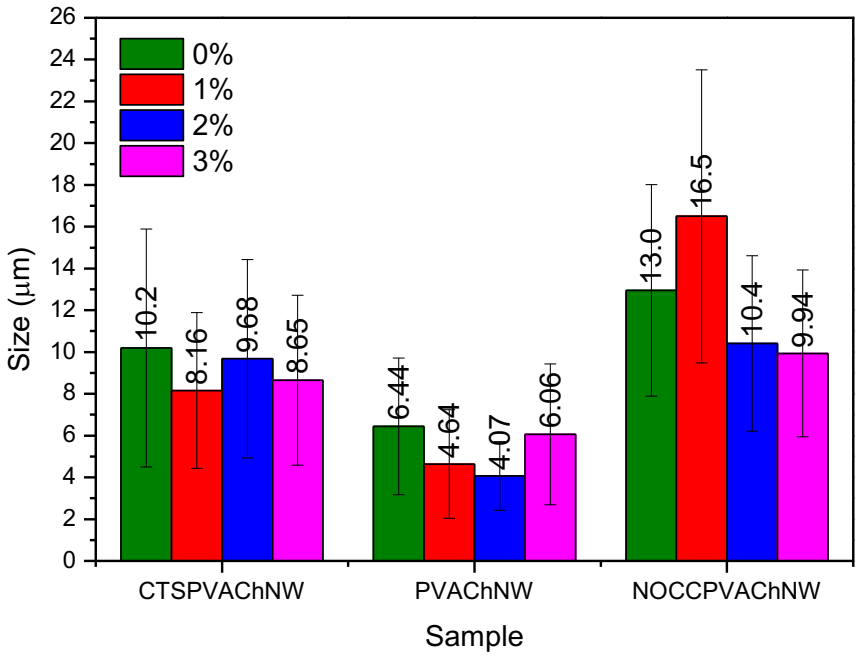

Figure 6.26: Overview of pore sizes of different matrices and different ChNW filler loadings.

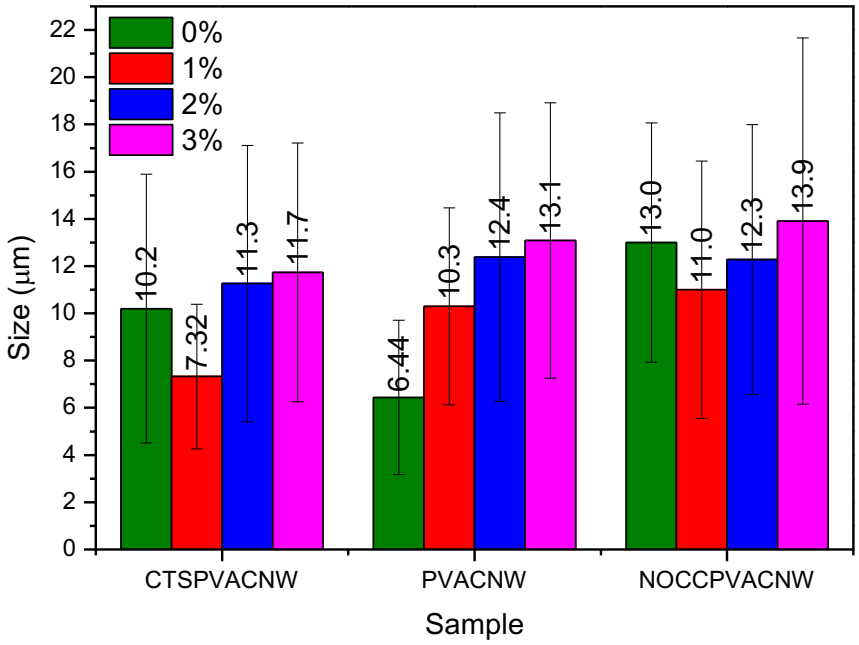

Figure 6.27: Overview of pore sizes of different matrices and different CNW filler loadings.

The pore size distribution is shown in **Figure 6.28** - **Figure 6.30** to compare the effects of the respective fillers on the matrix.

Figure 6.28 shows the pore size distribution within the primary PVA matrix with the addition of the ChNW and CNW filler to produce binary hydrogel blends. The addition of the ChNW nanofiller resulted in a narrower distribution compared to the CNW nanofiller. No concrete trends were observed with the addition of the ChNW filler whilst pore size distribution seemed to increase with the addition of increasing loadings of the CNW filler.

Figure 6.29 shows the pore size distribution within the binary CTSPVA matrix and the ternary hydrogel blends with the addition of the ChNW and the CNW filler. Again, with the addition of the ChNW filler, no concrete trends were observed. This was observed with the CNW nanofiller as well.

Figure 6.30 shows the pore size distribution of the binary NOCCPVA matrix and the ternary hydrogel blends which are produced by the addition of ChNW and CNW. No trends are observed with the addition of increasing loadings of ChNW whilst increasing loadings of CNW nanofiller seems to increase pore size distribution.

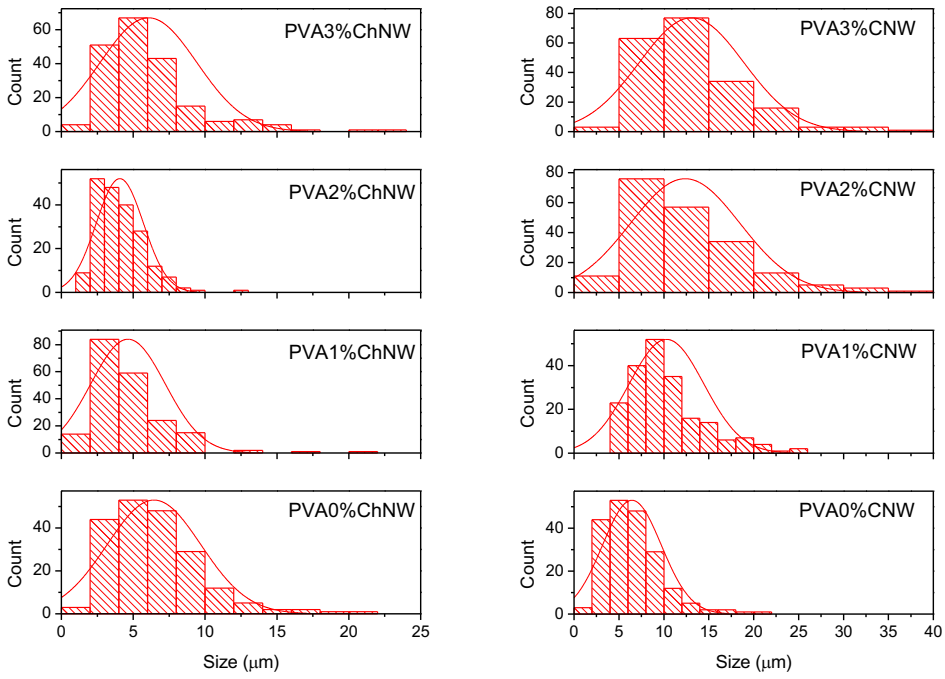

Figure 6.28: Pore size distribution of the PVA matrix with different loadings of ChNW and CNW loadings respectively.

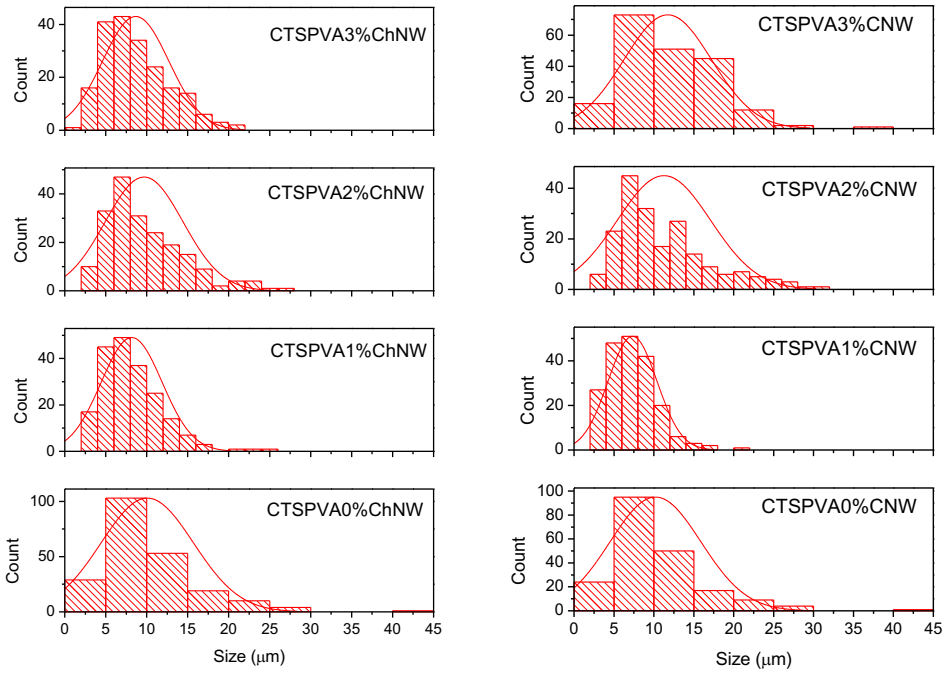

Figure 6.29: Pore size distribution of the CTSPVA matrix with different loadings of ChNW and CNW loadings respectively.

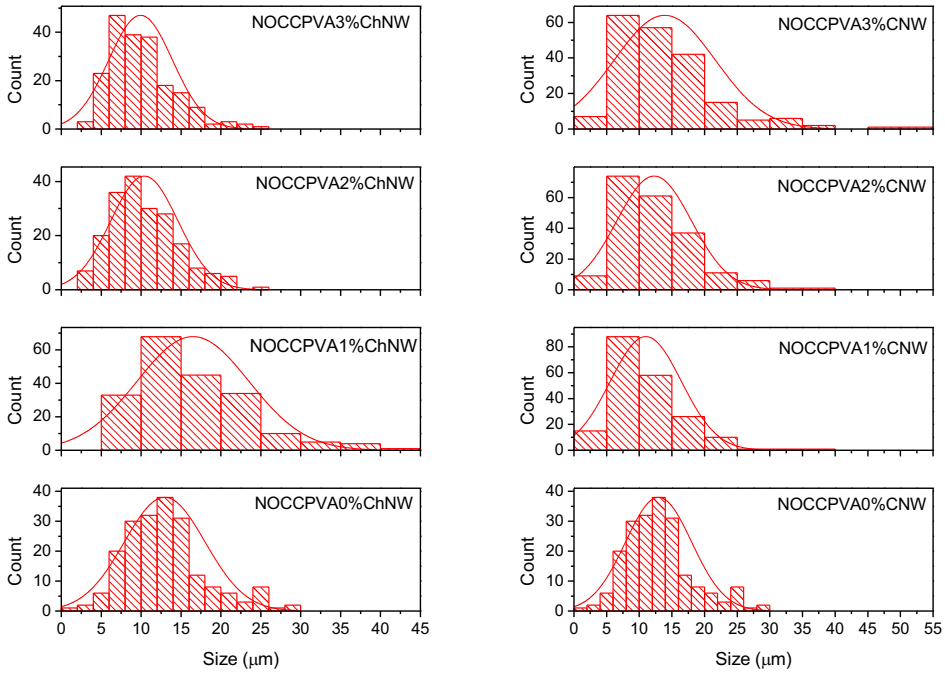

Figure 6.30: Pore size distribution of the NOCCPVA matrix with different loadings of ChNW and CNW loadings respectively.

6.2.6 Thermal analysis

6.2.6.1 Thermogravimetric analysis

TGA was performed to evaluate the stability of the produced materials. This was primarily done to determine the experimental parameters to aid in DSC, performed in Section 6.2.6.2.

This technique may improve the understanding of the effects on the degradation profiles of the respective blends with regards to the different components within the respective matrices and the effect of a different matrix whilst keeping the respective filler loading constant. **Figure 6.31** shows the decomposition of the respective fillers whilst decomposition profiles of the various blends are shown in **Figure 6.32 - Figure 6.35**.

Before evaluating the effect of the fillers on the respective matrices, the decomposition profiles of the neat fillers were obtained. The temperature profiles were recorded from 50 – 600 ºC. In **Figure 6.31** it can be seen that at the start of the profile, some of the physically weak and chemically strongly bound water that could have been absorbed after lyophilization already evaporated[40].

Table 6.1: Summary of the decomposition steps and onset of degradation of the ChNW and CNW fillers used in this study

Sample	Onset of degradation (℃)	Degradation steps (℃)	
ChNW	307.5	341.4	392.3
CNW	240.3	143.1	361.1

According to **Table 6.1** and **Figure 6.31,** it is clear that the onset of degradation for the CNW occurs at a lower temperature compared to the ChNW (240.3 ºC versus 307.5 ºC). The degradation profile of ChNW also reached a plateau at a higher temperature, compared to CNW which is indicative of the greater thermal stability of ChNW. This was also the findings by Herrera *et al.*[32] where the thermal properties of ChNWs and CNWs were evaluated for its use in nanocomposite films. The degradation profiles for the ChNWs and CNWs were also confirmed by other sources[41].

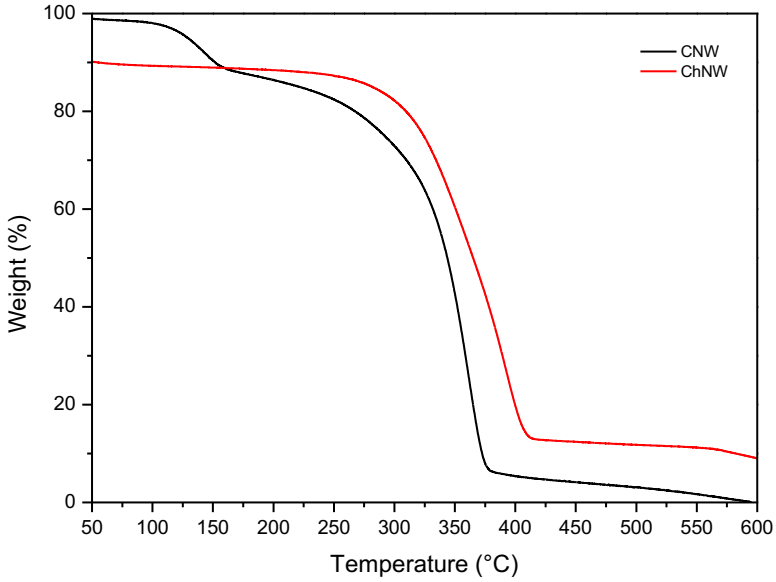

Figure 6.31: A comparison of the decomposition profiles of the ChNW and CNW fillers.

Chitin primarily degrades within the range of 300 – 460 ºC[42]. The first degradation step occurs between 43.9 and 102 ºC[43]. The second weight-loss step for chitin occurs between 250 and 400 ºC[43]. During this step decomposition/depolymerization of polymer chains occurs via deacetylation and cleavage of glycosidic links[44]. The last stage occurs above 400 ºC and entails the decomposition of the pyranose ring as well as the destruction of the residual carbon[45,46]. The residue at 600 ºC for ChNW is also consistent with the results reported in literature[41].

In cellulose, degradation begins at temperatures of about 200 – 300 ºC[47]. This onset of degradation is dependent on the composition of the cellulose fibrils which contains cellulose, hemicellulose, and lignin[47–49]. According to Yang *et al.*[47], cellulose begins to degrade around 315 ºC, hemicellulose at around 220 ºC, and lignin at around 160 ºC. Horseman *et al*.[50] stated that if cellulose fibers are highly purified, they will degrade at a higher temperature. Thus the onset of degradation as well as the degradation steps are dependent on the sample purity and composition.

Table 6.2: Summary of the decomposition steps and onset of degradation of the CTSPVA matrix with ChNW as filler at different loadings compared to the NOCCPVA and PVA matrix with 2% ChNW as filler. Temperatures in bold were identified as the main mass loss step by looking at the first derivative

Sample	The onset of degradation (℃)	Degradation steps (℃)			
CTSPVA0%ChNW	231.9	**257.9**	441.5		
CTSPVA1%ChNW	240.3	**280.8**	345.1	434.4	
CTSPVA2%ChNW	251.5	278.3	359.3	**387.9**	436.5
CTSPVA3%ChNW	258.9	278.9	345.2	**382.7**	435.7
NOCCPVA2%ChNW	235.9	**282.7**	350.6	493.2	
CTSPVA2%ChNW	251.5	278.3	359.3	**387.9**	436.5
PVA2%ChNW	316.7	**367.7**	386.5	439.2	

It had been reported that CNWs and ChNWs are used for reinforcement purposes in a variety of polymeric matrices including but not limited to chitosan[51]. Nanowhiskers have a high Young's modulus (*ca.* 140 GPa)[52,53] and this leads to enhanced thermal stability, improved mechanical performance, and a higher overall Young's modulus of the nanocomposite[51]. When looking at **Table 6.2** it is clear that the onset of degradation temperature increased with an increase in ChNW loading in the CTSPVA matrix as expected from literature[51]. Because of the presence of ChNW which had a higher degradation temperature than the matrix we expect the degradation temperature of the nanocomposite to increase as well because these ChNWs have to physically degrade with the matrix and the interaction between the matrix and the fillers will also play a role. When changing the matrix and keeping the ChNW filler loading constant it was seen that the addition of a second polymer such as CTS and NOCC decreased the onset of degradation. The addition of CTS to the PVA matrix perturbs the formation of PVA crystallites by preventing the PVA chains that interact with chitosan chains to partake in crystal formation[7,54]. This then leads to a decreased final crystallinity and an increase in the rate of degradation because the crystalline junction points serve as crosslinks in a physically crosslinked hydrogel[7]. It had also been reported that certain additives to the PVA matrix such as dextran seems to favor the crystallization process[7]. Thus the extent to which crystallization is favored is dependent on the interactions between the matrix and the polymer or compound added. In **Table 6.2** and **Figure 6.33,** it became clear that the addition of NOCC to the matrix decreased the onset of degradation temperature the most (235.9 ºC) compared to chitosan. The addition of NOCC also caused an increase in decomposition rate as seen in **Figure 6.33**. Initially, the intermolecular and intramolecular forces in NOCC maintained thermal stability

utilizing covalent forces[55] but that soon diminished. The increased rate of decomposition could be attributed to the decreased crosslinking density upon the addition of NOCC to PVA[56], attributed to the reduced interaction between polymer chains. Chitosan thus disrupts the crystallization process less than NOCC as seen in its lower rate of degradation in **Figure 6.33.** This behavior is due to more favorable intermolecular interactions between PVA and CTS in blends increasing crosslinking density[54].

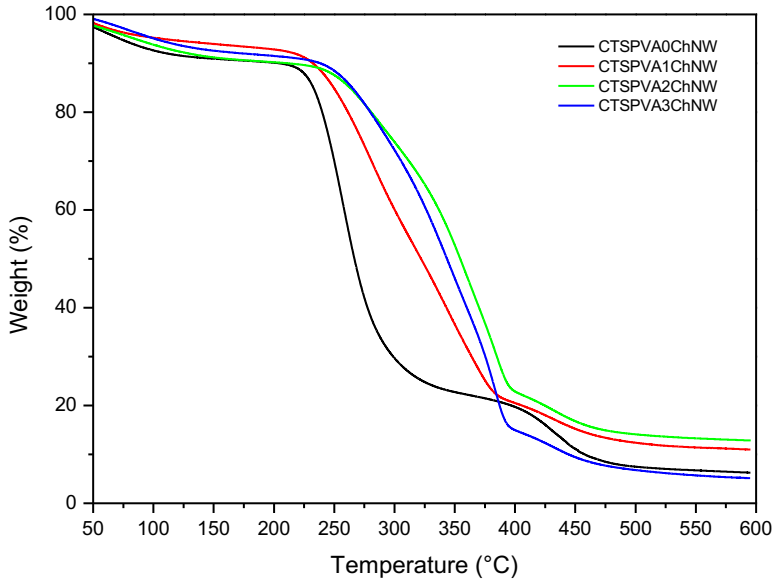

Figure 6.32: A comparison of the decomposition profiles of the CTSPVA matrix with different loadings of ChNW.

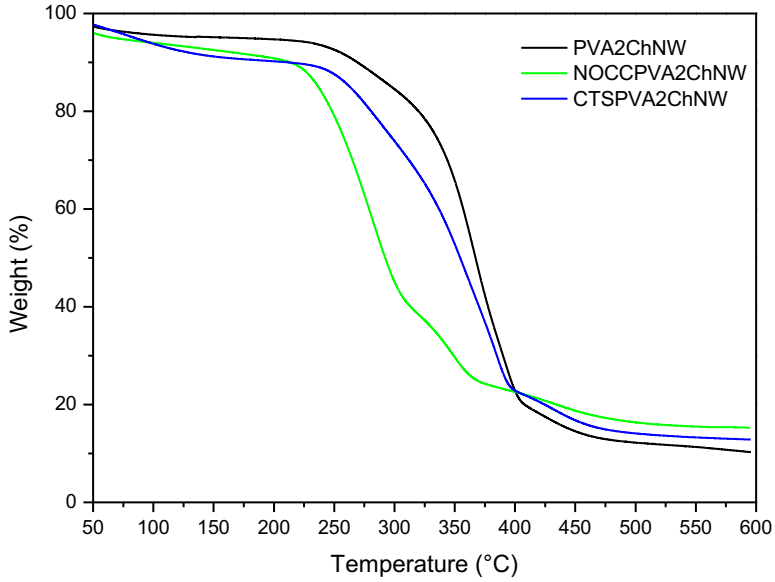

Figure 6.33: A comparison of the decomposition profiles of different matrices with ChNW filler loadings of 2%.

Table 6.3: Summary of the decomposition steps and onset of degradation of the CTSPVA matrix with CNW as filler at different loadings compared to the NOCCPVA and PVA matrix with 2% CNW as filler. Temperatures in bold were identified as the main mass loss step by looking at the first derivative

Sample	The Onset of degradation (℃)	Degradation steps (℃)		
CTSPVA0%CNW	231.9	**257.9**	441.5	
CTSPVA1%CNW	303.3	**356.9**	420.3	
CTSPVA2%CNW	270.9	**343.5**	432.1	
CTSPVA3%CNW	306.4	**356.6**	431.0	
NOCCPVA2%CNW	267.2	**333.2**	427.7	495.7
CTSPVA2%CNW	270.9	**343.5**	432.1	
PVA2%CNW	272.4	**343.6**	429.7	

Table 6.3 shows the effect of the addition of the CNW filler to the CTSPVA matrix as well as the effect of changing the matrix and keeping the CNW filler loading constant. It is observed that with an increase from 1% to 3% of the CNW nanofiller in the CTSPVA matrix, the degradation temperature as well as the onset of degradation increases as expected from literature[51]. As mentioned, CNWs and ChNWs are used as reinforcement filers in matrices such as chitosan. Due to their high Young's modulus[52,53], they also improve the thermal stability and mechanical performance with the overall enhancement of Young's modulus of the composite they are used in[51].

The 2% addition of CNW to the matrix, however, decreased the onset of degradation temperature as well as the temperature of the consequent degradation steps. This may be explained by the extent of agglomeration as agglomeration is common in polysaccharide nanowhiskers such as CNWs due to the strong intermolecular interactions between them[32]. This may lead to a reduction in crystallinity and may explain the increased rate of degradation that this specific loading underwent. Agglomeration was also observed in Section 6.2.4 and visible in CFM images.

When changing the matrix and keeping the CNW filler loading constant it was seen that the addition of a second polymer to the PVA matrix such as CTS and NOCC decreased the onset of degradation. The degradation steps for the CTSPVA matrix remained similar to the PVA matrix and the NOCCPVA matrix caused the degradation steps to occur earlier. As discussed above, the addition of a second polymer such as CTS or NOCC perturbs the formation of PVA crystallites[7,54] leading to a decreased crystallinity and thus a decrease in junction points to

serve as crosslinks[7]. When comparing the degradation profiles in **Figure 6.33** and **Figure 6.35** it is clear that the samples containing the CNW filler were more thermally stable. This could be explained by research done by Zhou *et al*.[38] where it was found that the addition of CNW to the matrix accelerated gel formation while simultaneously enhancing the formation of effective crosslinks. As crystalline regions serve as junction points or crosslinks it can be proposed that crystallinity also increased which leads to a more thermally stable hydrogel.

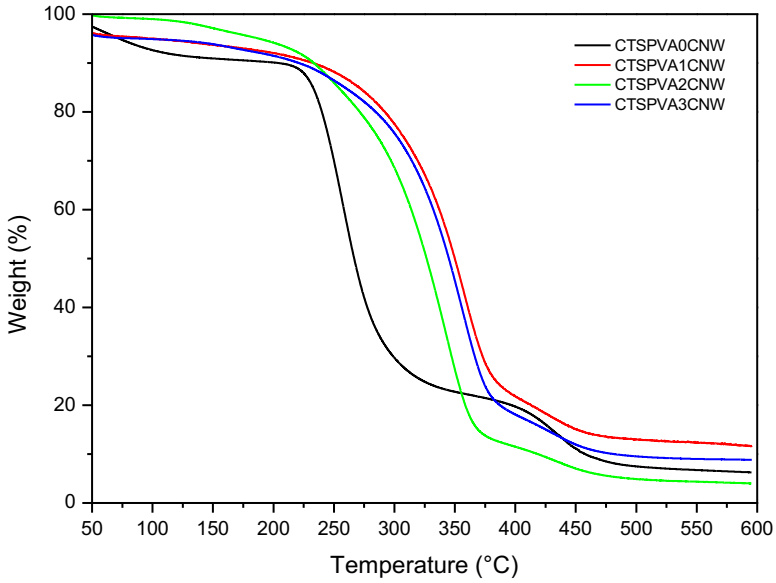

Figure 6.34: A comparison of the decomposition profiles of the CTSPVA matrix with different loadings of CNW.

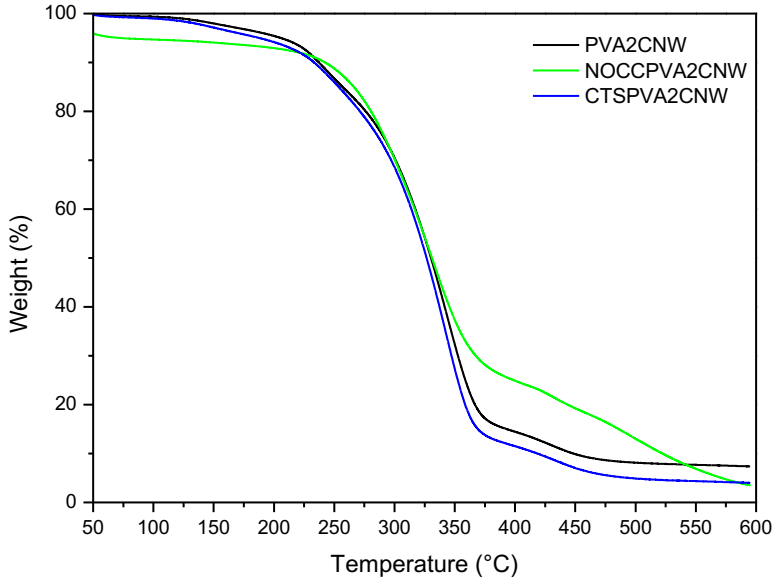

Figure 6.35: A comparison of the decomposition profiles of different matrices with CNW filler loadings of 2%.

6.2.6.2 Differential scanning calorimetry (DSC)

The thermograms of the primary, binary, and ternary hydrogel blends were obtained to investigate the thermal events that occur in these hydrogel blends upon thermal treatment. Thermograms are shown in **Figure 6.36** – **Figure 6.41** and a summary can be seen in **Table 6.4 – Table 6.6**. It is important to note that all samples evaluated by DSC were heated to 250 ºC and kept at 250 ºC, isothermally for 5 minutes to erase thermal history. This will result in comparable DSC results which will differ from TGA results as TGA was performed on samples that retained their full thermal history.

Following the evaluation of the binary hydrogel blends, from **Table 6.4** it is clear that the addition of the ChNW filler into the PVA matrix increased the melting enthalpy approximately two-fold. This translates to an increase in crystallinity of approximately 100%. It is expected that the addition of the ChNWs will increase crystallinity and melting enthalpy and thus lead to an increase in the thermal stability[51]. A slight increase in melting temperature was also detected with the addition of ChNWs as seen in **Table 6.4**. This could be due to the strong interactions between the ChNWs and the PVA chains where hydrogen bonds form between hydroxyl and acetyl groups present in ChNWs and hydroxyl groups present in PVA which will lead to a higher number of crystalline domains[19]. Taking this into account, more energy will be needed for PVA chains to become free and initiate melting[19]. This was however only true for a ChNW filler loading of 1% into the PVA matrix. As the filler content increased, the melting enthalpy decreased which is a clear indication that the filler content should not surpass a certain percentage as the effects on the crystallinity of the blend will become detrimental. In literature, this effect was ascribed to the aggregation of the polysaccharide nanowhiskers[23].

As with the melting enthalpy, an initial increase in crystallization enthalpy is observed followed by a subsequent decrease in enthalpy. The crystallization enthalpy soon became less than the enthalpy of the primary PVA hydrogel. Upon the cooling cycle in which crystallization is observed, crystallization initially occurred at a higher temperature, followed by lower temperatures as the ChNW loading was increased. This effect soon diminished as a result of the tendency of the ChNWs to cause agglomeration[23]. As mentioned, many agglomerated ChNWs will be micro fillers[35]. From this, it is clear that micro fillers have an adverse effect on nucleation which caused the crystallization enthalpy as well as crystallization temperature to decrease. The effects discussed can also be visually observed in **Figure 6.36**.

Table 6.4 and **Figure 6.37** shows the effect of the addition of the CNW filler into the PVA matrix. The effect that the CNW filler had on the PVA matrix is similar to the effect of the ChNW filler. An initial increase in melting enthalpy is seen with the addition of 1% CNW filler followed

by a decrease in melting enthalpy upon subsequent addition of increasing loadings of the CNW filler. This was also observed by Shalom *et al*.[57] where higher loadings of CNWs interfered with the crystallinity of the matrix. Initially, the addition of CNWs increased the nucleation of spherulites, but subsequently increasing loadings of CNWs had a detrimental effect on the final matrix crystallinity. The melting temperature also follows the same trend as with the ChNW where an initial increase is observed followed by a decrease in melting temperature with increasing CNW filler content. Initially, PVA forms strong hydrogen bonds with the hydrophilic CNWs[57] and acts as a good nucleating agent leading to an increase in crystallinity. More thermal energy will then be necessary to facilitate the movement of chains thus melting will occur at a higher temperature.

The crystallization enthalpy shows an initial increase up to the addition of 2% CNW filler content where after a decrease in enthalpy is observed whilst the crystallization temperature of the binary hydrogel blend of PVA and CNW shows an initial increase in temperature followed by a decrease in temperature. This can be visually observed in **Figure 6.17**. Initially, CNW's acted as a nucleating agent, resulting in higher crystallinity and thus, crystallization enthalpy. This effect then diminished as seen in literature[57] and is due to the agglomeration of CNW[23]. Agglomeration of nanofillers resulted in micro fillers which negatively affected nucleation of PVA spherulites.

Table 6.4: Peak melting temperature enthalpy with peak crystallization temperature enthalpy of PVA matrix with different loadings of ChNW and CNW nano fillers

Sample	Peak melting temperature (°C)	Melting enthalpy (J/g)	Peak crystallization temperature (°C)	Crystallization enthalpy (J/g)
PVA0%	217.2	14.5	190.7	23.3
PVA1%ChNW	226.7	28.9	204.6	32.6
PVA2%ChNW	226.7	20.8	204.3	20.4
PVA3%ChNW	224.6	16.0	202.6	16.7
PVA1%CNW	223.1	22.9	199.7	27.2
PVA2%CNW	220.6	22.0	197.8	31.0
PVA3%CNW	214.5	17.7	187.2	20.7

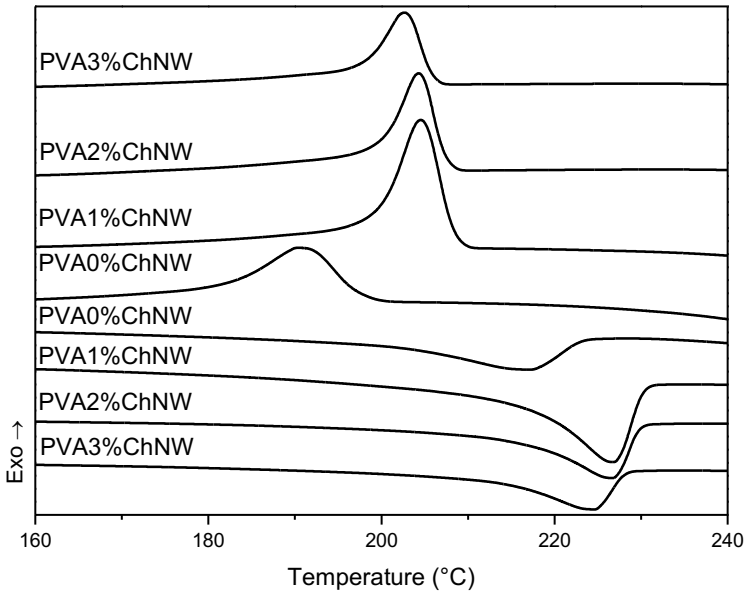

Figure 6.36: DSC thermograms of the second heating cycle and crystallization cycle of primary hydrogels from PVA and binary blends of PVA and ChNW.

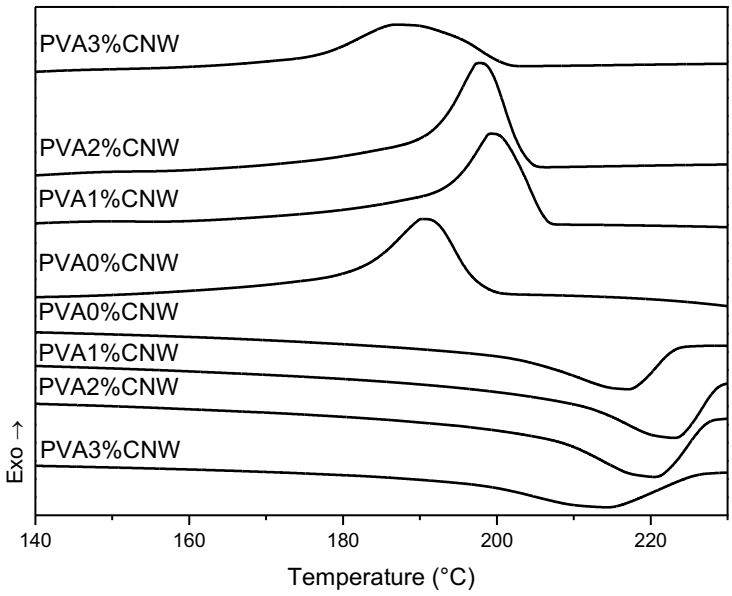

Figure 6.37: DSC thermograms of the second heating cycle and crystallization cycle of primary hydrogels from PVA and binary blends of PVA and CNW.

Table 6.5 shows the effect of changing the matrix by the addition of CTS to produce ternary hydrogel blends. By first comparing the matrix in the absence of fillers to the neat PVA matrix in **Table 6.4** it is observed that the addition of CTS greatly decreases the temperature at which melting occurs as well as the melting enthalpy. A similar observation can be made concerning the crystallization temperature and enthalpy. This effect of the addition of CTS to the matrix is expected as CTS perturbs the formation of PVA crystallites[7,54]. This prevents the PVA chains that interact to partake in crystallization which results in more amorphous areas within the sample. **Figure 6.38** and **Figure 6.39** clearly show the effect that the addition of CTS had on the thermograms of CTSPVA0%, in which the melting and crystallization behavior seems to be suppressed. As crystalline regions serve as junction points, an increase in amorphous areas will lead to a decrease in crosslinking density which will in turn cause melting as well as degradation of the sample to occur at a lower temperature. According to literature[23], CTS and the ChNW filler used in the production of these hydrogel blends are structurally compatible and exhibit the formation of strong intermolecular forces such as hydrogen bonding between hydroxyl and acetyl groups, present in both ChNW and CTS. The interfacial adhesion between ChNWs and CTS has been reported as being excellent[23]. Due to the presence of CTS in these ternary blends, increased interaction between the filler and the matrix exists which increases the dispersion degree of these nano fillers[29,30]. An increased degree of nanofiller dispersion will in this case lead to better nucleation and will result in an increased crystallinity. In this case, it seems as if ChNWs acted as a compatibilizer between PVA and CTS. This is however

not the case in the binary blends of PVA and ChNW because, in the absence of CTS, particle/particle interaction dominates due to their strong intermolecular interactions. In the case of the CTSPVA matrix which contains the CNW filler, it seems that the interaction mentioned earlier between the filler and CTS is less pronounced as crystallization seems to only be enhanced up to the addition of 2% of the CNW filler. With an increase in CNW content the melting enthalpy and crystallization enthalpy, initially increase and then decrease after a further increase of filler content above 2% due to the negative effect that agglomeration has on the nucleation of PVA spherulites[23].

Table 6.5 and **Figure 6.38** shows that with an increase in filler content an increase in melting temperature is observed. This is different from the observation made earlier concerning **Table 6.4** where only an initial increase in melting temperature was observed. Melting enthalpy also increased with increasing loadings of ChNW content. The same effect was observed for both the melting temperature and melting enthalpy when compared to crystallization temperature and crystallization enthalpy, respectively. This phenomenon can be explained by the increased interaction between the ChNWs and CTS as explained earlier.

Table 6.5: Peak melting temperature and enthalpy with peak crystallization temperature and enthalpy of CTSPVA matrix with different loadings of ChNW and CNW nanofillers

Sample	Peak melting temperature (°C)	Melting enthalpy (J/g)	Peak crystallization temperature (°C)	Crystallization enthalpy (J/g)
CTSPVA0%	190.5	7.20	164.1	3.50
CTSPVA1%ChNW	213.0	9.70	186.5	11.7
CTSPVA2%ChNW	216.8	12.2	191.9	15.5
CTSPVA3%ChNW	217.0	17.8	192.1	19.7
CTSPVA1%CNW	221.9	16.2	199.5	23.0
CTSPVA2%CNW	218.1	19.3	192.0	19.3
CTSPVA3%CNW	217.2	18.5	190.7	17.6

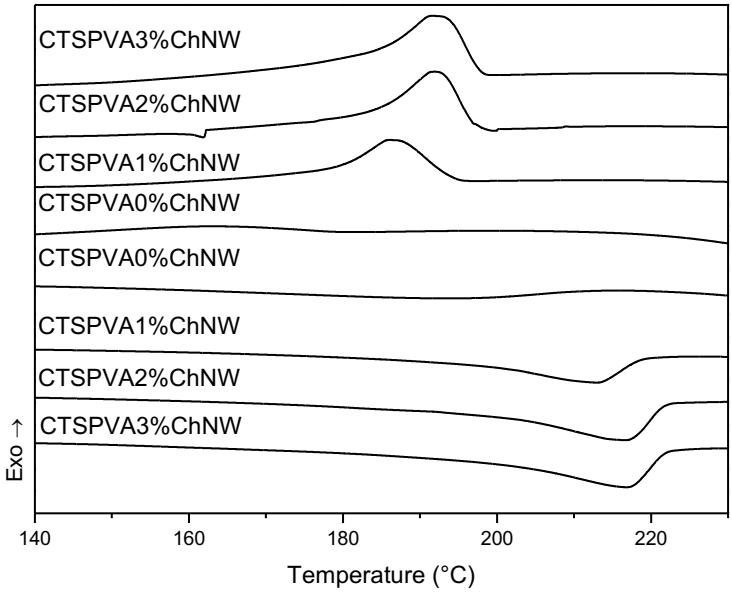

Figure 6.38: DSC thermograms of the second heating cycle and crystallization cycle of binary hydrogels from CTS and PVA and ternary blends of CTS, PVA, and ChNW.

According to **Table 6.5** and **Figure 6.39,** an initial increase in CNW content causes the melting enthalpy as well as the crystallization enthalpy to increase but decrease with increasing loadings of CNW filler. Here it is the suppression of melting and crystallization behavior that is also observed upon the addition of CTS. As discussed earlier it seems that CNWs acted as compatibilizers between PVA and CTS just like ChNWs did. Melting temperature is also increased due to the formation of strong hydrogen bonds between the CNW filler and the matrix[57]. A similar observation can be made for the melting and crystallization temperatures. Initially, good dispersion of the CNW filler is achieved. The addition CNWs accelerate nucleation as well as gel formation[38]. This effect soon diminishes as CNWs agglomerate to form secondary particles which negatively affect nucleation and PVA spherulite formation.

Table 6.6: Peak melting temperature and melting enthalpy with peak crystallization temperature and crystallization enthalpy of NOCCPVA matrix with different loadings of ChNW and CNW nano fillers

Sample	Peak melting temperature (°C)	Melting enthalpy (J/g)	Peak crystallization temperature (°C)	Crystallization enthalpy (J/g)
NOCCPVA0%	222.8	21.5	197.7	30.3
NOCCPVA1%ChNW	218.7	11.7	191.2	19.6
NOCCPVA2%ChNW	222.3	16.2	198.5	21.0
NOCCPVA3%ChNW	221.9	13.1	197.4	14.4
NOCCPVA1%CNW	220.9	27.9	195.0	31.8
NOCCPVA2%CNW	219.7	16.7	193.9	28.9
NOCCPVA3%CNW	213.4	16.1	187.4	15.0

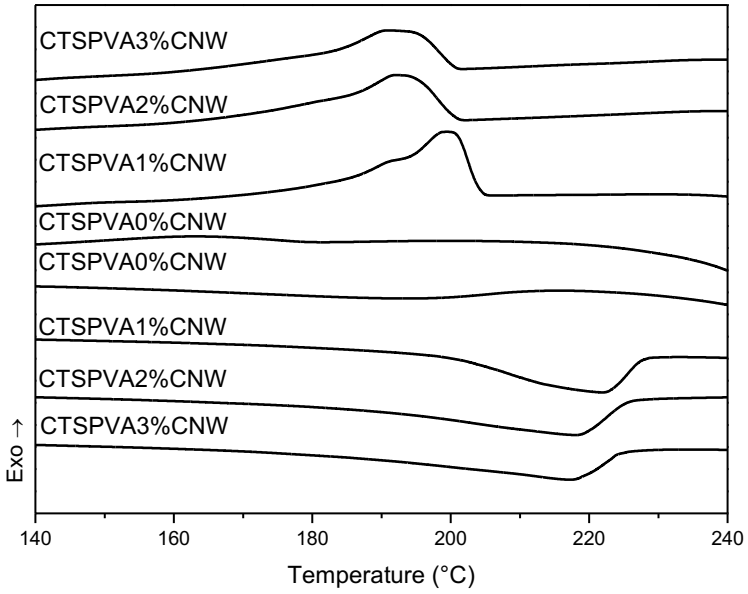

Figure 6.39: DSC thermograms of the second heating cycle and crystallization cycle of binary hydrogels from CTS and PVA and ternary blends of CTS, PVA, and CNW.

The effect of changing the matrix to a blend of NOCC and PVA is shown in **Table 6.6**. When comparing this to the PVA matrix in the absence of fillers as per **Table 6.4** it became clear that the addition of NOCC increased the peak melting temperature as well as the melting enthalpy. This means that NOCC acted as a nucleating agent which enhanced spherulite formation which leads to a higher crystallinity. Crystallization occurs upon cooling and it is

observed that the crystallization temperature also increased with the crystallization enthalpy. As crystallization occurred at a higher temperature, spherulite formation was facilitated by the addition of NOCC. So an overall increase in crystallinity in the absence of nanofillers was observed when comparing the NOCCPVA0% matrix to that of PVA0%. It can thus be deduced that PVA and NOCC form a miscible blend upon the combination of these two polymers.

Table 6.6 and **Figure 6.40** shows the effect of the addition ChNW to the binary blend of NOCC and PVA to produce ternary blends. It is observed that there is no significant change in the peak melting temperature, but the melting enthalpy does seem to decrease with increasing ChNW content. This decrease in melting enthalpy could also be attributed to agglomeration as discussed earlier[23].

Table 6.6 and **Figure 6.41** shows the effect of the addition of the CNW nanofiller on the binary matrix of NOCC and PVA. The addition of the CNW nanofiller causes a decrease in the peak melting temperature whilst an initial increase in the melting enthalpy is observed with the addition of 1% CNW, a decrease is observed thereafter. At a loading of 1% the CNWs act as a nucleating agent which improves nucleation and enhances PVA spherulite formation. This will lead to a higher crystallinity and thus a higher melting enthalpy is observed. This effect, however, diminishes with a further increase in the CNW loading due to the formation of secondary particles resulting in micro fillers. With regards to peak crystallization temperature, a slight decrease with an increase in CNW filler loading is observed but this is not significant. The same trend is observed with the crystallization enthalpy where a slight increase is observed after a 1% addition of CNW filler, followed by a decrease in crystallization enthalpy with subsequently higher loadings of the CNW filler. Initially, crystallization is favored and it can occur at a higher temperature due to the enhancement of PVA spherulite formation, but as the CNW loading is increased crystallization is negatively affected by agglomeration as mentioned in literature[23].

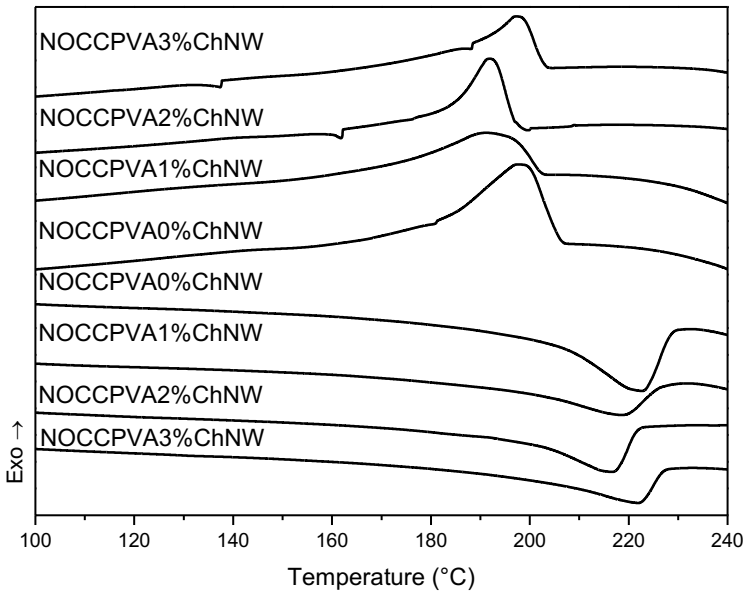

Figure 6.40: DSC thermograms of the second heating cycle and crystallization cycle of binary hydrogels from NOCC and PVA and ternary blends of NOCC, PVA, and ChNW.

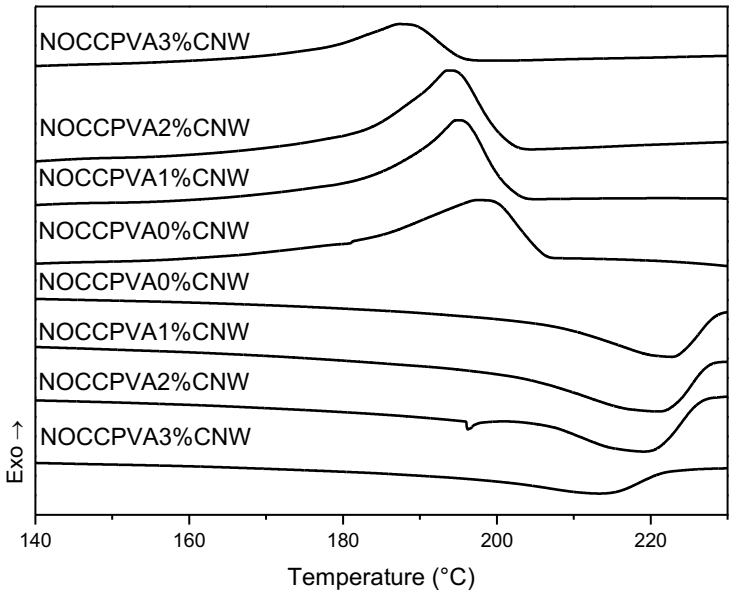

Figure 6.41: DSC thermograms of the second heating cycle and crystallization cycle of binary hydrogels from NOCC and PVA and ternary blends of NOCC, PVA, and CNW.

6.3 Conclusion

From the results of the amplitude sweep, it became clear that the addition of the respective nanofillers had a pronounced effect on the LVE limit of the respective samples. In the

NOCCPVA matrix, an increase in the LVE limit was observed upon the addition of the ChNW and the CNW filler, respectively. The addition of the CNW filler decreased the LVE limit in the CTSPVA whilst a 1% addition of the ChNW filler to the CTSPVA matrix increased the LVE limit. When evaluating the PVA matrix it is seen that the addition of both ChNW and CNW resulted in a decrease in the LVE limit. Successful hydrogel formation was observed after looking at G' and G" of the respective matrices. It was also noted that the NOCCPVA matrix had the lowest G' whilst the CTSPVA matrix had the highest G'. This corresponds to the highest LVE limit of the pure CTSPVA matrix and the lowest LVE limit of the NOCCPVA matrix.

From the swelling studies, it became clear that the addition of CNWs to all the matrices resulted in the greatest percentage weight gain, compared to ChNW. The lower percentage weight gain for matrices containing ChNWs was attributed to the hydrophobicity imparted by the acetyl group contained in the ChNW structure. When comparing the effect of the addition of different polymers to the pure PVA matrix it became clear that the addition of NOCC resulted in the greatest percentage weight gain when compared to chitosan. This was attributed to the fact that chitosan contains acetyl groups that contribute to hydrophobicity whilst NOCC contains deprotonated carboxyl groups at a pH of 7 which imparts strong interactions with water.

The antimicrobial evaluation showed that the addition of the respective loadings of the CNW filler facilitated antimicrobial growth in all the matrices whilst the addition of the ChNW filler to the respective matrices inhibited antimicrobial growth.

From the CFM images, it is evident that agglomeration occurred in all of the matrices evaluated. Agglomeration occurred to the greatest extent in the PVA matrix followed by the CTSPVA matrix and the NOCCPVA matrix. The CNW filler seemed to cause less agglomeration than the ChNW filler in the respective matrices so it can be deduced that the CNW filler was more compatible with the respective matrices and had better interaction with the matrices than the ChNW filler.

When looking at the galleries produced by the progressive deeper scans of the sample it was evident that the fluorescent signals were absent from the surface which means that both the ChNWs and the CNWs were embedded deeper into the matrix. Scans could unfortunately only be taken about 51.9 µm deep due to out-of-focus images produced at deeper levels. Thus it can be concluded that even though some agglomeration occurred, both the ChNW and the CNW fillers were distributed throughout the matrices.

According to literature[33,36], contradicting evidence has been reported with regards to the effect that the addition of nanofillers had on the crystallinity and pore size observed in nanocomposites. The shape and size, as well as the interaction between the nanofiller and the matrix, have a pronounced effect on the crystallinity, and in turn, pore size, according to Holloway *et al.*[9]. As the degree of crystallization increases, so does the pore size. The opposite of this statement is also true. Agglomeration of nanofillers due to the strong interactions between these individual nanofiller particles will also play a role as the size of these aggregates will vary. Larger aggregates will perturb the formation of crystallites more and lead to a greater decrease in final crystallinity and thus a decrease in pore size.

It should also be noted that because the porogen was removed by lyophilization after the freeze-thaw procedure it will cause shrinkage of the polymer network and the pores will collapse to some extent[39]. This will then lead to inhomogeneous performance that not even re-swelling will remedy[31]. Every precaution has been taken during lyophilization to ensure identical treatment of all samples.

Evaluation of the polysaccharide nanowhiskers used in this study proved that ChNWs are more thermally stable than CNWs. Upon evaluation of these ternary blends of PVA, CTS, and/or NOCC reinforced with ChNW or CNW it became evident that the addition of polysaccharide nanowhiskers increased the thermal stability of the hydrogel blends. According to literature, this enhancement of the thermal and mechanical properties of the resulting composites is due to the high Young's modulus of the polysaccharide nanowhiskers[51]. As these polysaccharide nanowhiskers are prone to agglomeration due to their strong interaction and hydrogen bonding it could influence the thermal stability as agglomeration will also influence the final crystallinity and the rate of degradation of these blends. This is observed where the CTSPVA2%CNW sample did not follow the same trend in thermal stability in **Table 6.3**

Further, it was observed that by changing the matrix by the addition of CTS or NOCC to PVA, the thermal stability of these blends was reduced and this is because the addition of a second polymer may perturb the formation of PVA crystallites[7,54]. Crystalline regions serve as junction points in physical hydrogels and thus if there is a reduction in crystalline regions, there will also be a reduction in junction points which will lead to decreased thermal stability.

When comparing the same matrices with different nanofillers as shown in **Figure 6.33** and **Figure 6.35**, it can be seen that the matrices containing the CNW nanofiller are more thermally stable than the matrices containing the ChNW nanofiller. Thus CNWs have a stabilizing effect on the thermal stability as opposed to the ChNWs which are more destabilizing.

DSC results show that the addition of a second polymer to the pure PVA matrix such as CTS caused a decrease in both the melting and crystallization enthalpy since CTS perturbs the formation of PVA spherulites[7,54]. This caused a decrease in overall matrix crystallinity compared to the primary PVA hydrogel. It is observed that the addition of NOCC to PVA leads to an increase in melting and crystallization enthalpy and it is deduced that the inclusion of NOCC in the PVA matrix enhanced nucleation and thus PVA spherulite formation. The addition of NOCC resulted in an overall increase in matrix crystallinity. Thus CTS is less compatible with PVA than NOCC but it is observed that ChNWs and CNWs acted as compatibilizers in the blend of PVA and CTS and improved the blend compatibility.

The addition of ChNWs and CNWs to the respective matrices all resulted in an initial increase in crystallinity at low nanofiller loadings. This is because the nanofillers served as nucleation sites PVA chains. This then leads to an increase in crystallinity and thus an increase in melting enthalpy. This effect, however, soon diminishes at higher polysaccharide nanowhiskers loadings due to the tendency of polysaccharide nanowhiskers to agglomerate and the difficulty encountered when trying to redisperse them in aqueous media[32]. Secondary particle formation results as a consequence of agglomeration and this have a negative effect on nucleation which caused a decrease in melting enthalpy as well as crystallization temperature and enthalpy.

6.4 References

1 F. Lotfipour, M. Alami-Milani, S. Salatin, A. Hadavi and M. Jelvehgari, *Res. Pharm. Sci.*, 2019, **14**, 175–189.

2 F. Reguieg, L. Ricci, N. Bouyacoub, M. Belbachir and M. Bertoldo, *Polym. Bull.*, 2020, **77**, 929–948.

3 J. G. Fernandez and D. E. Ingber, *Adv. Funct. Mater.*, 2013, **23**, 4454–4466.

4 T. R. Hoare and D. S. Kohane, *Polymer (Guildf).*, 2008, **49**, 1993–2007.

5 N. Bhattarai, J. Gunn and M. Zhang, *Adv. Drug Deliv. Rev.*, 2010, **62**, 83–99.

6 D. J. Leaper, *Int. Wound J.*, 2006, **3**, 282–294.

7 H. Zhang, F. Zhang and J. Wu, *React. Funct. Polym.*, 2013, **73**, 923–928.

8 J. Tavakoli, J. Gascooke, N. Xie, B. Z. Tang and Y. Tang, *ACS Appl. Polym. Mater.*, 2019, **1**, 1390–1398.

9 J. L. Holloway, A. M. Lowman and G. R. Palmese, *Soft Matter*, 2013, **9**, 826–833.

10 A. Rafique, K. Mahmood Zia, M. Zuber, S. Tabasum and S. Rehman, *Int. J. Biol. Macromol.*, 2016, **87**, 141–154.

11 H. Hamedi, S. Moradi, S. M. Hudson and A. E. Tonelli, *Carbohydr. Polym.*, 2018, **199**, 445–460.

12 Y. Qin and P. Li, *Int. J. Mol. Sci.*, 2020, **21**, 499–518.

13 R. De Souza, P. Zahedi, C. J. Allen and M. Piquette-Miller, *Biomaterials*, 2009, **30**, 3818–3824.

14 H. S. Kusuma, A. F. Al-sa'bani and H. Darmokoesoemo, *Procedia Food Sci.*, 2015, **3**, 35–51.

15 H. Homayoni, S. A. H. Ravandi and M. Valizadeh, *Carbohydr. Polym.*, 2009, **77**, 656–661.

16 V. K. Mourya, N. N. Inamdar and A. Tiwari, *Adv. Mater. Lett.*, 2010, **1**, 11–33.

17 I. Agirre-Olabide, J. Berasategui, M. J. Elejabarrieta and M. M. Bou-Ali, *J. Intell. Mater. Syst. Struct.*, 2014, **25**, 2074–2081.

18 A. P. Meera, S. Said, Y. Grohens and S. Thomas, *J. Phys. Chem. C*, 2009, **113**, 17997–18002.

19 H. Lisboa, *Polímeros*, 2018, **28**, 69–75.

20 E. L. Lindh, M. Bergenstråhle-Wohlert, C. Terenzi, L. Salmén and I. Furó, *Carbohydr. Res.*, 2016, **434**, 136–142.

21 M. Rinaudo, *Prog. Polym. Sci.*, 2006, **31**, 603–632.

22 J. Brugnerotto, J. Lizardi, F. . Goycoolea, W. Argüelles-Monal, J. Desbrières and M. Rinaudo, *Polymer (Guildf).*, 2001, **42**, 3569–3580.

23 B. Ma, A. Qin, X. Li, X. Zhao and C. He, *Mater. Lett.*, 2014, **120**, 82–85.

24 L. C. Wang, X. G. Chen, D. Y. Zhong and Q. C. Xu, *J. Mater. Sci. Mater. Med.*, 2007, **18**, 1125–1133.

25 S. Kalliola, E. Repo, V. Srivastava, F. Zhao, J. P. Heiskanen, J. A. Sirviö, H. Liimatainen and M. Sillanpää, *Langmuir*, 2018, **34**, 2800–2806.

26 S. N. Rampersad, *Sensors*, 2012, **12**, 12347–12360.

27 O. Tyc, L. Tomás-Menor, P. Garbeva, E. Barrajón-Catalán and V. Micol, *PLoS One*, 2016, **11**, e0169090.

28 P. Rajasekaran and S. Santra, *Front. Vet. Sci.*, 2015, **2**, e0169090.

29 J. Hári and B. Pukánszky, in *Applied Plastics Engineering Handbook*, Elsevier, 2011, pp. 109–142.

30 A. Tessema, D. Zhao, J. Moll, S. Xu, R. Yang, C. Li, S. K. Kumar and A. Kidane, *Polym. Test.*, 2017, **57**, 101–106.

31 Y. Zhang, L. Ye, M. Cui, B. Yang, J. Li, H. Sun and F. Yao, *RSC Adv.*, 2015, **5**, 78180–78191.

32 N. Herrera, A. M. Salaberria, A. P. Mathew and K. Oksman, *Compos. Part A Appl. Sci. Manuf.*, 2016, **83**, 89–97.

33 A. Jabbarzadeh and B. Halfina, *Nanoscale Adv.*, 2019, **1**, 4704–4721.

34 K. B. Nilagiri Balasubramanian and T. Ramesh, *Polym. Adv. Technol.*, 2018, **29**, 1568–1585.

35 J. Jeevanandam, A. Barhoum, Y. S. Chan, A. Dufresne and M. K. Danquah, *Beilstein J. Nanotechnol.*, 2018, **9**, 1050–1074.

36 N. Bosq and D. Aht-Ong, *Macromol. Res.*, 2018, **26**, 13–21.

37 V. E. Reinsch and L. Rebenfeld, *J. Appl. Polym. Sci.*, 1994, **52**, 649–662.

38 C. Zhou, Q. Wu, Y. Yue and Q. Zhang, *J. Colloid Interface Sci.*, 2011, **353**, 116–123.

39 K. Kudo, J. Ishida, G. Syuu, Y. Sekine and T. Ikeda-Fukazawa, *J. Chem. Phys.*, 2014, **140**, 044909.

40 C. Peng and G. Chen, *Materials (Basel).*, 2018, **11**, 1883.

41 J. H. Chen, J. G. Liu, T. Q. Yuan and R. C. Sun, *J. Appl. Polym. Sci.*, 2017, **134**, 1–8.

42 D. Stawski, S. Rabiej, L. Herczyńska and Z. Draczyński, *J. Therm. Anal. Calorim.*, 2008, **93**, 489–494.

43 H. Moussout, H. Ahlafi, M. Aazza and M. Bourakhouadar, *Polym. Degrad. Stab.*, 2016, **130**, 1–9.

44 M. Ziegler-Borowska, D. Chełminiak and H. Kaczmarek, *J. Therm. Anal. Calorim.*, 2015, **119**, 499–506.

45 I. Corazzari, R. Nisticò, F. Turci, M. G. Faga, F. Franzoso, S. Tabasso and G. Magnacca, *Polym. Degrad. Stab.*, 2015, **112**, 1–9.

46 J. B. Marroquin, K. Y. Rhee and S. J. Park, *Carbohydr. Polym.*, 2013, **92**, 1783–1791.

47 H. Yang, R. Yan, H. Chen, D. H. Lee and C. Zheng, *Fuel*, 2007, **86**, 1781–1788.

48 Majid Ali, *J. Civ. Eng. Constr. Technol.*, 2012, **3**, 80–89.

49 S. Srisuwan, N. Prasoetsopha, N. Suppakarn and P. Chumsamrong, *Energy Procedia*, 2014, **56**, 19–25.

50 T. Horseman, M. Tajvidi, C. I. K. Diop and D. J. Gardner, *Cellulose*, 2017, **24**, 2455–2468.

51 X. Shen, J. L. Shamshina, P. Berton, G. Gurau and R. D. Rogers, *Green Chem.*, 2016, **18**, 53–75.

52 T. Köhnke, A. Lin, T. Elder, H. Theliander and A. J. Ragauskas, *Green Chem.*, 2012, **14**, 1864.

53 A. Šturcová, G. R. Davies and S. J. Eichhorn, *Biomacromolecules*, 2005, **6**, 1055–1061.

54 T. Koyano, N. Koshizaki, H. Umehara, M. Nagura and N. Minoura, *Polymer (Guildf).*, 2000, **41**, 4461–4465.

55 A. Baiyrkhanova, A. Ismailova, T. Botabekova, E. Enin and Y. Semenova, *Int. J. Drug Deliv. Technol.*, 2016, **6**, 47–51.

56 Q. Liu, Q. Zuo, R. Guo, A. Hong, C. Li, Y. Zhang, L. He and W. Xue, *J. Bioact. Compat. Polym.*, 2015, **30**, 397–411.

57 T. Ben Shalom, Y. Nevo, D. Leibler, Z. Shtein, C. Azerraf, S. Lapidot and O. Shoseyov, *Macromol. Biosci.*, 2019, **19**, 1800347.

Chapter 7: Recommendations for future work

Swelling studies were only performed with distilled deionized water – different solvents (apolar and polar) should be tested in the future to investigate the swelling behavior of the hydrogels under those conditions. Other swelling media that could be used include aqueous solutions of antibiotic or antimicrobial agents to evaluate the performance of the hydrogel blend as a drug delivery system followed by antimicrobial tests.

The difference in weight gain for different loadings of nanofiller was not as pronounced as the difference in weight gain between the two nanofillers investigated. If different blends of these two fillers could be used in the production of quaternary hydrogels the effect on pore size would be quite interesting and tunable pore sizes for drug delivery purposes might be achieved.

It was also clear that after performing antimicrobial studies the CNW nanofiller facilitated microbial growth and that the ChNW filler inhibited microbial growth. It would be interesting to see what the antimicrobial effects of a hydrogel containing both the CNW and the ChNW nanofiller will be. Antimicrobial studies could also be performed on a hydrogel blend swollen with a suitable antimicrobial agent.